ACOUSTOOPTIC DIFFRACTION AND DEFLECTION IN TELLURIUM FOR THE CARBON DIOXIDE LASER

BY

© DOMINIQUE JACQUES SOUILHAC

A Thesis submitted to
the Faculty of Graduate Studies and Research
in partial fulfillment of the
requirements for the degree of
Doctor of Philosophy
(in Electrical Engineering)

Department of Electrical Engineering
McGill University
Montreal, Quebec, Canada

January, 1987.

ACOUSTOOPTIC DIFFRACTION AND DEFLECTION IN TELLURIUM FOR THE CARBON DIOXIDE LASER

ABSTRACT

This thesis follows the work done in the last decade to analyse the acoustooptic [AO] effect in materials and more recently, the observation [1] that tellurium exhibits an exceptionally large acoustooptic figure of merit at the 10.6μm CO_2 laser wavelength, in a particular acoustic wave and optical beam configuration. A new comprehensive analytic analysis of single and multifrequency AO diffraction involving uniform plane waves is presented as well as the results obtained for the first time of an experimental and quantitative analysis of AO diffraction and deflection for birefringent and isotropic configurations that scan the entire space of the crystal.

First the diffraction efficiency is derived for first-order AO interactions for a general acoustic and optic beam propagation condition; a complete expression for the figure of merit is consequently derived, the relationship between incident and diffracted Bragg angles in terms of the acoustic frequency is then obtained, leading to the derivation of the deflection passband characteristics, with optical activity taken into account when close Z-axis optic beam propagation is considered.

A detailed experimental program has been carried out to measure the unknown terms of the photoelastic tensor of tellurium as well as to measure the deflection passband characteristics in

typical cases with specific choices of interaction planes as well as optical and acoustic wave parameters. Using the known acoustic behaviour of tellurium and the complete photoelastic tensor, we have run for the first time a complete three-dimensional computer search for high figure-of-merit configurations in the isotropic case scanning the entire three dimensional space of the crystal, as well as for birefringent interactions. Hence the optimum configurations for CO_2 laser deflection and modulation have been discussed.

The complete mapping thus obtained, identifies configurations giving values of the figure of merit [M] one and two orders of magnitude larger than any previously reported.

Two of these giant M values have been verified experimentally.

DIFFRACTION ET DÉFLECTION DANS LE TELLURIUM POUR LE LASER CO_2

RÉSUMÉ

Cette thèse fait suite au travail realisé ces dix dernières années relatif aux effets acoustooptiques [AO] dans les matériaux, ainsi qu'à une première observation indiquant que le tellurium possède une valeur de mérite [M] exceptionnellement élevée à la longueur d'onde 10.6μm du laser CO_2, pour une certaine configuration de l'onde acoustique et optique. Une analyse plus générale et plus complète de la diffraction et de la déflection à des fréquences acoustiques simples et multiples est présentée ainsi que pour la première fois, les résultats d'une analyse expérimentale et quantitative de la diffraction et de la déflection AO pour les configurations biréfringentes et isotropiques qui couvrent l'espace entier du crystal.

Premièrement, l'expression de l'efficacité de diffraction est derivée pour les interactions du premier-ordre, pour une condition générale de propagation acoustique et optique. Une expression complète de la valeur de mérite est par conséquent obtenue. La relation entre les angles de Bragg incidents et diffractés en fonction de la fréquence acoustique est également obtenue. Ces dernières relations permettent de calculer les bandes passantes de diffraction et les angles de déflection correspondants,en prenant en considération l'activité optique lorsque les faisceaux optiques se propagent près de l'axe OZ.

Un programme expérimental détaillé a été entrepris afin de mesurer les coefficients inconnus du tenseur photoélastique du tellurium et les caracteristiques de diffraction AO dans des cas typiques particulièrement choisis des plans d'intéraction et des paramètres optiques et acoustiques.

Utilisant le comportement acoustique connu du tellurium et le tenseur photoélastique complet, nous avons fait fonctionner pour la première fois un programme d'ordinateur, dont le but est de calculer toutes les valeurs de [M] et en particulier celles qui sont les plus élevées, dans tout l'espace du crystal, pour les intéractions isotropiques et biréfringentes. Ainsi, les configurations optimuns pour la déflection et la modulation du laser CO_2 ont été analysées.

Les graphiques tri-dimensionels représentant les valeurs de [M] ainsi obtenues, identifient des configurations pour lesquelles certaines de ces valeurs sont de deux ordres de grandeur supérieures à celles préalablement publiées.

Deux de ces valeurs géantes, ont été vérifiées expérimentalement.

ACKNOWLEDGEMENTS

It is a pleasure for the author to thank his thesis adviser, Professor Arshavir A. Gundjian, for the help and guidance extended throughout this work. I am also grateful to Professor Farnell, Professor Adler, Dr. Jen and Dr. Oliveira, for many useful discussions and for their work in the field of acoustics and AO interactions.

The author also thanks his parents, whose continuous support allowed the succesful completion of this program.

The research assistanship for the conduct of this work was provided by the National Sciences and Engineering Council and the Quebec Department of Education.

This manuscript was prepared on the McGill University System for Interactive Computing.

All computations were performed at the McGill University Computing Center.

TABLE OF CONTENTS

SECTION PAGE

SECTION PAGE

SECTION PAGE

SECTION PAGE

SECTION PAGE

SECTION **PAGE**

APPENDIX.

LIST OF TABLES

TABLE PAGE

LIST OF FIGURES

1.INTRODUCTION

1.1.Purpose of the Analysis

The design of acoustooptic systems for deflection and AM-FM modulation of laser radiation, requires the understanding of the acoustooptic [AO] properties of the crystals used.

In the last sixty years, a considerable amount of work has been done [1]-[12], to analyse theoretically and experimentally the acoustooptic effects in materials exposed to optic radiation in the visible and infrared wavelength region, using electromagnetic field theory for the propagation of light and the classical theory of acoustic beam propagation in piezoelectric crystals.

The acoustooptic parameters of many materials have lately and more recently been determined [8],[19]. In the recent work of Fukuda [1],[2], it is demonstrated that tellurium is a highly favorable material for acoustooptic Bragg diffraction at 10.6μm laser radiation, providing the highest figure of merit for diffracted laser power. The optic and acoustic behaviour of tellurium is known [1],[13],[40], but its photoelastic tensor is not completly known [2].

The purpose of this thesis is to obtain a detailed analytical and experimental investigation of AO diffration and deflection in tellurium and in doing so to measure the last remaining photoelastic coefficients. It was also the purpose to run a complete computer search for isotropic configurations covering the entire three dimensional space of the crystal, as well as for birefringent interactions, in order to characterize the optimum configurations for CO_2 laser deflection and modulation.

1.2.Organization.

Based on the formalism developed by Nelson and Lax [3], Yariv [14], Warner White and Bonner [15], Chang [12], Fukuda [2], and the discussions with Oliveira, a general expression is worked out in Chapter 3 for the diffraction efficiency, the figure of merit and the relationships between incident and diffracted Bragg angles versus acoustic frequency,with optical activity being taken into account when optical propagation is close to the crystalline Z-axis, leading to the expressions of the AO passband characteristics.

We have extended the analysis of first-order isotropic AO interactions to include the case of second-order isotropic AO interactions and multifrequency AO diffraction.

In Chapter 4 relations for the previously unknown photoelastic coefficients are derived in terms of the figure of merit [M] in strategically chosen AO configurations.

In Chapter 5, using the analytic results of chapter 3, we calculate the passband curves and the corresponding deflection characteristics of typical AO interaction configurations. The first case corresponds to an optically active birefringent mode of operation, with acoustic beam propagation along the crystalline X-axis, and optic beam propagation direction close to the Z axis. The second case corresponds to acoustic beam propagation 4° off X-axis, eliminating the double phonon scattering dip at the center frequency of the deflector. The latter case invokes a second-order isotropic, double-phonon-scattering-free, AO interaction, where the incident ordinary polarized optic beam propagates at twice the Bragg angle from the Y axis in the XY plane.

In Chapter 6, the experimental system is described, while in Chapter 7, the unknown photoelastic coefficients are evaluated in magnitude and sign from diffraction efficiency measurements.

In Chapter 8, the analytic results of Chapter 4 concerning diffraction passband characteristics in typical AO interaction configurations are verified experimentally.

In Chapter 9, using the known acoustic behaviour of tellurium and the complete photoelastic tensor we run a complete computer search for high figure-of-merit [M] configurations in the three-dimensional space of the crystal in order to identify the most favorable regions for birefringent and isotropic interactions. Based on this analysis, a discussion follows which characterizes the optimum configurations for CO_2 laser deflection and modulation using tellurium.

In Chapter 10, this thesis is completed with a discussion and a summary of the major results obtained.

2.HISTORY AND STATE OF THE ART OF AO INTERACTIONS

2.1.Introduction

We present first in this section a chronological review of acoustooptic interactions in crystals and their applications, based on the two recent papers of A.Korpel [10], H.Young and S.K.Yao [11]. Then, the available data on measured photoelastic properties and the corresponding calculated figures of merit of materials commonly used in AO interactions are listed in Tables 1.1 and 1.2, with some of their relevant parameters and discussed in section 2-3.

2.2.History of Acoustooptics

Acoustooptic deals with the interaction of light and sound. The existence of such an interaction was predicted by Brillouin [4] in 1922 and experimental verification followed in 1932 by Lucas and Biquard [5] in France, and by Debye and Sears [6] in the US.

Brillouin's original theory predicted a phenomenon closely analogous to X-Ray diffraction in crystals. In the latter, the atomic planes cause multiple reflections of an incident electromagnetic plane wave. These reflections interfere constructively for certain critical angles of incidence to cause enhanced overall reflection (also called diffraction or scattering). In acoustic diffraction, the role of the atomic planes is assumed by planes of compression and rarefaction induced by ultrasonic waves usually with frequencies between 1MHz and 1GHz. The fact that the sound wavefronts move cause the diffracted light to be Doppler shifted. Brillouin predicted a basic Doppler shift equal to the sound frequency. This phenomenon of frequency shifting became of importance only in the past decade, and forms the basis of a coherent heterodyne detection technique in modern signal processing applications [16] [17]. Thus almost 50 years after Brillouin's analysis, all the phenomena he predicted have been put to use.

The invention of lasers as coherent light sources,the development of high-frequency acoustic transducers, and the development of materials having excellent acoustic and optical properties and large photoelastic constants [19], have generated intensive interest in the subject. Acoustooptic devices developed for the purpose of optical beam control, such as light modulators and deflectors [11],[20], are widely used in various laser applications like television scanners [21] or laser printers [22].

Finally some research has been done in order to characterize or develop acoustooptic modulators [23] and deflectors [1],[2] in the infrared region which will find an important place in the field of space communication systems or CO_2-laser radar applications [77,78,79,80,81,82].

2.3.Materials for AO interactions

Tables 1.1 and 1.2 list the state-of-the-art M values and their relevant properties for infrared and transparent materials in the visible wavelength region, commonly used in AO interactions.

In order to characterize and compare the acoustooptic properties of materials, a figure of merit is defined as equation (2) of Ref [1]. This value [M] varies with the sixth power of the index of refraction. Germanium and especially tellurium, which are transparent at 10.6μm have the largest [M].

The state-of-the-art highest M values for infrared materials are found for the following GaAs, Ge and Te, and are equal to:
$104x10^{-15}$, $810x10^{-15}$ and $4400x10^{-15}sec^3/Kg$,
respectively.

The state-of-the-art highest M values for the materials transparent in the visible wavelength region are found for the following As_2S_3 , TeO_2, and are equal to:
$433x10^{-15}$ and $790x10^{-15}sec^3/Kg$ respectively.

More specifically we note that many materials have their photoelastic tensor components completely known (Table 17.2 of Ref [19]). Thus a complete three-dimensional computer search for high figure-of-merit configurations in the entire crystal space can be done.

For example, in the following crystal systems (Table 17.2 of Ref [19]):

1)Isotropic:(Optical classification:isotropic).

Many materials have their photoelastic tensor components completely known in magnitude and sign. The highest M-figure is found for As_2S_3 and is equal to $345x10^{-15}sec^3/Kg$. Its photoelastic tensor is completely known and it is transparent at $1.15\mu m$.

2)Cubic:(Optical classification:isotropic).

Many materials have their photoelastic tensor components known. The highest M-figure is found for Ge and is equal to: $M=810x10^{-15}sec^3/Kg$. Its photoelastic tensor is completly known and it is transparent at $10.6\mu m$.

3)Trigonal:(Optical classification:uniaxial).

Many materials have their photoelastic tensor components known. The highest M-figures are found for the following $LiNbO_3$ and Te and are equal to:$13.5x10^{-15}$ and $4400x10^{-15}sec^3/Kg$. Their photoelastic tensor is not completly known and they are transparent at $0.63\mu m$ and $10.6\mu m$ respectively.

3)Hexagonal:(Optical classification:uniaxial).

Most materials have their photoelastic tensor entirely known. Their M-figures are small.

4)Tetragonal:(Optical classification:uniaxial).

TeO_2 has its photoelastic tensor completely known. Its M-figure is equal to: $790x10^{-15}sec^3/Kg$. It is transparent at $\lambda=0.63\mu m$.

5)Orthorhombic:(Optical classification:biaxial).

Most materials have their photoelastic tensor completely known.The highest M-figure is found for α-HIO_3 and is equal to $90x10^{-15}sec^3/Kg$. Its photoelastic tensor is not completly known and it is transparent at $\lambda=0.63\mu m$.

2.4.Conclusion

The figure-of-merit is an important parameter to characterize and compare the AO interactions in materials.It is observed that tellurium which has the highest index of refraction of all the materials considered has also the largest M. In many materials listed in Tables 1.1 and 1.2, the complete photoelastic tensor is still unknown [19]. It is necessary to determine all of the tensor components in order to determine the highest M-figures for a given material, as will be demonstrated and calculated in the following Chapters for the case of tellurium.

TABLE 1.1. SELECTED ACOUSTOOPTIC MATERIALS. (R.J.Presley, Ed.[19]).

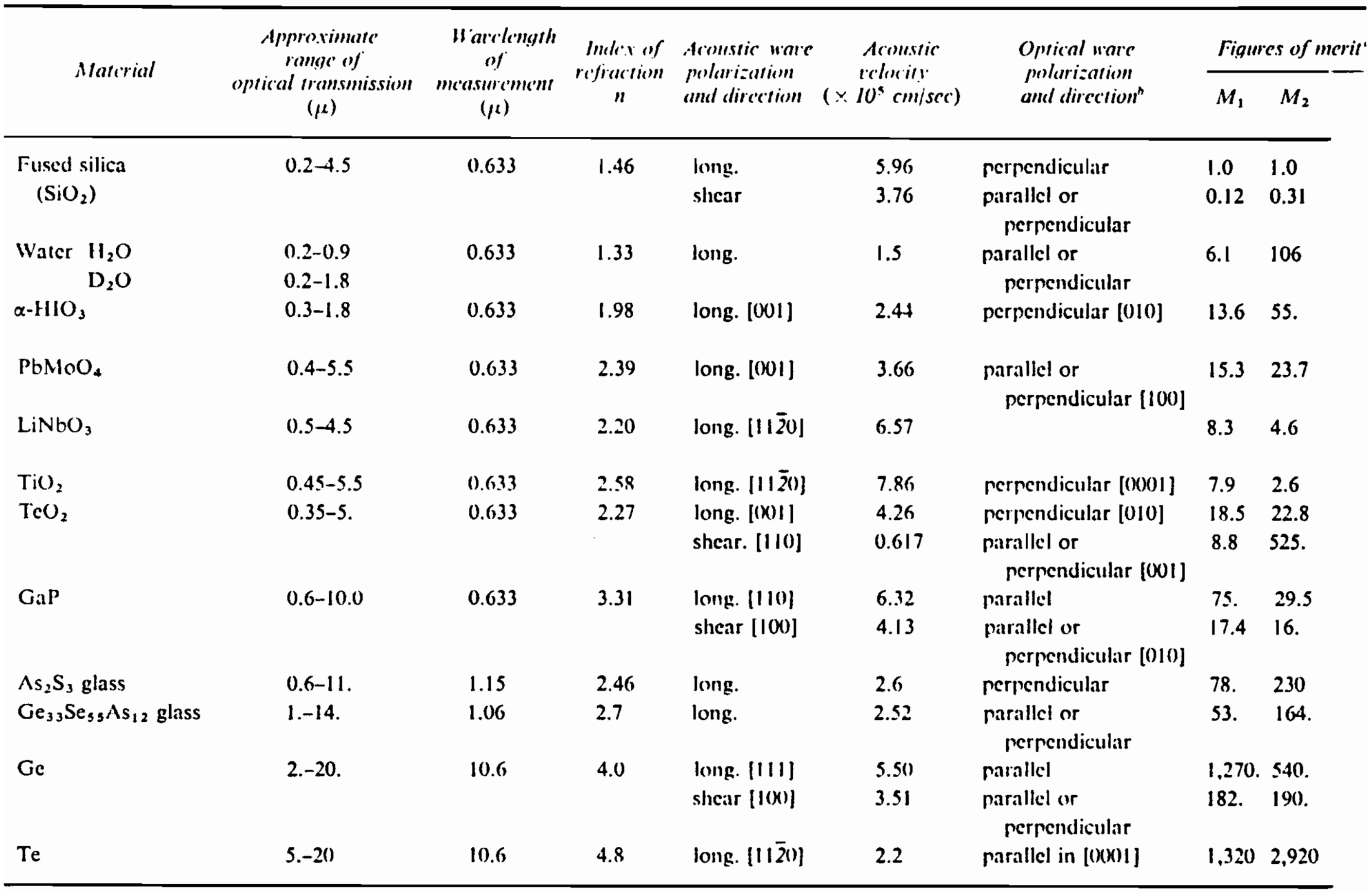

Material	*Approximate range of optical transmission* (μ)	*Wavelength of measurement* (μ)	*Index of refraction* n	*Acoustic wave polarization and direction*	*Acoustic velocity* ($\times 10^5$ *cm/sec*)	*Optical wave polarization and direction*[b]	*Figures of merit*	
							M_1	M_2
Fused silica (SiO_2)	0.2–4.5	0.633	1.46	long.	5.96	perpendicular	1.0	1.0
				shear	3.76	parallel or perpendicular	0.12	0.31
Water H_2O	0.2–0.9	0.633	1.33	long.	1.5	parallel or perpendicular	6.1	106
D_2O	0.2–1.8							
α-HIO_3	0.3–1.8	0.633	1.98	long. [001]	2.44	perpendicular [010]	13.6	55.
$PbMoO_4$	0.4–5.5	0.633	2.39	long. [001]	3.66	parallel or perpendicular [100]	15.3	23.7
$LiNbO_3$	0.5–4.5	0.633	2.20	long. [$11\bar{2}0$]	6.57		8.3	4.6
TiO_2	0.45–5.5	0.633	2.58	long. [$11\bar{2}0$]	7.86	perpendicular [0001]	7.9	2.6
TeO_2	0.35–5.	0.633	2.27	long. [001]	4.26	perpendicular [010]	18.5	22.8
				shear. [110]	0.617	parallel or perpendicular [001]	8.8	525.
GaP	0.6–10.0	0.633	3.31	long. [110]	6.32	parallel	75.	29.5
				shear [100]	4.13	parallel or perpendicular [010]	17.4	16.
As_2S_3 glass	0.6–11.	1.15	2.46	long.	2.6	perpendicular	78.	230
$Ge_{33}Se_{55}As_{12}$ glass	1.–14.	1.06	2.7	long.	2.52	parallel or perpendicular	53.	164.
Ge	2.–20.	10.6	4.0	long. [111]	5.50	parallel	1,270.	540.
				shear [100]	3.51	parallel or perpendicular	182.	190.
Te	5.–20	10.6	4.8	long. [$11\bar{2}0$]	2.2	parallel in [0001]	1,320	2,920

The Units of M_1 and M_2 are:

$M_1 X10^{-7} (sec/Kg) m^2$

$M_2 X1.6X10^{-15} (sec^3/Kg)$

TABLE 1.2. FIGURES OF MERIT FOR ACOUSTOOPTIC DEVICES.(R.W.Dixon,[8]).

Material	$\lambda(\mu)$	n	ρ(g/cm^3)	Acoustic wave polarization and direction	v(10^5 cm/sec)	Opt. wave polarization and direction^a	$M_1(n^7p^2/\rho v)$	$M_2(n^6p^2/\rho v^3)$
Fused quartz	0.63	1.46	2.2	long.	5.95	⊥	7.89×10^{-7}	1.51×10^{-18}
Fused quartz	0.63			trans.	3.76	‖ or ⊥	0.963	0.467
GaP	0.63	3.31	4.13	long. in [110]	6.32	‖	590	44.6
GaP	0.63			trans. in [100]	4.13	‖ or ⊥ in [010]	137	24.1
GaAs	1.15	3.37	5.34	long. in [110]	5.15	‖	925	104
GaAs	1.15			trans. in [100]	3.32	‖ or ⊥ in [010]	155	46.3
TiO_2	0.63	2.58	4.6	long. in [11-20]	7.86	⊥ in [001]	62.5	3.93
$LiNbO_3$	0.63	2.20	4.7	long. in [11-20]	6.57	(b)	66.5	6.99
YAG	0.63	1.83	4.2	long. in [100]	8.53	‖	0.16	0.012
YAG	0.63			long. in [110]	8.60	⊥	0.98	0.073
YIG	1.15	2.22	5.17	long. in [100]	7.21	⊥	3.94	0.33
$LiTaO_3$	0.63	2.18	7.45	long. in [001]	6.19	‖	11.4	1.37
As_2S_3	0.63	2.61	3.20	long.	2.6	⊥	762	433
As_2S_3	1.15	2.46		long.		‖	619	347
SF-4	0.63	1.616	3.59	long.	3.63	⊥	1.83	4.51
β-ZnS	0.63	2.35	4.10	long. in [110]	5.51	‖ in [001]	24.3	3.41
β-ZnS	0.63			trans. in [110]	2.165	‖ or ⊥ in [001]	10.6	0.57
α-Al_2O_3	0.63	1.76	4.0	long. in [001]	11.15	‖ in [11-20]	7.32	0.34
CdS	0.63	2.44	4.82	long. in [11-20]	4.17	‖	51.8	12.1
ADP	0.63	1.58	1.803	long. in [100]	6.15	‖ in [010]	16.0	2.78
ADP	0.63			trans. in [100]	1.83	‖ or ⊥ in [001]	3.34	6.43
KDP	0.63	1.51	2.34	long. in [100]	5.50	‖ in [010]	8.72	1.91
KDP	0.63			trans. in [100]		‖ or ⊥ in [001]	1.57	3.83
H_2O	0.63	1.33	1.0	long.	1.5		43.6	160
Te	10.6	4.8	6.24	long. in [11-20]	2.2	‖ in [0001]	10 200	4400

The Units of M_1 and M_2 are:

M_1 (sec/g)cm^2

M_2 (sec^3/g)

3.THEORETICAL ANALYSIS OF AO DIFFRACTION IN UNIAXIAL CRYSTALS.

3.1.Introduction.

The basic theory of acoustooptic interactions in uniaxial crystals is well understood [7] [9] [12] [46]. When an acoustic wave propagates in a material, it produces a periodic modulation of the index of refraction via the elastooptical effect and this modulation can diffract a light beam incident on it.

The diffraction of a plane wave monochromatic light beam by a single sound beam has been reviewed and analysed by Klein Cook [9] using a coupled mode formulation. Later Chang [12] has generalized these results for first-order AO interactions in an anisotropic medium.

In the following section we shall present the general coupled-wave analysis of the acoustooptic interaction in an anisotropic medium based on the work of Chang [12], and discussions with Oliveira [37]. We have extended this analysis to include the case of second-order isotropic interactions.

From the results obtained above, we have generalized the coupled-wave formulation of Hecht [46] in the Raman Nath Regime (thin ultrasonic grating) and the Bragg regime (thick ultrasonic grating) for the case of multiple acoustic waves of different carrier frequencies which are now considered to be propagating in an anisotropic medium.

A general expression is defined for the figure of merit which is valid for all AO interactions. On the other hand, different expressions have been found for the diffraction efficiency for first-order interactions in the Bragg regime and for the nth diffracted beam in the Raman Nath regime.

General solutions for the diffraction efficiency have been obtained only for first-order AO interactions. For second-order isotropic AO interactions and multifrequency AO interactions, approximate solutions are given.

3.2.General Expression for the Diffraction Efficiency and the Figure of Merit for Single-Acoustic-Frequency, First-order Interactions.Plane Wave AO Interactions.

3.2.1.General Considerations.

Figures 3-1a,b show the basic configuration of acoustic and optic beams involved in a general anisotropic AO diffraction interaction. The general plane of interaction is the X*Z* plane. The acoustic wavevector $\vec{K}_A$ is chosen along X* and makes an angle δ_a with the acoustic Poynting vector assumed to be directed along the boundary of the acoustic column. The optic wavevectors $\vec{K}_I$, $\vec{K}_D$ for the incident and diffracted optic beams make an angle Θ_I^*, Θ_D^* respectively near the Z* axis in the X*Z* plane. In this general case a change of the polarization directions can take place with the optic beams. Also the finite deviation of the optic propagation direction from the Poynting vector due to the optical anisotropy is taken into account.

P_e in figure 3-1a is the incident acoustic beam power which results in a distributed acoustic strain that in turn through the AO effect results in an induced electric polarization vector $\Delta\vec{P}_D$

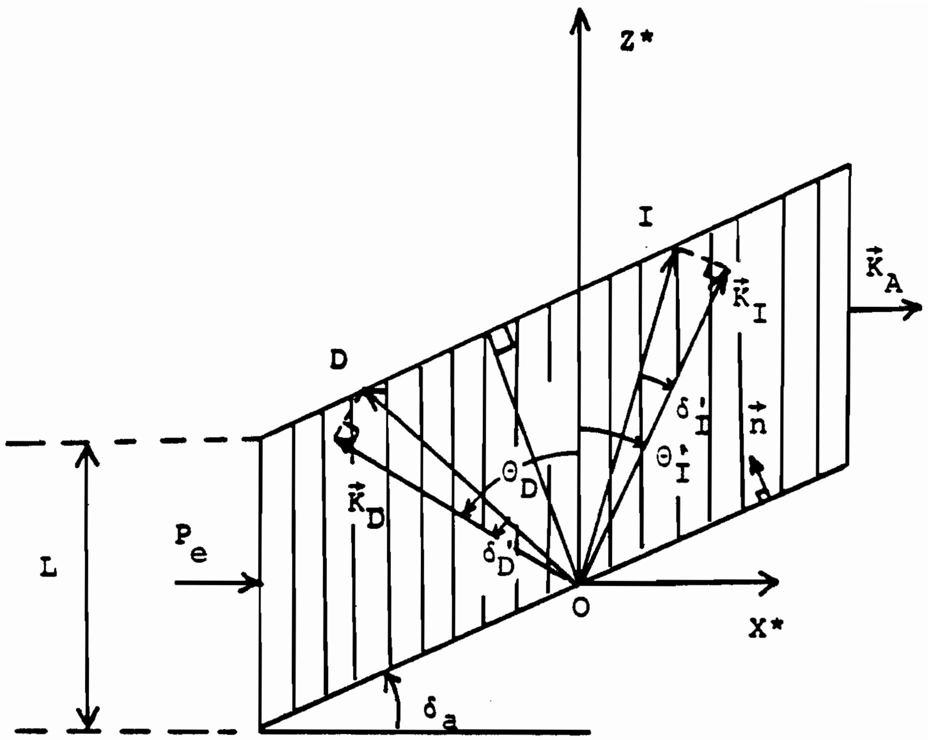

Figure 3-1a. Geometrical characteristics of the acoustic column in the X*Z* interaction plane rotated from the X,Y,Z axes by the three Euler angles ϕ,Θ,ψ. OI is the length of interaction of the incident optic Poynting vector projected in the X*Z* plane. δ' is the optic power flow angle in the X*Z* plane. δ_a is the acoustic power flow angle in the X*Z* plane. The acoustic direction wavevector $\vec{K}_A$ is along the X* axis.

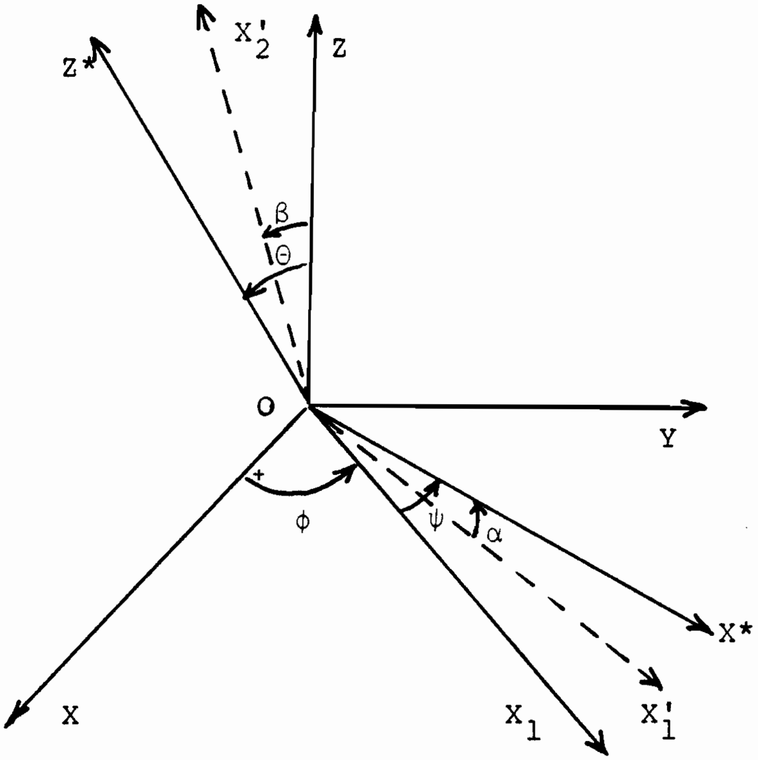

Figure 3-1b. X*Z* is the General Interaction Plane. X* and Z* define the rotated axes related to the crystalline axes X, Y, Z, through the three Euler angles ϕ, θ, ψ. X_1' is the intersection axis between the X*Z* and the XZ planes. X_2' is perpendicular to X_1' and lies in the X*Z* plane. X_1 is the X rotated axis of an angle ϕ around the Z axis.

in the crystal, where $\Delta\vec{P}_D$ is expressed as [14]:

$$\Delta\vec{P}_D = \varepsilon_o \varepsilon_{ii} \varepsilon_{jj} p_{ijkl} S_{kl} (E_I \vec{e}_I + E_D \vec{e}_D) \tag{3-1}$$

ε_o is the free space permittivity

ε_{ij} is the relative permittivity tensor element

p_{ijkl} is the Pockels photoelastic tensor element

S_{kl} is the acoustic strain field. ($S_{kl}=\frac{1}{2}S_{kl}(\vec{r},t)+$ cc.) |2,14|.

$E_{I,D}\vec{e}_{I,D}$ is the electric field vector of the incident or the diffracted optic beam.

$\vec{e}_{I,D}$ are unit vectors in the direction of $\vec{E}_{I,D}$.

The application of Maxwell's equations gives the wave equation:

$$\nabla^2 \vec{E}_{D,I} - \vec{\nabla}.(\vec{\nabla} E_{D,I}) = \mu[\varepsilon] \frac{\partial^2 \vec{E}_{D,I}}{\partial t^2} + \mu \frac{\partial^2}{\partial t^2} (\Delta\vec{P}_{D,I}) \tag{3-2}$$

Where $\vec{E}_D(\vec{r},t)$ is the resultant optic electric field after a propagation OI of the incident optic intensity. Points O and I are on the two opposite boundaries of the acoustic column.(See Fig 3-1a).

Due to optical activity in uniaxial crystals, the crystal relative permittivity tensor is given by [26]:

$$[\varepsilon] = \begin{bmatrix} \varepsilon_{11} & 2i\delta\varepsilon_{11} & 0 \\ -2i\delta\varepsilon_{11} & \varepsilon_{11} & 0 \\ 0 & 0 & \varepsilon_{33} \end{bmatrix} \tag{3-3}$$

for wave propagation along the Z optic axis.

Where δ is related to the rotatory power $\beta(z)$ in the material [15], the free-space optical wavelength λ_o and the ordinary index of refraction n_o by the relation:

$$\delta = \frac{\beta(z)\lambda_o}{2\pi n_o} \tag{3-4}$$

In tellurium, $\beta(z)=9°/mm$ (0.157rad/mm), $\lambda_o = 10.6\mu m$, $n_o=4.7939$, hence $\delta = 0.55x10^{-4}$. δ translates into an effective permittivity of $\varepsilon_o(1\pm 2\delta)$, for the slow and fast optic modes of propagation that result from optical activity [26].

For the ordinary fast optic mode, different orders of diffracted optic beam components can be identified. The nth order diffracted beam electric field is expressed as [3]:

$$\vec{E}_D = \frac{1}{2} E_D(\vec{r})\vec{e}_D e^{j[(\omega \pm n\Omega)t - \vec{K}_D \cdot \vec{r}]} + cc. \tag{3-5}$$

Where Ω is the acoustic beam pulsation frequency with the + or - sign depending on whether the sound propagation is in or opposite to the direction of propagation of the optic beam. $\vec{K}_D = \frac{2\pi}{\lambda_o} n_D(\Theta_D)\vec{e}_D$ is the diffracted beam wavevector at wavelength λ_o and diffraction angle Θ_D . $n_D(\Theta_D)$ is the index of refraction seen by the diffracted optic beam. (See Fig 3-1c).

For the case of an optically active uniaxial crystal, Warner White and Bonner [15] give, the following approximate relations for determining the indices of refraction, $n_I(\Theta_I)$ and $n_D(\Theta_D)$, in the slow extraordinary incident and fast ordinary diffracted propagating optical beams respectively (see Fig 3-1c):

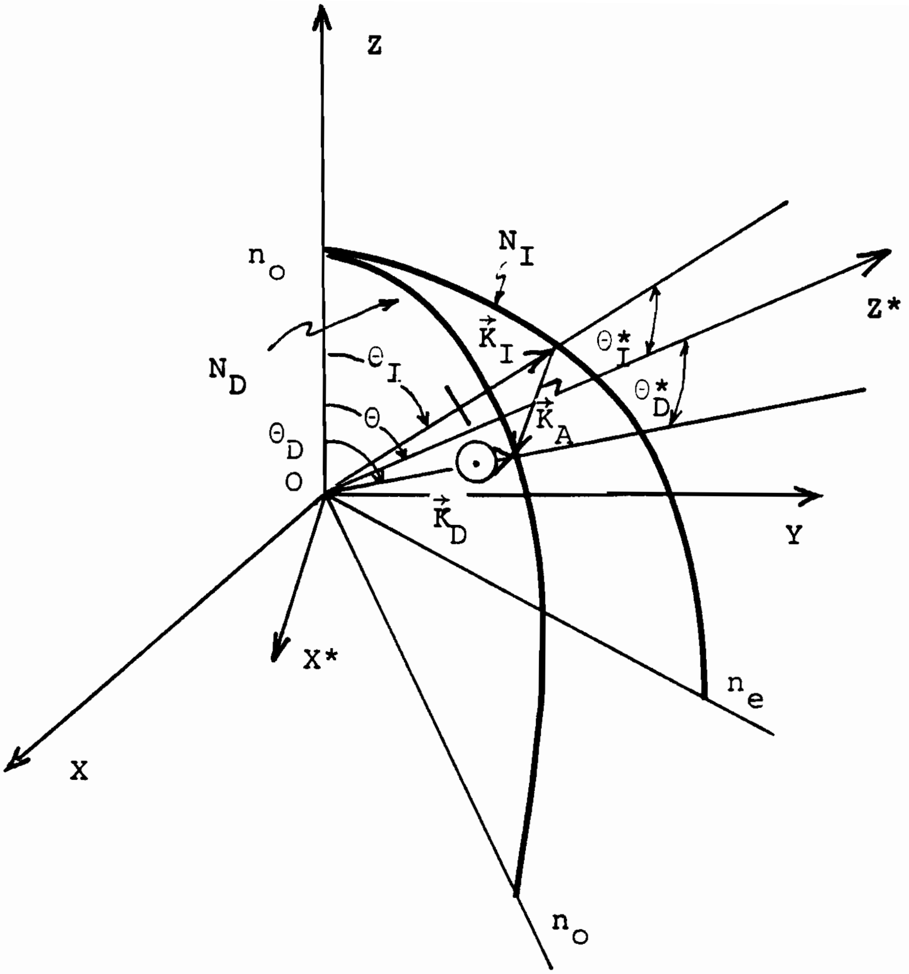

Figure 3-1c. General Wavevector diagram. X,Y,Z, are the principal crystalline axes. The rotated X*,Y*,Z* axes define the interaction plane X*Z*. With X* making an angle 0° with the direction of the acoustic wave. The allowed polarization direction for the extraordinary optic beam is in the $\vec{K}_I, \vec{Z}$ plane. The ordinary polarization direction of the diffracted optic beam is perpendicular to the Z axis. $N_I = n_I(\Theta_I)$ and $N_D = n_D(\Theta_D)$ are the indices of refraction seen by the incident and diffracted optic beams.

For the slow incident optic mode:

$$\frac{n_I^2(\Theta_I)\cos^2\Theta_I}{n_o^2(1+\delta)^2} + \frac{n_I^2(\Theta_I)\sin^2\Theta_I}{n_e^2} = 1 \qquad (3\text{-}6a)$$

For the fast diffracted optic mode:

$$\frac{n_D^2(\Theta_D)\cos^2\Theta_D}{n_o^2(1-\delta)^2} + \frac{n_D^2(\Theta_D)\sin^2\Theta_D}{n_o^2} = 1 \qquad (3\text{-}6b)$$

Where n_o=4.7939 is the ordinary index and n_e=6.2433 is the extraordinary index.

In the X*Z* interaction plane, the index of refraction loci for the extraordinary incident optic beam is an ellipse, expressed as follows,(see Fig 3-2 and Ref [45]):

$$\frac{n_I^2[\sin^2(\Theta_I') + \cos^2(\Theta_I')\sin^2\beta]}{n_e^2} + \frac{n_I^2\cos^2\beta\cos^2(\Theta_I')}{n_o^2} = 1 \qquad (3\text{-}6c)$$

where $\Theta'_I = \alpha + \Theta^*_I, \beta$, are specified in Figs 3-1b,c,2 and X_1', X_2', are the principal axes of the ellipse. The major axis has a length 2ne. The minor axis has a length $2n_o n_e/(n_o^2\sin^2\beta + n_e^2\cos^2\beta)^{1/2}$. X_1' is the intersection axis between the X*Z* plane and the XY plane. X_2' is perpendicular to X_1' and lies in the X*Z* plane. Also it can be shown that in Fig 3-1c that α and β are related to the Euler angles by the following relations:

$$\tan^2\alpha = \tan^2\Theta\sin^2\psi \quad \text{and} \quad \cos^2\beta = \cos^2\Theta/\cos^2\alpha \qquad (3\text{-}6d)$$

It is to be noted that due to optical activity, for

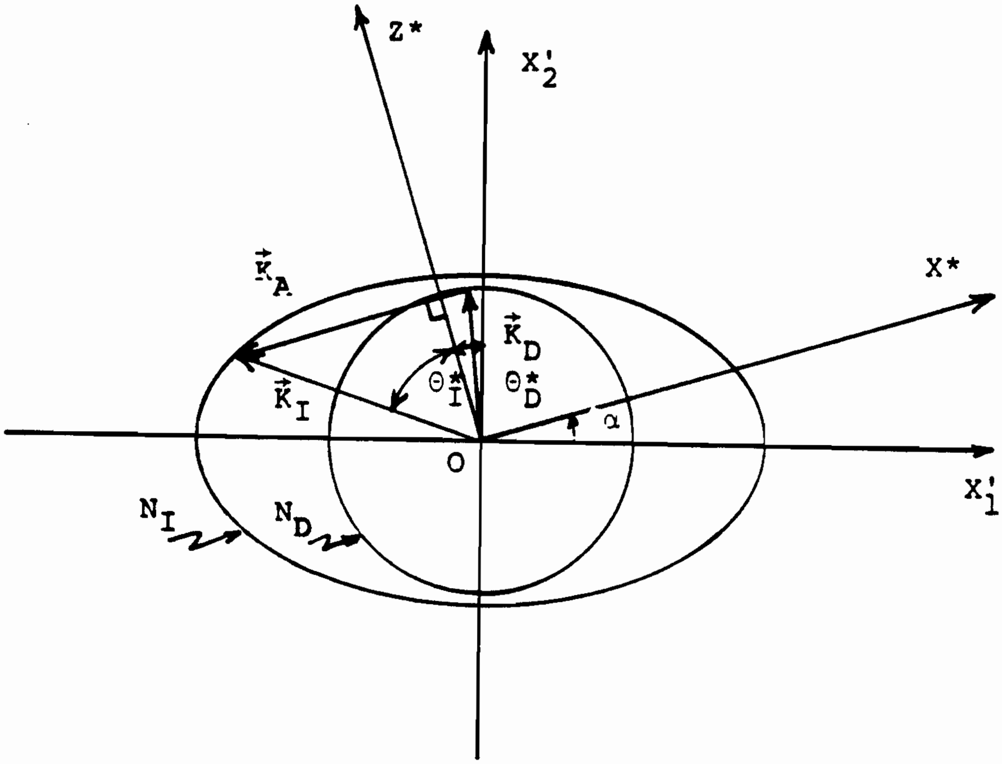

Figure 3-2. Wavevector diagram loci in the X^*Z^* plane showing AO phase matching condition. X_1' and X_2' are the principal axes of the ellipse. N_I is the index of refraction seen by the extraordinary polarized incident optic beam, $N_D=n_o$ is the ordinary index of refraction seen by the ordinary polarized diffracted optic beam.

propagation close to the Z axis, $\vec{E}_D$ is elliptically polarized and of known ellipticity in tellurium [1]. For propagation far-off the Z axis, $\vec{E}_D$ has two possible orientations: one with extraordinary polarization vector in the $\vec{K}_I$, $O\vec{Z}$ plane, and the second with ordinary polarization vector perpendicular to this plane, as shown in Fig 3-1c . To obtain the diffraction efficiency, Eq(3-2) is now solved. It should be noted that the term $\vec{\nabla}.(\vec{\nabla}\vec{E})$, neglected in previous treatments, is explicitly taken into consideration in this presentation, and hence account is taken simultaneously of the anisotropy and of the optical activity of the crystal. The problem of AO diffraction is thus treated in its exact form.

3.2.2.Solution for the Case of First-Order Birefringent Plane Wave AO Interactions.

3.2.2.1.Diffraction Efficiency

a)General expressions.

By solving Eq(3-2) in the first-order diffraction case (ie, n=1 in Eq(3-5), the coupled wave equations (3-7a) and (3-7b) that relate the magnitudes of the incident and diffracted optic beam electric fields $\vec{E}_I$ and $\vec{E}_D$ are obtained:

$$\frac{\partial E_D(r)}{\partial r_D} = \eta_D E_I e^{i(-\vec{K}_D+\vec{K}_I+\vec{K}_A).\vec{n}r} \tag{3-7a}$$

$$\frac{dE_I}{dr_I} = \eta_I E_D e^{-i(-\vec{K}_D+\vec{K}_I+\vec{K}_A).\vec{n}r} \tag{3-7b}$$

Where $\vec{K}_A$ is the acoustic propagation wavevector, and:

$$\eta_{D,I} = -i\frac{\pi}{2\lambda_o} n_{D,I}(\Theta_{D,I}) n^2_{I,D}(\Theta_{I,D}) p_{ijkl} \frac{d_i^{I,D} d_j^{D,I} \cos\delta_{I,D}}{\cos\delta_{D,I}} S_{kl} \qquad (3\text{-}8)$$

S_{kl} defines the acoustic strain field amplitude.

$\delta_{D,I}$ define the angles between the optic Poynting vector and the wavevector in the $\vec{K}_{D,I}, \vec{Z}$ plane [24]. δ' is the projection of δ in the X*Z* plane.

$n_{D,I}(\Theta_{D,I})$ are the indices of refraction seen respectively by the diffracted and incident optic beams.

d_j^D, d_i^I $(i,j=x,y,z)$ define the direction cosines of the unit vectors relative to the crystalline axes X,Y,Z in the direction of the electric displacement of the diffracted and incident optic beam. The electric field direction cosines e_i is related to d_i by:

$$e_i^D = d_i^D n_D^2(\Theta_D)\cos\delta_D / n_{ii}^2 \qquad (3\text{-}9)$$

where $n_{xx}=n_{yy}=n_o$ and $n_{zz}=n_e$.

We now solve the coupled wave equations (3-7a) and (3-7b). In Fig 3-1a we have chosen Z* along L and r along the perpendicular $\vec{n}$ to the boundary of the acoustic column assumed parallel to the Poynting vector. In this case, the following change of variables can be made, $r_D = r/\cos(\Theta_D^* - \delta_a)$ and $r_I = r\cos\delta_I'/\cos(\Theta_D^* - \delta_I' - \delta_a)$, (see Fig 3-1a). We obtain:

$$\frac{d^2E_D}{dr^2} + i\Delta k\frac{dE_D}{dr} - \eta_D\eta_I \frac{\cos\delta_I'}{\cos(\Theta_I^* - \delta_I' - \delta_a)\cos(\Theta_D^* - \delta_a)} E_D = 0 \qquad (3\text{-}10)$$

where $\Delta k = (\vec{K}_A + \vec{K}_I - \vec{K}_D)\cdot\vec{n}$

When n orders are diffracted, the term ΔkL is small [9], Eq(3-10), becomes [37],

$$\frac{dE_m}{dr} - i\,\frac{\Delta k_m}{\cos\alpha_m}\,E_m = \eta_{m,m+1}E_{m+1} - \eta_{m,m-1}E_{m-1} \qquad (3\text{-}11)$$

where m is an integer

$$\cos\alpha_m = \cos(\Theta^*_m-\delta_a-\delta'_m)\cos\delta_m/\cos\delta'_m$$

$$\eta_{m,m-1} = \frac{\pi}{\lambda_o}\left(\frac{P_A}{2LH\rho V_P^3}\right)^{1/2}\cos\delta_{m-1}p_{m,m-1}\frac{N_mN_{m-1}^2}{\cos\alpha_m} \qquad (3\text{-}12)$$

where $p_{m,m-1}$ is an effective photoelastic coefficient expressed in section 3.2.2.2.

$$\Delta k_m = \{[\vec{K}_I+m\vec{K}_A]^2-(K_oN_m)^2\}\cos\delta_m/2K_oN_m \qquad (3\text{-}13)$$

N_m is the index of refraction of the mth diffracted optic wave.

Let us solve Eq(3-10):

The boundary conditions at r=0 are:

$$E_D = 0 \quad \text{and} \quad \frac{dE_D}{dr} = \frac{\eta_D E_I(0)}{\cos(\Theta^*_D-\delta_a)} \qquad (3\text{-}14)$$

In Eq(3-10), $\Delta k = (\vec{K}_A+\vec{K}_I-\vec{K}_D).\vec{n} = \frac{\Delta k(m=1)}{\cos\alpha(m=1)}$ is the phase mismatch term. ($\vec{n}$ denotes a unit vector in the direction of the $\vec{r}$ axis).

For the case of a first-order diffracted beam, Eq(3-10) is solved to obtain the following expression :

$$\left|\frac{E_D(r=\ell)}{E_I(0)}\right|^2 = \frac{\sin^2\{G^{1/2}\}}{G} \qquad (3\text{-}15)$$

where $\ell = L\cos\delta_a$ and $G = \eta_D\eta_I\dfrac{\ell^2\cos\delta'_I}{\cos(\Theta^*_I-\delta'_I-\delta_a)\cos(\Theta^*_D-\delta_a)} + \left(\dfrac{\Delta k\ell}{2}\right)^2$

Next, in order to obtain the final expression for the diffraction efficiency, we use the following relation which expresses the intensity of an optic beam propagating in an anisotropic medium, [24]:

$$I_{D,I} = |\langle\vec{S}_{D,I}\rangle| = \frac{1}{2}\varepsilon_o c n_{D,I}(\Theta_{D,I}) E^2_{D,I} |\vec{s}\cos\delta_{D,I}| \tag{3-16}$$

where $\langle\vec{S}_{D,I}\rangle$ is the average Poynting vector for the diffracted or incident optic beam. (Watts/m²), $I_{D,I}$ is the corresponding optic power or intensity (Watts) of the diffracted and incident optic beam. $\vec{s}$ is the unit vector in the direction flow of the optic waves. $E_{D,I}$ is the magnitude of the diffracted and incident optic electric field.

Thus, the general expression for the diffraction efficiency for first-order AO interactions, is:

$$\frac{I_D}{I_I} = \eta \frac{\cos\alpha_I}{\cos\alpha_D} \cdot \frac{\sin^2\left[\eta + (\frac{\Delta k\ell}{2})^2\right]^{1/2}}{\eta + (\frac{\Delta k\ell}{2})^2} \tag{3-17}$$

where $\eta = \eta_D \eta_I (\ell^2 \cos\delta_I') / \cos(\Theta_I^* - \delta_I' - \delta_a)\cos(\Theta_D^* - \delta_a)$

$\cos\alpha_I = \cos(\Theta_I^* - \delta_a - \delta_I')\cos\delta_I / \cos\delta_I'$ and $\cos\alpha_D = \cos(\Theta_D^* - \delta_a)$

I_D and I_I are the intensities of the diffracted and incident optic beams.

This last expression ressembles that given by Chang [12], and Fukuda [2] except that now the terms $\cos\alpha_{I,D}$ and δ δ' , neglected in these previous treatments appear in this new relation of the diffraction efficiency which is expressed in its general form. In the latter relation we have assumed that no rediffraction occurs. This treatment and the different parallel analytic approach of Ref [37] are in perfect agreement.

b)Discussion.

Let us now consider the simplification of Eq (3-17). Two cases namely Θ_I^* small and Θ_I^* large are considered.

For Θ_I^* small,(ie $<6°$ inside tellurium), we are in the acoustic frequency range 0-100MHz, where the acoustic attenuation is acceptable (see section 6.3.3). Also in tellurium we can neglect the optic power flow angles.(See section 3.2.2.4). Thus Eq (3-17) reduces to:

$$\frac{I_D}{I_I} = \eta \frac{\sin^2\left[\eta + \left(\frac{\Delta k \ell}{2}\right)^2\right]^{1/2}}{\eta + \left(\frac{\Delta k \ell}{2}\right)^2} \qquad (3\text{-}18)$$

Where again $l = L\cos\delta_a$

For Θ_I^* large,(ie $\Theta_I^* > 6^0$, f<100MHz), we cannot simplify the term $\cos\alpha_{I,D}$. The latter vary significantly also at high acoustic frequencies, where the acoustic attenuation becomes high, and where modulation applications usually operate [11].

3.2.2.2.The Figure of Merit

Equation (3-8), can be written in a more compact form, since [2]:

$$|S_{kl}(\vec{r},t)| = \left|\frac{1}{2}\left(\frac{\partial u_k}{\partial x_l} + \frac{\partial u_l}{\partial x_k}\right)\right| = K_A u a_l b_k \qquad (3\text{-}19)$$

where u_k is the acoustic displacement vector component projected on the X,Y,Z crystalline axes $(k = x,y,z)$ and K_A is the acoustic wave vector magnitude. a_l and b_k, are the direction cosines for the acoustic wavevector and particle polarization, respectively. u is the acoustic amplitude.

The acoustic power density can be expressed as [26]:

$$p_a = \frac{(1/2)\rho V_P \vec{v}.\vec{v}^*}{\cos\Psi} = \frac{p_e}{\cos\Psi} \tag{3-20}$$

where, p_e is the acoustic power density delivered by the transducer and p_a is the acoustic power density inside the crystal. $\vec{v}$ is the acoustic displacement velocity vector. Ψ is the angle between the direction of propagation of the acoustic poynting vector and the acoustic propagation wavevector [26]. When the acoustic Poynting vector lies in the X*Z* plane, $\Psi = \delta_a$. Thus, using Equations (3-8,3-19,3-20) , we can write η as :

$$\eta = \frac{\pi^2}{2\lambda_o^2} M P_e \frac{\ell^2}{LH} \frac{\cos\delta_I'}{\cos(\Theta_I^* - \delta_I' - \delta_a)\cos(\Theta_D^* - \delta_a)} \tag{3-21}$$

where $P_e = p_e LH$ is the acoustic power. L and H are the dimensions of the central electrode of the transducer which define the cross section of the acoustic beam, and M is defined as the figure of merit, and is expressed as:

$$M = \frac{n_I^3(\Theta_I)\, n_D^3(\Theta_D)\, p_{eff}^2}{\rho V_P^3} \tag{3-22}$$

and $$p_{eff} = d_m^D d_n^I p_{mnkl} a_l b_k \tag{3-23}$$

p_{mnkl} are the photoelastic tensor components of tellurium.
P_e is the acoustic power delivered by the transducer.

V_P is the acoustic phase velocity

ρ is the density of the material

Θ_I, Θ_D, δ'_I are the angles shown in Figure 3-1a,c.

L and H are the length and the width of the acoustic column.

This general expression for M, is independant of the anisotropy terms δ_I and δ_D which were neglected in previous treatments [2,12],but is identical to that obtained by Fukuda [2].

3.2.2.3.Phase Mismatch Term.

The phase mismatch term, of Eq (3-13), for the configuration of Fig 3-1c, is found to be equal to: (ie at the center frequency $f=f_0$ and $\vec{K}_A \perp \vec{K}_D$).

$$\Delta k \ell = \pi \frac{\ell}{\ell_o} \left(\frac{f-f_o}{f_o}\right)^2 \qquad (3\text{-}24)$$

with $\ell_o = n_o \Lambda_o^2 \cos(\Theta_D^* - \delta_a)/\lambda_o$. Θ_D^* is the diffracted Bragg angle at the frequency f. Λ_o is the acoustic wavelength at f_0, where:

$$f_o = (V_P/\lambda_o)\left[n_I^2(\Theta_I^*) - n_D^2(0)\right]^{1/2} \qquad (3\text{-}25)$$

with $\Theta_I^* = \cos^{-1}(n_o/n_I)$

This expression is indepedant of the anisotropy terms δ and δ' and is similar to that obtained by Chang [12], except that now the acoustic power flow angle δ_a is taken into account.

When $\vec{K}_A$ is perpendicular to $\vec{K}_D$ at $f=f_0$, the phase mismatch condition can be approximately satisfied for a given incident light direction over a broad range of acoustic frequencies. Such AO geometry is a typical deflection configuration, and Eq (3-25) expresses the center frequency of the deflector, at which the minimum incident Bragg angle occurs [38]. When the incident optic beam propagates at less than 2° from the Z* axis inside the optically active region of tellurium, f_0 is low, preventing high acoustic attenuation.

3.2.2.4. Implication of the Anisotropy Terms:

The implication of the anisotropy terms is significant as demonstrated below.

From Eq (3-9), we obtain the following expression for the anisotropy terms δ_I, δ_D, for the case of extraordinary polarized optic beams:

$$\cos\delta_{I,D} = \frac{1}{n^2_{I,D}(\Theta)} \cdot \frac{1}{\{\cos^2\Theta_{I,D}/n_o^4 + \sin^2\Theta_{I,D}/n_e^2\}^{1/2}} \qquad (3\text{-}26)$$

From Eq (3-26), $\delta_{I,D}$ is maximum for extraordinary polarized optic beams and when $\Theta_{I,D} = 50°$ is equal to 14°. For ordinary polarized optic beams, $\delta_{I,D} = 0°$.

Thus, for birefringent AO interactions in tellurium, an error of at most 3% occurs in the expression of the diffraction efficiency (3-17), if the anisotropy terms are neglected. On the other hand, in the general case of biaxial crystals, the angle δ expressed by Eq (3-26), can be very large [28], and therefore the term $\cos\delta_{I,D}$ may have a very significant effect.

An expression for δ' which represents the projected optic power flow angle in the X*Z* interaction plane can be derived. In tellurium δ can be neglected. From Fig 3-1c, it can be seen that at $\Theta^*_I = 0$ and $\Theta = 0$, $\delta = 0$.

It is to be noted that in relation (3-26), δ indicates the deviation between $\vec{E}$ and $\vec{D}$ in the $\vec{K}_I$, $\vec{Z}$ plane [29].

3.2.3. First-Order Isotropic Diffraction.

In the general case of isotropic AO interactions, the plane of interaction lies in the rotated X*Z* plane. Figure 3-3a shows the first-order isotropic AO configuration. In this case, the incident optic beam propagates at the Bragg angle, the refractive indices of incident and diffracted light are equal to n_o, and the polarization directions of the ordinary polarized optic beams are perpendicular to the $\vec{K}_I,\vec{Z}$ plane [29].

Solving the wave equation (3-10), we obtain the same expression for the diffraction efficiency as Eq(3-17) but now $\Theta_I^* = \Theta_D^*$; $\delta_{I,D} = \delta'_{I,D} = 0$.

From Eq(3-13), the phase mismatch term becomes

$$\Delta k \ell = \pi \frac{\ell}{\ell_o} (F-1)F \qquad (3\text{-}28)$$

where $F=f/f_o$. Equations (3-17),(3-18), in which $\delta_{I,D}=\delta_a=0$, are identical to the expression previously derived by Chang [12].

Using Equations (3-18) and (3-28), typical curves of diffracted light as a function of frequency have been obtained; see section 3.3 , Chapter 5 and Ref [39].

3.3.Second-Order Isotropic AO Diffraction. Expression for the Diffraction Efficiency.

3.3.1.General Considerations.

In this case only isotropic AO interactions, where no change of the optical beam polarization direction takes place, will be

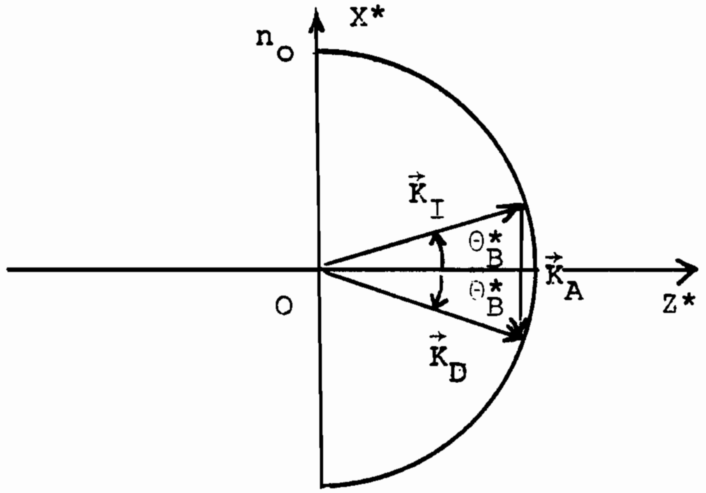

Figure 3-3a. General First-Order Isotropic Interaction Lying in the Rotated Plane X*Z*.

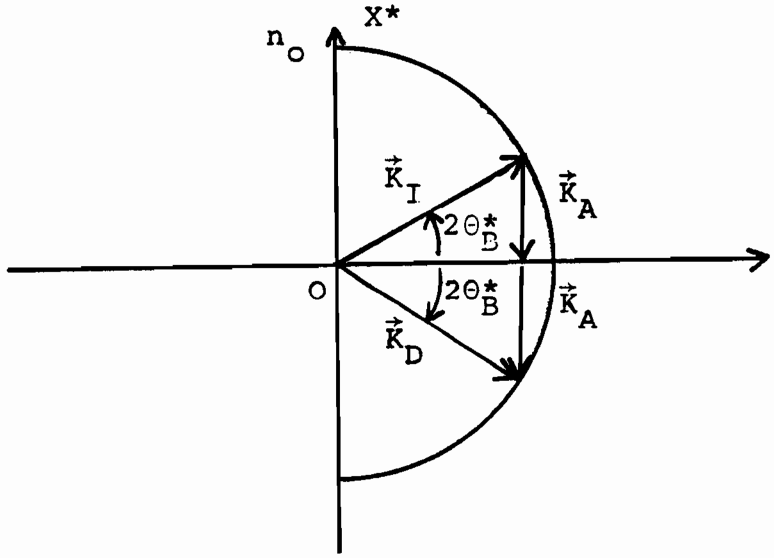

Figure 3-3b. General Second-Order Isotropic Interaction Lying in the Rotated Plane X*Z*.

considered.Reasonably high interaction efficiencies are anticipated but on the other anisotropic interactions do not yield to simple mathematical solutions with a distinctly higher figure of merit and therefore will not be considered.(See Chapter 9). Figure 3-3b shows the relative configuration of the vectors involved in this interaction. Now, the incident ordinary polarized optic beam propagates at twice the Bragg angle with respect to the axis perpendicular to the acoustic direction.

An explicit solution for the second- order diffracted beam intensity has been derived in the isotropic case by Poon and Korpel [30] and is expressed as:

$$\frac{I_{D_2}}{I_I} = \frac{1}{4}\{(\cos\chi-\cos\xi)^2+(\frac{\xi}{\chi}\sin\chi-\sin\xi)^2\} \qquad (3\text{-}29)$$

where: $\chi = \frac{1}{4}\{Q^2+32\eta\}^{1/2}$; $\xi = \frac{Q}{4}$

and Q is the Klein and Cook parameter, defined as $Q = \frac{K_A^2 L}{K_I}$ [9]. In Eq(3-17) $\eta^{1/2} = K_o \Delta n L$ is the peak optical phase delay through the medium [10], and Δn is the peak variation of the index of refraction produced by the peak acoustic strain.

3.3.2.Derivation of the Figure of Merit

The figure of merit for second-order AO interaction is obtained by noting first that complete transfer of power into the second order is predicted from Eq(3-29) for values of $Q=4m\pi$, where m is a positive integer, and [30]:

$$\eta = \pi^2\{(4n^2-m^2)/2\} \text{ for m odd} \qquad (3\text{-}31a)$$

$$\eta = \pi^2\{((2n+1)^2-m^2)/2\} \text{ for m even} \qquad (3\text{-}31b)$$

where n is also a positive integer.

It is also clear from equation (3-21), that η is proportional to the acoustic power. Thus at 100% diffraction efficiency, the acoustic power for second-order diffraction must be $2(4n^2-m^2)$ fold larger for m odd and $2((2n+1)^2-m^2)$ fold larger for m even, than the required acoustic power for 100% diffraction in first order. Furthermore, at 100% diffraction in second order, the wavevector diagram is of the same form as in the first-order diffraction except for the acoustic wavevector magnitude being $2K_A$.

In this region of 100% diffraction into second-order, we propose to fit the variations of the diffraction efficiency (3-18), into the familiar functional form when $\Delta k = 0$:

$$\frac{I_{D_2}}{I_I} = \sin^2(\eta)^{1/2} = \sin^2\left(\frac{\pi^2}{2\lambda_o^2} M P'_A \frac{\ell^2}{LH} \frac{1}{\cos^2(2\Theta_B^* - \delta_a)}\right)^{1/2} \qquad (3\text{-}32)$$

This defines P'A as:

$$P'_A = \frac{P_e}{2(4n^2-m^2)} \qquad \text{for m odd} \qquad (3\text{-}33a)$$

$$P'_A = \frac{P_e}{2\{(2n+1)^2-m^2\}} \qquad \text{for m even} \qquad (3\text{-}33b)$$

where M is the first-order figure of merit defined in previous section for the same AO configuration. P_e is expressed in (3-21). m=1 is the usual experimental condition for only a single diffracted order. In order to obtain 100% diffracted light into the second-order, it is seen from Eq (3-33a,b) that minimum acoustic power is required, and hence highest efficiency is obtained, when n = 1. This result indicates that in this case six times more acoustic power is needed to diffract 100% light into the second-order than into the first-order ($P'_A = P_A/6$).

3.3.3.Phase Mismatch Term.

Since around 100% diffraction in second-order, the wavevector diagram of the AO interaction is of the same form as in the first-order diffraction except that the acoustic wavevector magnitude is $2K_A$, the phase mismatch term in Eq(3-10) reduces to the simple form valid for an isotropic interaction as derived by Chang [12]. Here the acoustic power flow angle is also taken into account in the equations.

$$\frac{\Delta k \ell}{2} = \frac{\pi \ell}{2\ell'_o}(F-1)F \tag{3-34}$$

$$\ell'_o = n_o \Lambda'^2_o \cos(\Theta^*_D - \delta_a)/\lambda_o \text{ with } \Lambda'_o = \Lambda_o/2$$

where: F is still equal to f/f_o.

Λ_o is the excitation acoustic wavelength at the acoustic frequency f_o.

3.4.Relevant Deflection Parameters in AO Diffraction.

Diffraction Angles and Passband Characteristics.

3.4.1.General Considerations.

In deflection applications, it is useful to define, the following parameters:

a) One-half power bandwidth.

The range of acoustic frequencies Δf, where the power of the diffracted beam remains above 50% of its maximum obtainable value is defined as the half-power bandwidth of the deflector device.

b) Deflection angle

The sweep $\Delta\Theta$ in the angle of the diffracted beam corresponding to the half-power bandwidth is referred to as its deflection angle.

c) Retrace time.

The retrace time is the time taken by the acoustic beam to cross the optic beam and defines also the time taken to construct the diffracted optic beam after an angular sweep of $\Delta\Theta$.

$$\tau = \frac{w_o}{V_P} \tag{3-35}$$

Where w_0 is the optic beam width as it traverses the cross section of the acoustic beam and V_P is the acoustic phase velocity.

d) Number of resovable points.

Hawkins [69] has pointed out that the resolution criterion for acoustooptic deflectors, (see Appendix C), says that two adjacent Gaussian beams are separated if each peak is placed $1.22 \frac{\lambda}{w_o}$ apart. The resulting null depth is 24% (relative to the peaks). Therefore, the number of Rayleigh resolved spots is not just $\tau\Delta f$, the time-bandwidth product, as would be the case with uniform plane waves, but is:

$$N = (\tau\Delta f_o)/1.22 \tag{3-36}$$

Most acoustooptic deflection cells, are illuminated with a truncated Gaussian beam instead of a uniform plane wave. Typically the truncation is done by the cell aperture at the

$1/e^2$ intensity points.

e)Deflection Global Figure of Merit.

When considering different AO diffraction configurations in a given material, in order to establish a basis of comparison, we define a global figure of merit to account for the optimum combination of diffraction efficiency and number of resolvable points.

a)Isotropic Interactions:

The global figure of merit is defined here as M_1, a measure of $M\Delta f_0$, as follows:

$$M_1 = Mn_o V_P^2 = \frac{n^7 p_{eff}^2}{\rho V_P} \tag{3-37}$$

b)First-order birefringent interactions.

We will define M_1 in the following form:

$$M_1 = \frac{n_I^3 n_D^4 p_{eff}^2}{\rho V_P} \tag{3-38}$$

3.4.2.Diffraction Utilizing First-Order Birefringent AO Interaction with and without Optical Activity.

In the AO geometry of Figure 3-1c, when $f=f_0$ by definition, the direction of propagation of the ordinary diffracted optic beam is perpendicular to the acoustic direction, the AO triangle becomes right angled. This is the preferred configuration for deflection applications, because the phase mismatch condition can be satisfied over a broad range of acoustic frequencies around the center frequency f_0 [12]. When the incident angle Θ_I^* is kept constant and the acoustic frequency is varied, we obtain the passband characteristics, Δf and $\Delta\Theta$ for this mode of operation. The latter are calculated as follows:

Consider first the case when Z* coincides with the Z axis, the optic beams propagate near the Z axis and optical activity is manifested. Under these conditions, the angular sweep $\Delta\Theta$ which results from a frequency sweep Δf equal to the one-half power diffracted light bandwidth, is calculated using the approximate equation of Warner, White and Bonner [15], valid for small deviations from the Z axis;

$$\sin\Theta_I = \frac{\lambda_o}{2n_o\Lambda}\{1+4n_o^2\Lambda^2\delta/\lambda_o^2+\sin^2\Theta_I\Lambda^2n_o^2(n_e^2-n_o^2)/\lambda_o^2n_e^2\} \qquad (3\text{-}39a)$$

$$\sin\Theta_D = \frac{\lambda_o}{2n_o\Lambda}\{1-4n_o^2\Lambda^2\delta/\lambda_o^2-\sin^2\Theta_I\Lambda^2n_o^2(n_e^2-n_o^2)/\lambda_o^2n_e^2\} \qquad (3\text{-}39b)$$

Θ_I and Θ_D are described by the AO configuration shown in Fig 3-1c. In tellurium $\delta = 0.55\text{x}10^{-4}$ [38].

λ_o is the free-space optic wavelength

Λ is the acoustic wavelength

It is the middle term in the bracket of equations (3-39a,b), which is due to optical activity and is dominant only when the optical wavevector is within a few degrees of the optic axis. This raises the lowest cut-off frequency f_c from zero to approximately less than 1MHz (See Figures 5-2,5-3).

In Chapter 8, the diffraction formula expressed by equations (3-18), (3-24,28) and (3-39a,b), are calculated in typical choices of AO interactions in tellurium and verified experimentally for some of the cases.

When in the second case where Z* deviates substantially from the Z axis $\delta = 0$, Θ becomes larger, and the well-known Dixon's relations [8] are used to calculate the detailed Θ_I ,Θ_D curves versus acoustic frequency [2] [27] [37] [45].(See Figures 5-2,3).

$$\sin\Theta_I^* = \frac{\lambda_o}{2n_I(\Theta_I)V_P}\{f+\frac{V_P^2}{f\lambda_o^2}(n_I^2(\Theta_I)-n_D^2(\Theta_I))\} \tag{3-40a}$$

$$\sin\Theta_D^* = \frac{\lambda_o}{2n_D(\Theta_D)V_P}\{f-\frac{V_P^2}{f\lambda_o^2}(n_I^2(\Theta_I)-n_D^2(\Theta_D))\} \tag{3-40b}$$

On the other hand the 3dB diffracted light acoustic bandwidth is practically independant of δ, and is calculated as [12]:

$$(\frac{\Delta f_o}{f_o})^2 = 3.6\frac{n_oV_P^2\cos(\Theta_D^*-\delta_a)}{f_o^2\lambda_o\ell} \quad \text{with } \ell = L\cos\delta_a \tag{3-41}$$

Where $f_o= (\frac{V_P}{\lambda_o})[n_I^2(\Theta_I^*)-n_D^2(\Theta_D^*)]^{1/2}$ as in section 3.2.2.3 is the center acoustic frequency.

3.4.3.Diffraction Utilizing First and Second-Order Isotropic Interactions.

To obtain the passband characteristics $\Delta\Theta,\Delta f$ for the general first and second-order isotropic configuration of Fig(3-2a,b), we use the previously derived relationships [12]:

a) Isotropic first-order:

$$(\Delta f)_{ISO} = 1.8(f_o)\frac{\ell_o}{\ell} = \frac{1.8n_oV_P^2\cos(\Theta_D^*-\delta_a)}{\lambda_of_o\ell} \tag{3-42}$$

where ℓ_o is defined in section 3.2.2.3.

$$\sin(\Theta_B^*) = (\lambda_o/2V_P)f_o. \text{ Thus } \Delta\Theta_D^* = (\lambda_o/2V_P)\Delta f \tag{3-43}$$

b) Isotropic second-order:

$$\Delta f = 1.8(2f_o)\frac{\ell'_o}{\ell} = 1.8\frac{n_o V_P^2 \cos(\Theta^*_D - \delta_a)}{\lambda_o 2 f_o \ell} \qquad (3\text{-}44)$$

where ℓ'_o is defined in section 3.3.3.

$$\sin 2\Theta^*_B \simeq \lambda_o f_o / V_P \text{ ; thus } \Delta(2\Theta^*_B) \simeq (\lambda_o / V_P)\Delta f \qquad (3\text{-}45)$$

Clearly this proposed description of the second-order AO diffraction interaction provides high diffraction efficiencies and predicts the second-order AO diffracted angle to be twice as large as the first-order and the one-half power bandwidth twice smaller as the first-order isotropic interaction at the same acoustic central frequency f_0.

The quantitative relations derived up to here in this Chapter will be used to obtain the numerical results in Chapters 5 and 9.

3.5. Multifrequency AO Diffraction.

3.5.1. Introduction.

If more than one acoustic frequency is applied to an AO modulator a separate first-order beam is created for each input frequency at an angular position determined by the Θ_I ,Θ_D relationships of section 3.4.2. This effect allows the production of many separate independently modulated beams from a single input laser beam and is particularly useful in multiple character generation, radio-frequency spectrum analysis, real-time signal processing, multichannel recording, multiple beam deflection and modulation and frequency coded television display [46,47,49,50,52].

Based on the results obtained in sections 3.2, 3.4, we generalize in the following section the coupled wave analysis for the acoustooptic interaction of Hecht [46], the case of multiple acoustic waves of different carrier frequencies now considered to be propagating in an anisotropic medium. This generalizes also the results obtained by Klein and Cook in the Raman Nath regime (thin ultrasonic grating) and in the Bragg regime (thick ultrasonic grating).

3.5.2. General Multifrequency-Coupled Wave Equation. Raman Nath Regime. Thin ultrasonic grating. $Q = K_A^2 L/K_I << 1$.

Figure 3-5 shows the multifrequency AO configuration. When N acoustic waves are applied simultaneously to the transducer, as shown in Fig 3-5 the following general coupled wave equation is obtained from Eq 3-11:

$$\frac{d}{dz^*}E_D(\bar{n}) - i\left(\frac{\Delta K(\bar{n})\cos\delta_a}{\cos\alpha(\bar{n})}\right)E_D(\bar{n}) + \sum_{m=1}^{N}\{\eta_{(\bar{n},\bar{n}-a_m)}E_D(\bar{n},\bar{n}-a_m) - \eta_{(\bar{n},\bar{n}+a_m)}E_D(\bar{n},\bar{n}+a_m) = 0 \qquad (3\text{-}46)$$

where $\cos\alpha(\bar{n}) = \cos\delta(\bar{n})\cos(\Theta^*_{(\bar{n})} - \delta_a - \delta'_{(\bar{n})})/\cos\delta'_{(\bar{n})}$

$$\eta_{(\bar{n},\bar{n}\pm a_m)} = \frac{\pi}{\lambda_o}\left(\frac{P_A^m}{2LH\rho V_P^3}\right)^{1/2}\cos\delta_{\bar{n}\pm a_m}\, p(\bar{n},\bar{n}\pm a_m)\, N(\bar{n})\, N^2(\bar{n}\pm a_m)\frac{\cos\delta a}{\cos\alpha(\bar{n})} \qquad (3\text{-}47)$$

where $\Theta^*_{(\bar{n})}$, δ_a, $\delta'_{(\bar{n})}$ are specified in Figures 3-1a and 3-5. $(\bar{n})$ represents the $(\bar{n})^{th}$ diffracted field amplitude, at the acoustic frequency $f(\bar{n})$.

$f(\bar{n}) = n_1 f_1 + n_2 f_2 + \ldots.$; $\bar{n} = (n_1, n_2, \ldots, n_N)$ are positive and negative integers.

$p(\bar{n},\bar{n}\pm a_m) = (d)^i_{\bar{n}}(d)^j_{\bar{n}\pm a_m} p_{ijkl} a_l b_k$ is the effective photoelastic coefficient. $(p_{eff} = p_{(\bar{n},\bar{n}\pm a_m)})$.

$E_D(\bar{n})$ belongs to the diffracted order $G(\bar{n}) = n_1 + n_2 + \ldots + n_N$. (See Fig 3-5).

$(\bar{n}\pm a_m)$ represents $(n_1, n_2, \ldots, n_m \pm 1, \ldots, n_N)$.

The total diffracted field is expressed as follows:

$$\vec{E}_D^{TOTAL} = e^{i\omega t}\sum_{n_1=-\infty}^{\infty}\sum_{n_2=-\infty}^{\infty}\sum_{n_N=-\infty}^{\infty}\vec{e}^{D}_{(\bar{n})}E_D(\bar{n})\exp[i\sum_{m=1}^{N} n_m(\omega_m t) - i\vec{K}_{(\bar{n})}\cdot\vec{r}] \qquad (3\text{-}48)$$

where $\vec{K}_{(\bar{n})}\cdot\vec{r} = K_I(z^*\cos\Theta_I^* + x^*\sin\Theta_I^*) + \sum_{m=1}^{N} n_m K_A^m x^*$,

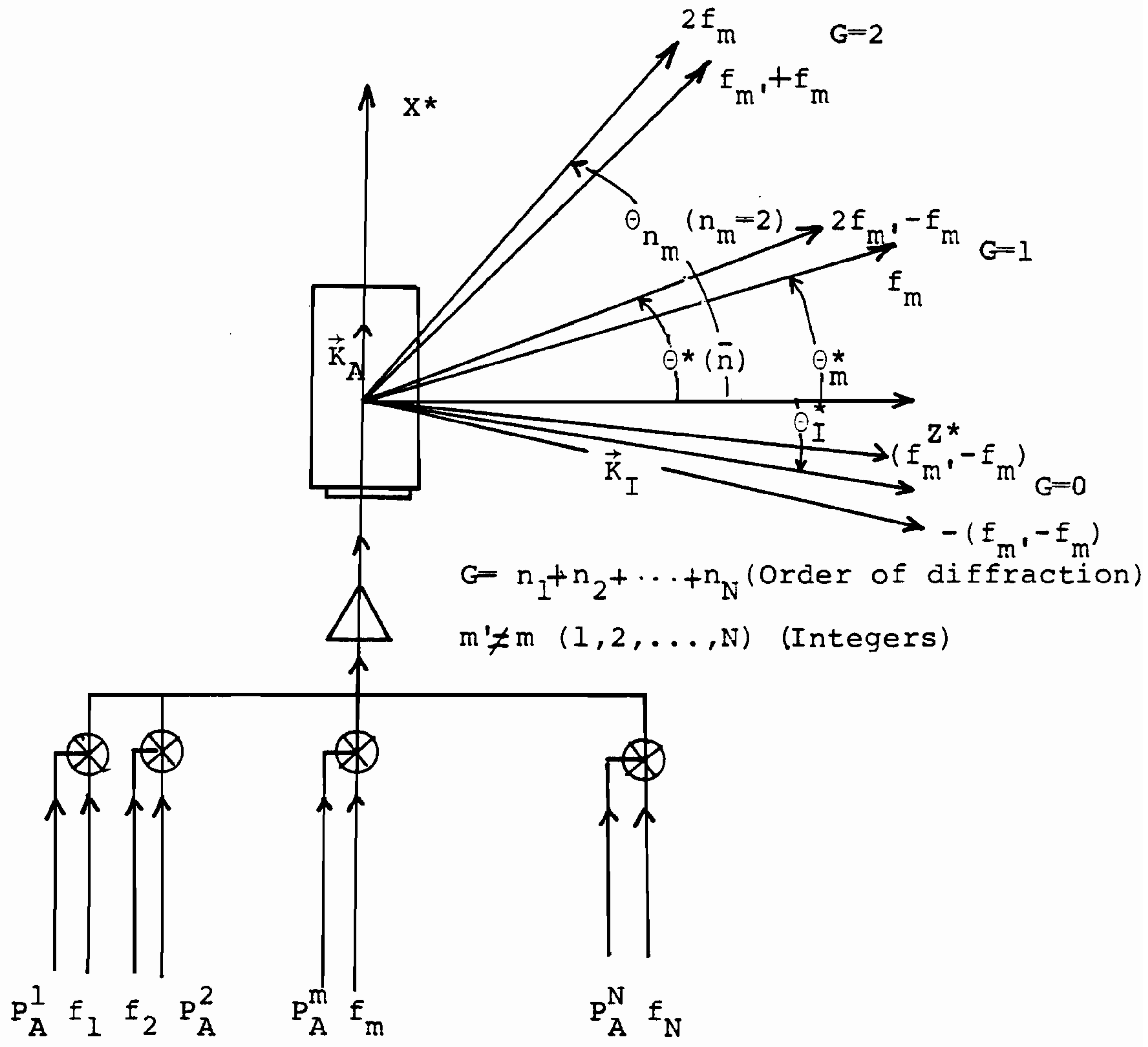

Figure 3-5. Multifrequency AO Interaction.

Θ_I^* is specified in Figure 3-5 .

$\vec{e}_D(\bar{n})$ is a unit vector in the direction of the optic electric polarization of $\vec{E}_D(\bar{n})$.

K_A^m is the mth component of the acoustic wavevector

ω_m is the corresponding acoustic pulsation frequency.

The phase mismatch term, obtained from Eq(3-13), is expressed as follows:

$$\frac{\Delta K(\bar{n})}{\cos\alpha(\bar{n})} = ([[\vec{K}_I + \sum_{m=1}^{N} n_m \vec{K}_A^m]^2 - (K_o N(\bar{n}))^2] \cos\delta(\bar{n}))/2K_o N(\bar{n}) \cos\alpha(\bar{n}) \qquad (3\text{-}49)$$

$N(\bar{n})$ is the index of refraction seen by the $(\bar{n})$th diffracted wave. $\vec{K}_o$ is the free space optic wavevector .

Eq(3-46) is identical to the coupled wave equation obtained by Hecht [46], except that now the acoustic power flow angle δ_a appears in the equation, the coefficients $\eta_{(\bar{n},\bar{n}\pm a_m)}$ and the phase mismatch term are explicitly expressed in their general form.

3.5.3.Solution for the case of Isotropic AO Interactions.

Raman Nath regime. Q << 1.

Relatively simple expressions for the diffraction efficiency can be derived from Eq(3-46) if we assume that the diffracted angles are small; in this case, we have:

$$N(\bar{n}) \simeq N(\bar{n} \pm a_m), p_{(\bar{n},\bar{n}\pm a_m)} \simeq p_{(\bar{n},\bar{n}\mp a_m)}, \delta(\bar{n}) \simeq \delta(\bar{n}\pm a_m) = 0, \eta_{(\bar{n},\bar{n}\pm a_m)} \simeq \eta_m^{1/2}$$

$$\text{where } \eta_m^{1/2} = \{\frac{\pi^2}{2\lambda_o^2} \cdot \frac{MP_A^m}{LH} \cdot \frac{\cos^2\delta_a \cos\delta'(\bar{n}) \cos\delta'(\bar{n}-a_m)}{\cos(\Theta^*_{\bar{n}-a_m} - \delta_a - \delta'_{\bar{n}-a_m}) \cos(\Theta^*_{\bar{n}} - \delta_a - \delta'_{\bar{n}})}\}^{1/2} \qquad (3\text{-}50)$$

$$\text{with } M = \frac{N^6(\bar{n}) p_{eff}^2}{\rho V_P^3} \qquad (3\text{-}51)$$

where $\Theta^*_{\bar{n}-a_m}$ is the angle of diffraction at the order $G(\bar{n})-1$, which is assumed to be approximately constant and from Eq(3-49) $\frac{\Delta K(\bar{n})\cos\delta_a}{\cos(\Theta^*_n-\delta_a)}$ is found to be equal to [9] [46]:

$$\cos\delta_a \frac{\pi}{\ell_o}(F-2\alpha)F = \cos\delta_a \frac{Q}{2L}(F-2\alpha)F \qquad (3\text{-}52)$$

where $F=\sum_{m=1}^{N} n_m f_m/f_o$ (f_o is the midband frequency).

$Q = \bar{K}_A^2 L/n_o K_o \cos(\Theta^*_{\bar{n}}-\delta_a)$; $\alpha = (n_I K_o \sin\Theta^*_I)/\bar{K}_A$ (at $\Theta^*_I=\Theta^*_B$; $\alpha=1/2$).

$\bar{K}_A$ is the midband wavenumber ($\bar{K}_A=(2\pi/V_P)f_o= 2\pi/\Lambda_o$).

K_o is the free space optic wavevector.

n_D is the ordinary index which is equal to n_I, the index of refraction of the incident optic beam. When $\alpha=1/2$, Θ^*_I is the Bragg angle. Eq(3-52) is identical to the previously derived relations [12] [46] except that now the acoustic power flow angle is included in the equations.

We now solve Eq(3-46) with the assumption that at low acoustic frequencies the diffraction angles are small.For moderate angles of incidence at low frequencies, the numerical value of α can be large, n_m is 10 or less, $2\alpha>>F$ and at $Z^*=L$, the diffraction efficiencies are expressed as [46]:

$$I_{n_m} = |\phi_{n_m}|^2 = J^2_{n_m}\left\{V_m \frac{\sin\left(\frac{Q'\alpha'\cos\delta_a}{2}\right)}{\frac{Q'\alpha'\cos\delta_a}{2}}\right\} \qquad (3\text{-}53)$$

$$\text{Phase}(\phi_{n_m}) \simeq \cos\delta_a \frac{Q'}{L} n_m \alpha. \quad I_D(\bar{n}) = |E_D(\bar{n})|^2 = \prod_{m=1}^{N} |\phi_{n_m}(V_m)|^2 ; \; V_m = 2L\eta_m^{1/2} \qquad (3\text{-}54)$$

$Q' \simeq (K^m_A)^2 L/n_o K_o \cos(\Theta^*_{n_m}-\delta_a)$ and $\alpha'=(n_I K_o \sin\Theta^*_I)/K^m_A$. $\alpha'\simeq\alpha$.

In Eq(3-53), we note the following results:

Many diffracted orders are obtained when $Q<<1$, with relatively high diffraction efficiencies. (See Fig 2 of Ref [9]).

The diffraction pattern is symmetric at all angles of incidence since $I_{n_m}=I_{-n_m}$.

When $(Q'\alpha'\cos\delta_a)/2 = m\pi$ all $I_{n_m}=0$

Maximum diffraction will occur when the argument of the Bessel function, takes the local maximas indicated in Fig 2 of Ref [9].

Light intensities in the positive and negative nth diffraction orders will vanish at the zeros of the J_{n_m} Bessel functions.

We propose to define the figure of merit for the Raman Nath isotropic AO interactions by Eq(3-51).

The 3dB acoustic bandwidth as a function of $F=f/f_o=\sum_{m=1}^{N}\frac{n_m f_m}{f_o}$, can be calculated from Eq(3-53). Note that since $Q<<1$, the 3dB acoustic bandwidth is very large compared to the Bragg case $(Q>>1)$.

3.5.4. Solution for the case of extraordinary polarized incident and diffracted optic beams, Raman Nath regime, $Q<<1$.

For the case of extraordinary incident and diffracted optic beams, simple solutions are available if $N_{\bar n}\simeq N_{\bar n\pm a_m}$, $p_{(\bar n,\bar n\pm a_m)}\simeq p_{(\bar n,\bar n\mp a_m)}$, and $\cos\delta(\bar n)\simeq\cos\delta(\bar n\pm a_m)$. In this case, all the solutions found in the previous paragraph remain the same, but the optic power flow angles are now included in the equations. The index of refraction of the incident and diffracted optic beams are given by Eq(3-6a).

3.5.5. Solution for Isotropic AO Interaction in the Bragg Regime $Q > 1$.

Hecht [46] has solved Eq(3-46), when $Q > 1$, for the case of isotropic interactions subject to two acoustic frequencies f_1, f_2, and one diffracted order. Then he has generalized the results to N acoustic frequencies for the case of small diffracted signals and small phase mismatch term.

In order to generalize the latter results we must include the acoustic power flow angle and express V_m in a more general form, (see equation 3-50,) in the coupled wave equation of References [9] and [46].

Thus in the expressions obtained by Hecht, [46], $V_m/2L$ is replaced by $(\eta_m)^{1/2}$, (see Eq 3-54). When $V_1 = V_2$, the expression for the diffraction efficiency is found to be equal to [46]:

$$I_D = |E_D(\bar{n})|^2 \simeq J_{D_n}^2(aV) \qquad (3\text{-}55)$$

$$\text{where } V/2L = \eta^{1/2} \simeq \{(\pi^2/2\lambda_o^2) M (P_A/LH) \frac{\cos^2 \delta_a}{\cos(\Theta^*_{\bar{n}-a_m} - \delta_a) \cos(\Theta^*_{\bar{n}} - \delta_a)}\}^{1/2} \qquad (3\text{-}56)$$

$\Theta^*_{\bar{n}}$ represents the diffracted angle at $2f_2 - f_1, f_1, f_2, 2f_1 - f_2$, $(G=1)$ and $\Theta^*_{\bar{n}-a_m}$ at $f_2 - f_1, -(f_2 - f_1)$. $D_n = \sum_m |n_m|$ and $a=1$ at $f_{1,2}$, $a=2$ at $2f_{2,1} - f_{1,2}$.

Thus four diffracted optic waves are obtained at the unique diffracted order. $G = n_1 + n_2 = 1$.

No relatively simple solutions exist in the general case of birefringent multifrequency AO Bragg interactions.

3.5.6.Discussion.

A general expression has been obtained for the coupled wave equation in multifrequency AO interactions. From this equation we have been able to obtain more general expressions for the approximate expressions for the diffraction efficiencies in the Raman Nath and Bragg regime, which include for the first time the optic and acoustic power flow angles.

In Fig 7,8 of Ref [46], a comparison is shown between the two tone intermodulation spectrum obtained in the Raman Nath and Bragg regimes. $(V_m/2)^2$ is taken to be equal to 0.1; ie small signal case. From these results, we conclude than the Raman Nath regime is superior to the Bragg mode of operation for multichannel operation, since it provides sufficiently high diffraction efficiencies in the principal diffracted orders $G(\bar{n})$; (ie diffraction efficiencies occuring at $n_m f_m$, where n_m=0, 1, 2,... n_N); (see Fig 8 in Ref [46]).

In the Bragg regime no principal diffracted orders exist outside the 0 and +1 unique diffracted orders.

From the results obtained in this Chapter, we note that the same M figures of merit are found in the Raman Nath and Bragg regime in single or multifrequency AO configurations but they are associated with different diffraction efficiencies expressions.

As for the angular diffraction characteristics, they are the same as as those defined for first-order interactions.(See section 3-4).

3-6.General Expression For the Fraunhofer Diffracted Optic Field, When the Bragg Cell is Illuminated by a Plane Wave.

In the field of optical information processing [49],[50], it is important that the diffracted spot of the AO deflectors be as close as possible to the Rayleigh criterion.(See appendix D).

Cohen and Gordon [53] and Uchida [54], have expressed the one dimensional diffraction pattern and later Chang Hecht [52], and Vanderlugt [51], have expressed the two-dimensional diffraction pattern produced by a fully illuminated Bragg cell, taking into account the acoustic anisotropy of the crystal.

Neglecting the acoustic attenuation and assuming that we are just outside the Fresnel diffraction region [52] in order that the acoustic wavefront presents no aberrations,the diffracted field in the Fourier plane of a lens, is found to be equal to [51] (see Fig 3-5-1):

$$|E_D| = |\eta|^{1/2}|E_I|(\mathrm{sinc}\frac{\pi H\beta}{\lambda_o})(\mathrm{sinc}\frac{\pi L}{\lambda_o}f(\alpha,\beta)) \qquad (3\text{-}57)$$

Where $|\eta|^{1/2}$ is the diffraction efficiency in amplitude, see section 3.2.2. E_I is the incident optic beam amplitude.$L, H, \alpha, \beta, \phi$ are specified in Fig 3-5-1.

$f(\alpha,\beta)$ is the argument of the δ function [54]:

$$\delta\left[\beta^2 - \frac{\lambda_o(\alpha+\lambda_o/\Lambda)}{\Lambda(1/2-s)}\right] \qquad (3\text{-}58)$$

Where s is defined by $v(\phi)=V_p(1-s\phi^2)$ and $v(\phi)$ denotes the acoustic velocity at an angle ϕ from a zero power flow axis [56].

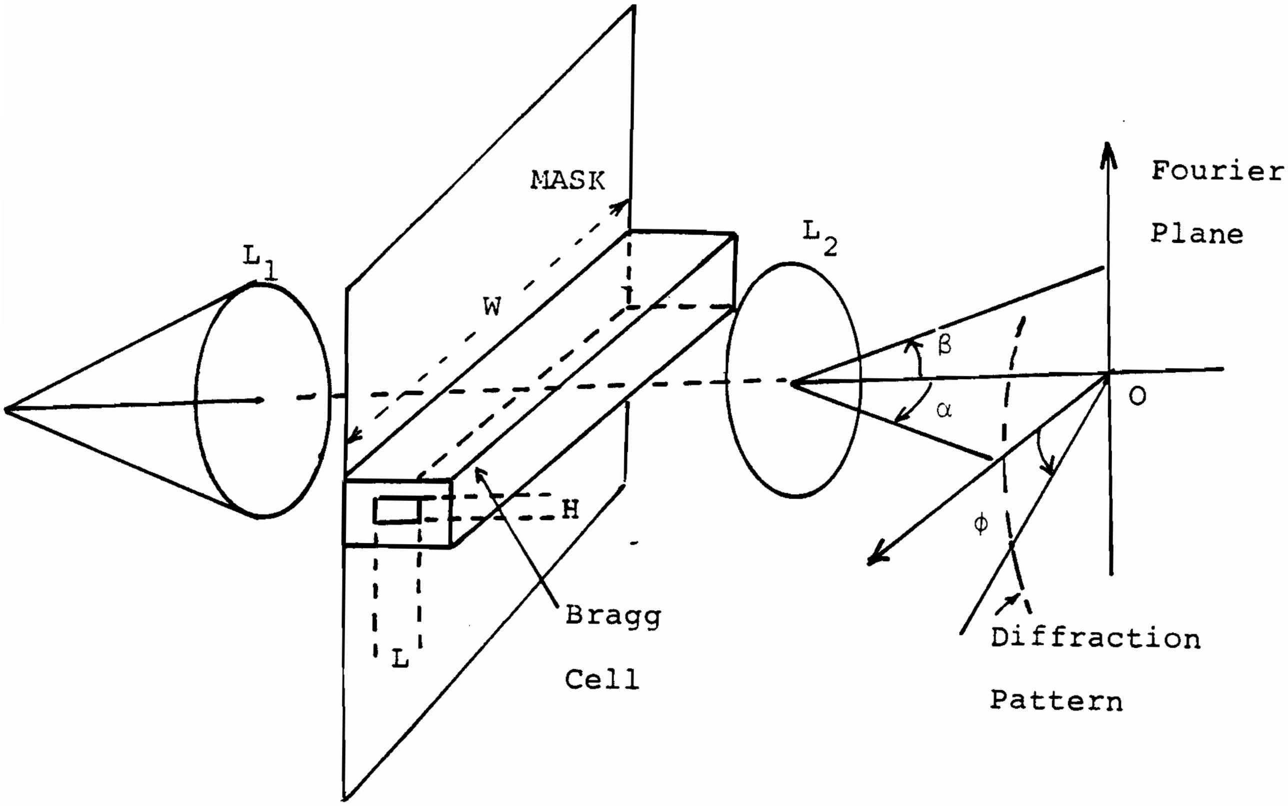

Figure 3-5-1. Fourier Transform Set-Up for Displaying Diffraction Patterns.

V_P is the phase velocity

Λ is the acoustic wavelength. λ_o is the optic wavelength. Vanderlugt [51] has discussed the influence of s on the diffraction on the diffraction pattern in detail and Uchida [54] the effect of the acoustic attenuation.

Since H is smaller than W, the diffraction pattern will be more spread in the vertical direction than in the horizontal direction. (See Fig 3-5-1).

In order to improve the resolution of the cental diffracted spot, (see Appendix C), we propose to use the set-up shown in Fig 3-5-2.

In plane P, the intensity of the central lobe of the diffraction pattern is equal to [24]:

$$\frac{I_D}{I_I} = \frac{k^2}{R_o'^2}(D)^4 \left|\frac{J_0(t)}{t}\right|^2 \quad t = \frac{2\pi D\rho}{\lambda R_o'} \quad k = 2\pi/\lambda_o \qquad (3\text{-}59)$$

where R_o', D, ρ are specified in Figure 3-5-2 .

The Fraunhofer diffraction pattern for this circular aperture is shown in Fig 3-5-3. A comparison is made with the diffraction patterns obtained at the focal plane of lens L_2 with and without the lenses L_0 and L_2. All of the optic beam crosses the acoustic beam.

The resolution has been improved by a factor 2D/H, since 2D can be made much larger than H, the gain in resolution can be very significant.

This kind of aparatus can be very useful in CO_2 laser deflectors, for which λ_o is much larger than the visible wavelength. In this case we can reach the number of resolvable

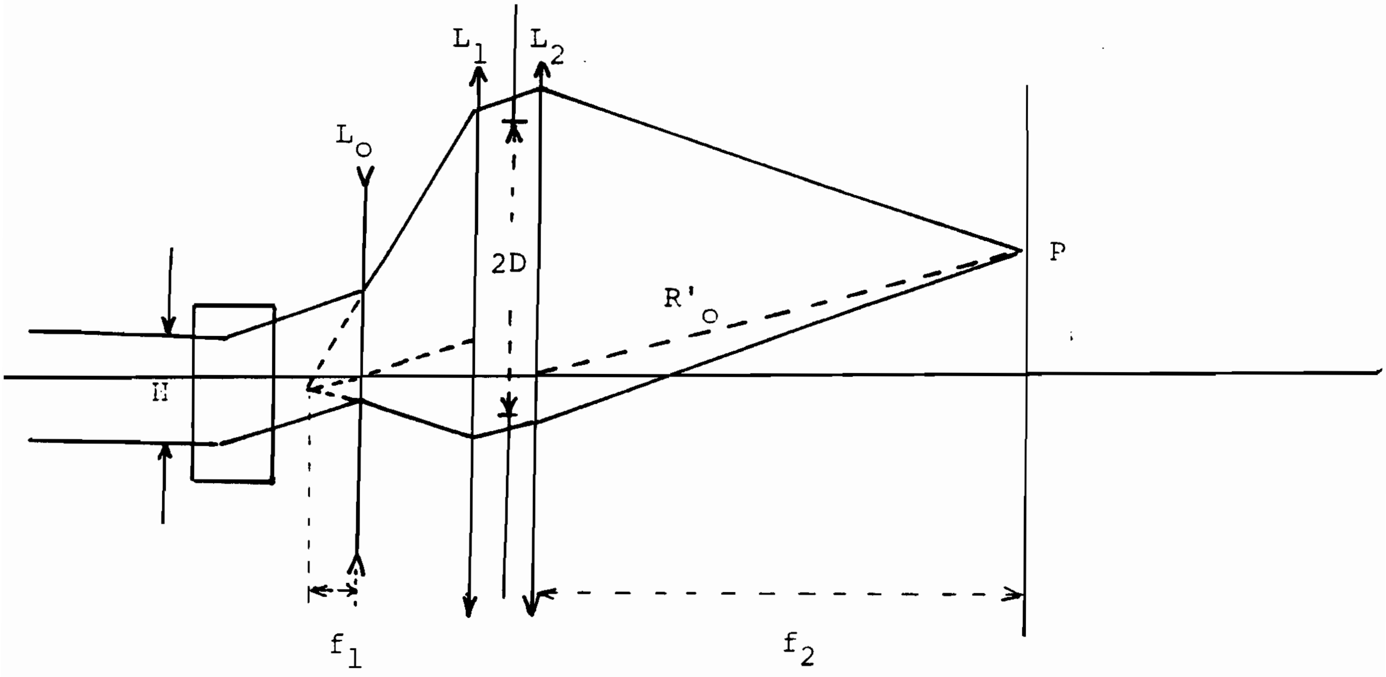

Figure 3-5-2. Propose optical set-up to improve the resolution of the central diffracted spot. L_0 is a diverging lens of focal length f_1. $L_{1,2}$ are converging lenses of focal length f_2. All of the optic beam crosses the acoustic column.

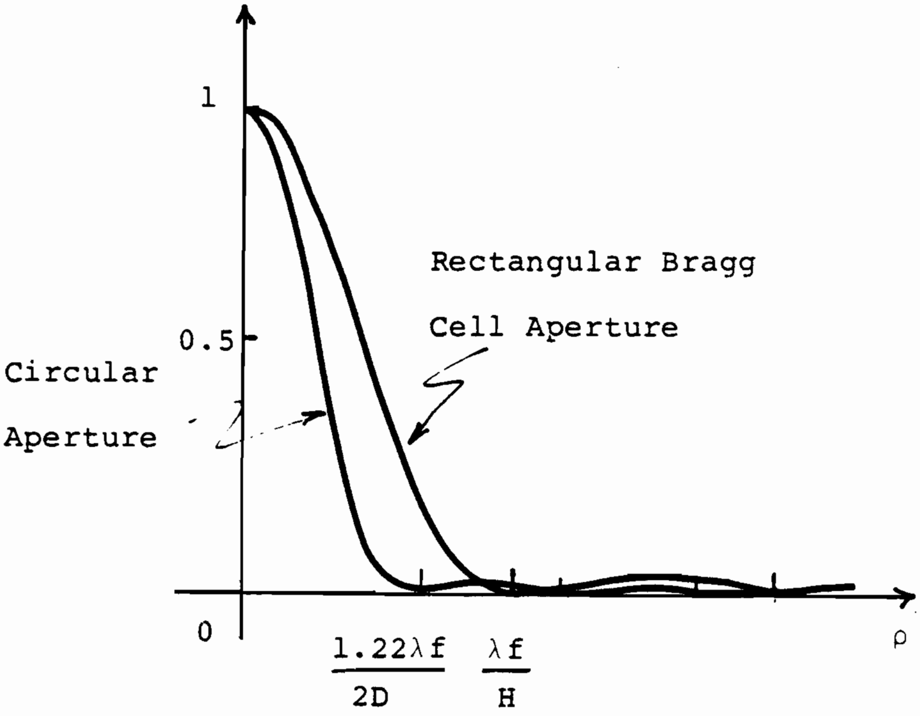

Figure 3-5-3. Fraunhofer Diffraction Pattern for the Circular Aperture. Comparison with the Diffraction Pattern Obtained with the Bragg Cell Illumination.

points obtained in the visible wavelength region.(ie of the order of a few thousands).

4.THEORETICAL DETERMINATION OF THE EXPRESSIONS FOR THE UNKNOWN PHOTOELASTIC TENSOR COMPONENTS OF TELLURIUM p_{65}, p_{56}, p_{44}.

4.1.Introduction.

In order to evaluate the figure of merit in any combination of optic beam polarization direction and acoustic parameters, the complete photoelastic tensor components of the material must be known both in magnitude and sign.

The photoelastic tensor of tellurium, a crystal of class 32, is given by:

6x6 tensor

$$\left|\begin{array}{cccccc} p_{11} & p_{12} & p_{13} & p_{14} & 0 & 0 \\ p_{12} & p_{11} & p_{13} & -p_{14} & 0 & 0 \\ p_{31} & p_{31} & p_{33} & 0 & 0 & 0 \\ p_{41} & -p_{41} & 0 & p_{44} & 0 & 0 \\ 0 & 0 & 0 & 0 & p_{44} & p_{41} \\ 0 & 0 & 0 & 0 & p_{14} & \frac{1}{2}(p_{11}-p_{12}) \end{array}\right|$$

The following photoelastic tensor components have been measured previously [2].

$|p_{11}| = 0.164$; $|p_{12}| = 0.138$; $|p_{13}| = 0.146$; $|p_{31}| = 0.086$
$|p_{33}| = 0.038$ (MKSA units).

In this section we present analytic expressions of the remaining unknown photoelastic coefficients, p_{65}, p_{56}, p_{44}.

In Chapter 7, using these latter expressions and the appropriate diffraction efficiency measurements, we evaluate these coefficients both in magnitude and sign.

In order to determine these analytic expressions, p_{eff} as given by equation (3-23) is calculated for a number of conveniently chosen different configurations where the required p_{ij} coefficients appear significantly in the expression of p_{eff}.

4.2.Calculation of p_{65}.

In order to calculate p_{65}, we have chosen the AO geometry shown in Fig 4-a , where the fast shear wave propagates along the X axis, the extraordinary incident and ordinary diffracted beams propagate in the XZ plane near the Z axis.

Using Eq(3-23), the following expression for p_{eff} is obtained:

$$p_{eff} = \cos\Theta_I (p_{66}u_2 + p_{65}u_3) \tag{4-2}$$

Where u_2 , u_3 are the direction cosines of the polarization direction of the acoustic wave and Θ_I is the angle shown in Fig 4-a.

Hence from Eq (3-22,23,4-2), we obtain:

$$p_{65} = \pm\left(\frac{M\rho V_P^3}{n_I^3 n_D^3}\right)^{1/2} \cdot \frac{1}{u_3\cos\Theta_I} - p_{66}\frac{u_2}{u_3}\cos\Theta_I \tag{4-3}$$

where M in Eq(3-21) is determined experimentally, V_P and u_2 , u_3 are calculated from the general program of Ref [40]; n_I, n_D, are

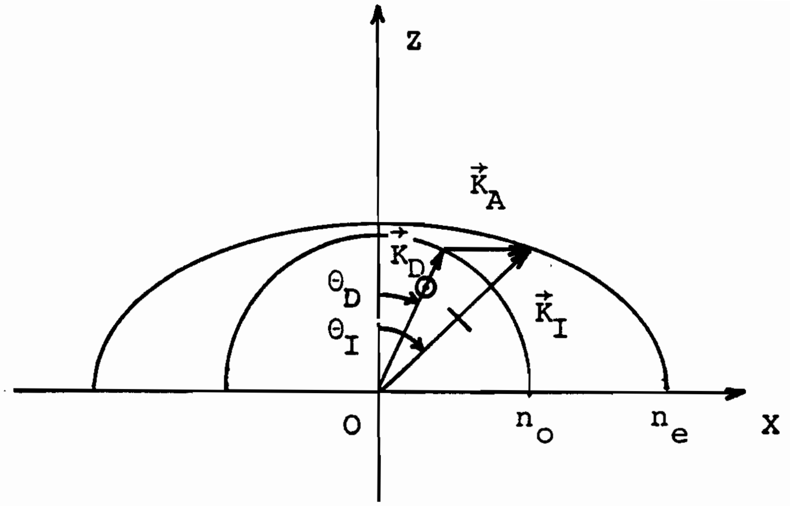

Figure 4-a. AO Geometry for the Determination of p_{65}

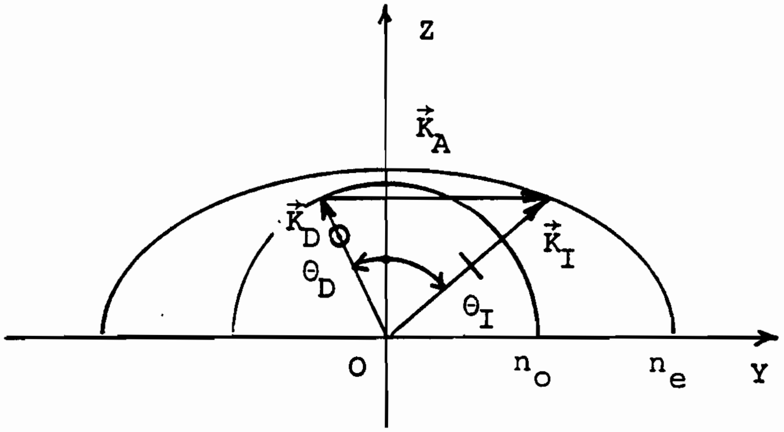

Figure 4-b. AO Geometry for the Determination of p_{56}

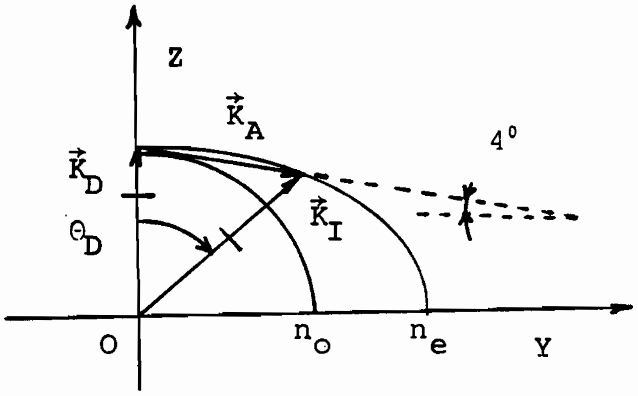

Figure 4-c. AO Geometry for the Determination of p_{44}

calculated from Eq (3-6a),(3-6b), and Θ_I, Θ_D are calculated from the following trigonometric relations:

$$K_X^I - K_X^D = K_A \quad (a) \qquad \text{and} \qquad K_X^I = K^I \sin\Theta_I \quad (c)$$

$$K_Z^I - K_Z^D = 0 \quad (b) \qquad\qquad K_X^D = K^D \sin\Theta_D \quad (d)$$

Using relations (a),(b),(c),(d), and (3-6a), we obtain:

$$\Theta_D = \Theta_I - \sin^{-1}\left(\frac{\lambda_o}{n_o V_P} f\cos\Theta_I\right) \qquad (4\text{-}4a)$$

$$\frac{n_e\cos\Theta_I}{\{n_o^2\sin^2\Theta_I + n_e^2\cos^2\Theta_I\}^{1/2}} - \cos\left[\Theta_I - \sin^{-1}\left(\frac{\lambda_o}{n_o V_P} f\cos\Theta_I\right)\right] = 0 \qquad (4\text{-}4b)$$

Where $\vec{K}_I, \vec{K}_D$ are the optic wavevectors for the incident and diffracted beams, f is the acoustic frequency, V_P is the acoustic phase velocity

4.3.Calculation of p_{56}:

For the determination of p_{56}, we have chosen the AO geometry of Fig 4-b , where the slow shear acoustic wave polarized along the X-axis propagates in the Y direction.

From Eq(3-23), we obtain the following expression for p_{eff}:

$$p_{eff} = -p_{66}\cos\Theta_I + p_{56}\sin\Theta_I \qquad (4\text{-}5a)$$

Θ_I is the angle shown in Fig 4-b. Hence:

$$p_{56} = \pm\left(\frac{M\rho V_P^3}{n_I^3 n_D^3}\right)\frac{1}{\sin\Theta_I} + p_{66}\tan\Theta_I \qquad (4\text{-}5b)$$

Where all parameters are determined in the same manner as in section 4-2.

4.4.Calculation of p_{44}.

For the determination of p_{44}, we use the AO geometry shown in Fig 4-c, where two quasi-shear waves polarized in the YZ plane [40] propagate at 4° from the Y axis in this plane.

The following expression for p_{eff} is obtained:

$$\begin{aligned} p_{eff} = {} & \cos\Theta_D(p_{22}u_2\sin 94^0+p_{24}u_3\sin 94^0+p_{24}u_2\cos 94^0+p_{23}u_3\cos 94^0) \\ & -\sin\Theta_D(p_{42}u_2\sin 94^0+p_{44}u_3\sin 94^0+p_{44}u_2\cos 94^0+p_{43}u_3\cos 94^0) \end{aligned} \tag{4-6}$$

Where u_2 , u_3 are the direction cosines of the polarization direction of the acoustic wave. For this acoustic propagation 4° off Y-axis, we calculate from [40]:

Fast shear: V_P=2519m/s; $u_1=0$ $u_2 = u_3 =-0.7$.

Slow Shear: V_P=1909m/s; $u_1=0$ $u_2 = -0.7$ $u_3=0.7$

Θ_D is calculated from the following trigonometric relations:

$$\begin{aligned} K_D\sin\Theta_D &= K_A\cos\alpha \\ K_D\cos\Theta_D &= -K_A\sin\alpha + K_I \end{aligned} \tag{4-7}$$

From Eq(4-7),we obtain the final expressions for Θ_I, Θ_D :

$$(\tan\Theta_D)^{-1} = -\tan\alpha+\frac{n_o}{\cos\alpha}\frac{\Lambda_o}{\lambda_o} \quad \text{and} \quad \Theta_I = 0 \tag{4-8}$$

Therefore, p_{44} can be estimated using Eq(4-6), in which p_{eff} is measured experimentally and Θ_D is determined from Eq(4-8).

5.DIFFRACTION PASSBAND CALCULATION FOR TYPICAL AO INTERACTION CONFIGURATION

5.1.Introduction

In this section, using the analytic results of Chapter 3 the detailed passband curves for three typical AO interaction configurations are calculated:

1)The birefringent AO interaction with X-axis acoustic propagation.

2)The birefringent AO with 4° off X-axis acoustic propagation.

3)The second-order isotropic AO interaction with X-axis longitudinal acoustic propagation.

5.2.The X-axis Birefringent AO Interaction. Calculation of the Passband Curves and the Deflection Characteristics.

5.2.1.Calculation of the Passband Curves.

Figure 5-1a shows this AO configuration, where the acoustic beam propagates along the X- axis, and the extraordinary incident and ordinary diffracted optic beams propagate close to the Z axis in the XZ plane. Equations (3-40,3-18,3-24) are used to calculate the detailed curves of the Bragg angles and the diffracted power versus acoustic frequency.

The curves obtained are shown in Figures 5-2,5-3,5-4,5-5 for the fast and slow shear waves respectively.

We note in the curves of figures 5-2,5-3, the very broad minimum of which is important for a deflection configuration.

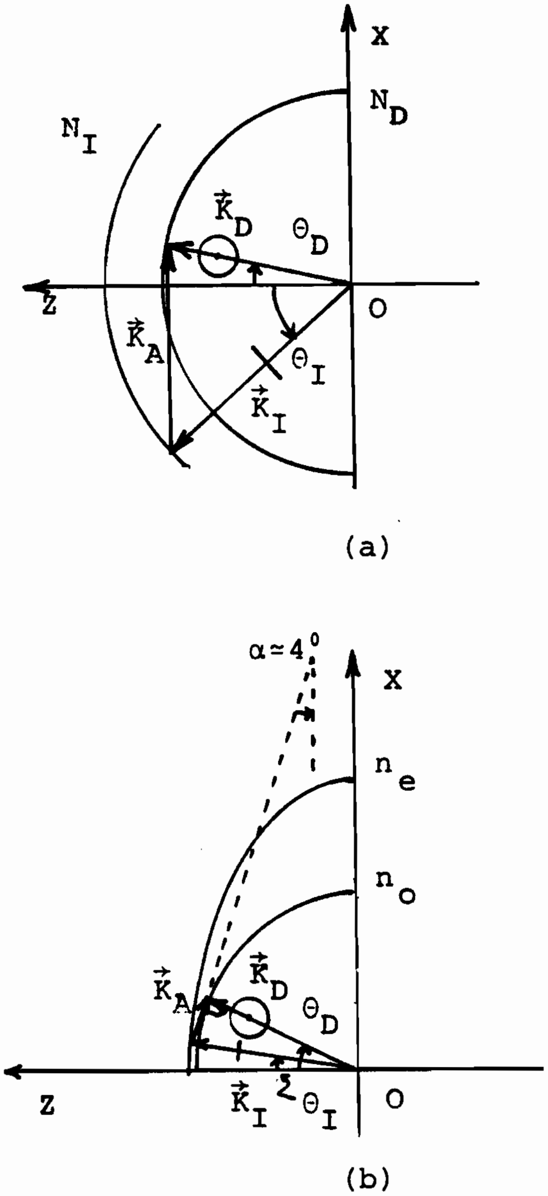

Figure 5-1 a. Wavevector Diagram for the X-Axis AO Interaction.
b. Wavevector Diagram for the 4° Off X-Axis AO Interaction.

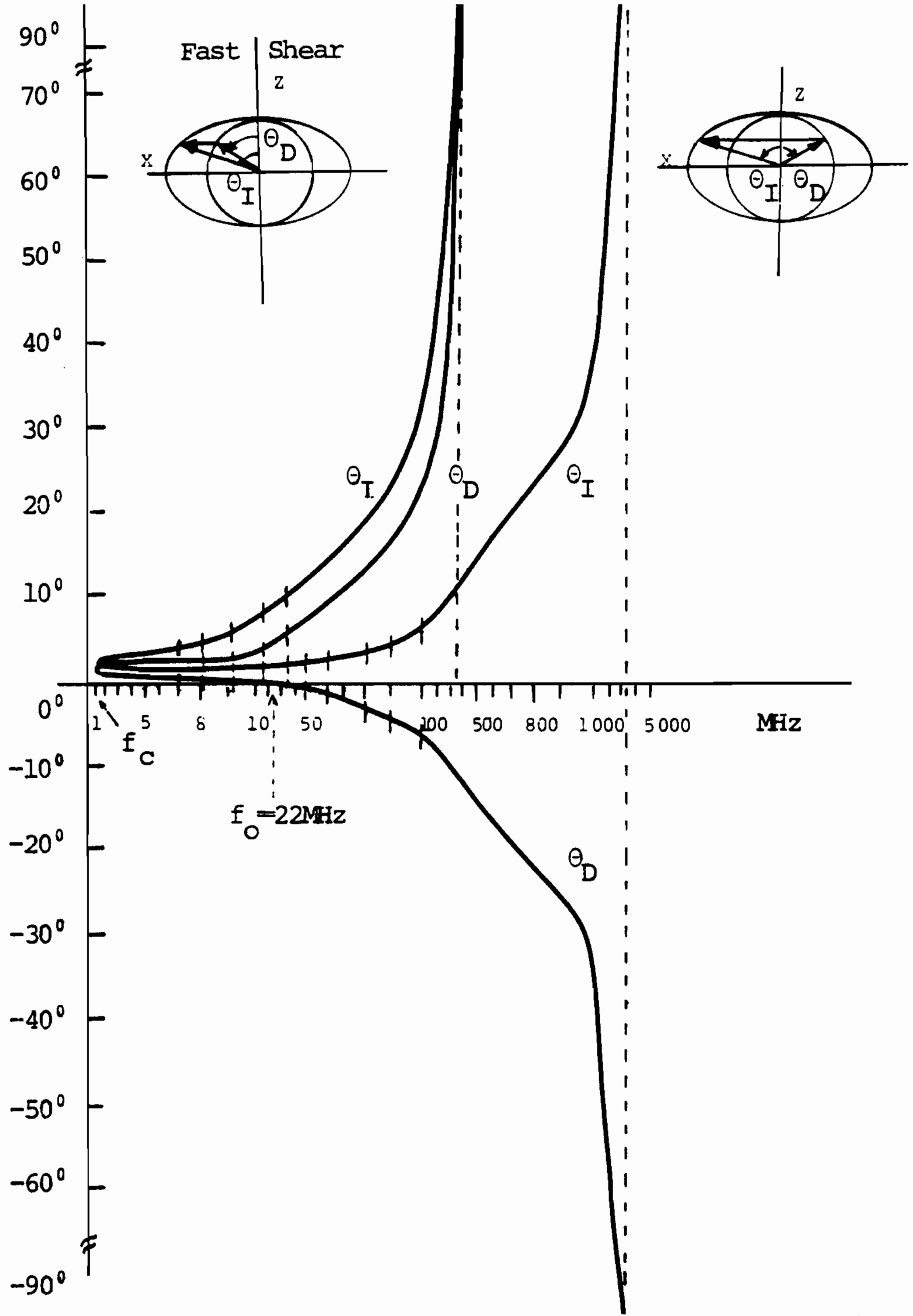

Figure 5-2. Calculated angles of incidence and diffraction inside the tellurium crystal at 10.6μm as a function of frequency for the fast shear wave propagating in the X direction at 2445m/s. The incident slow mode is diffracted into the fast mode. Also shown are experimental data points.

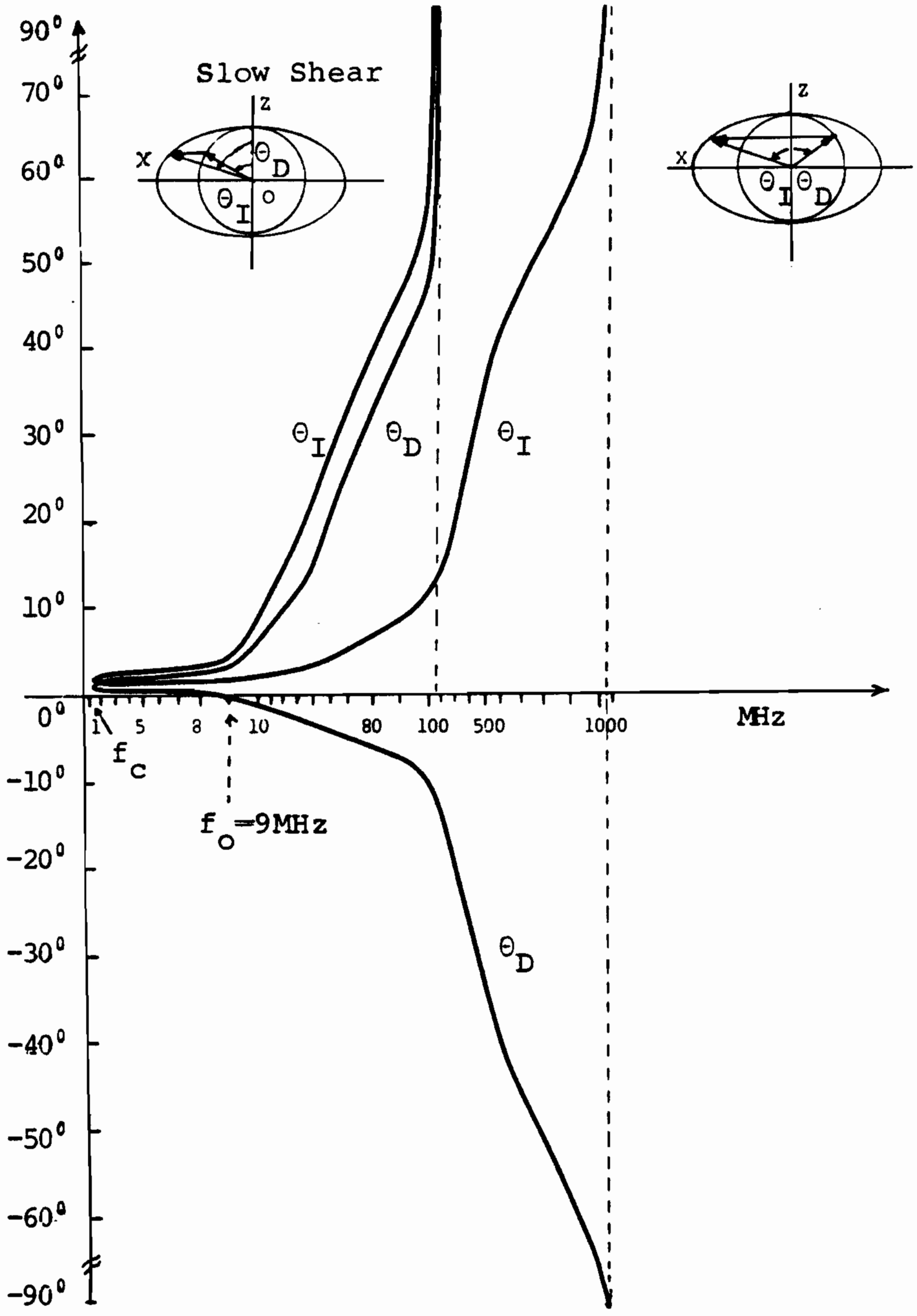

Figure 5-3. Calculated angles of incidence and diffraction inside the tellurium crystal at 10.6μm as a function of frequency, for the slow shear wave propagating in the X direction at 979m/s. The incident slow mode is diffracted into the fast mode.

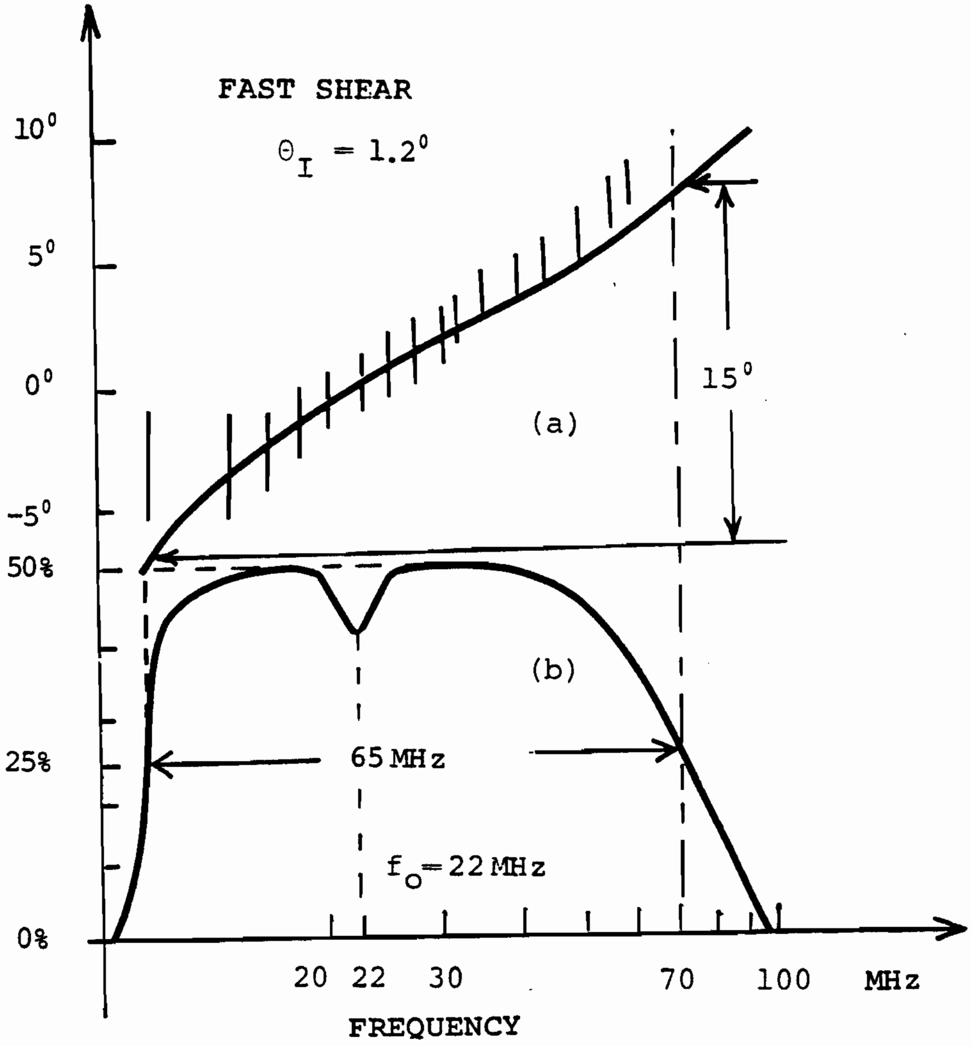

Figure 5-4. a. Calculated and measured angles of deflection outside the tellurium crystal versus frequency
b. Calculated percentage of diffracted light intensity as a function of frequency. The fast acoustic shear wave propagating in the X direction and the incident optical slow mode has $\Theta_I = 1.2^0$. The acoustic beam is 1x1mm.

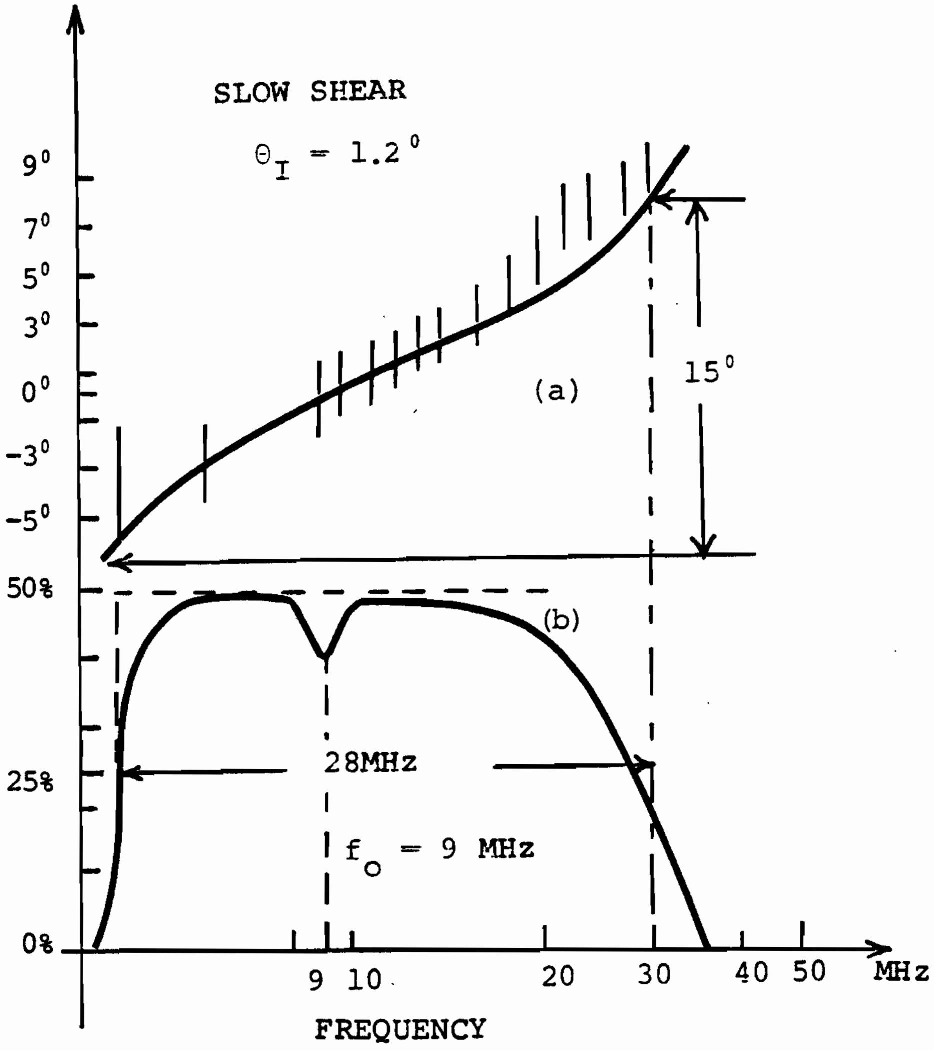

Figure 5-5a,b. Same as in figure 5-4, but the slow acoustic shear wave propagates along X.

When Θ_I is constant and Θ_D varies during the frequency sweep Δf, this minimun keeps the phase mismatch term of Eq(3-13) nearly nil and the diffracted light constant. We also note the fairly low acoustic frequencies involved which will minimize the effect of acoustic attenuation. The frequency f_o at which the minimum incident angle occurs is calculated from Eq(3-25).

5.2.2.Calculation of the Deflection Characteristics.

In Fig 5-4,5-5, the diffraction characteristics for the X-axis acoustic propagation interaction can be seen. Thus, for an acoustic beam having LxH=1x1mm, the half power diffraction bandwidth is 28MHz for the slow shear wave, the center frequency is 9MHz and the corresponding angular diffracted sweep is 15°. For the fast shear wave, the half power bandwidth is 65MHz, the center frequency is 22MHz and the corresponding angular diffracted sweep is 15°.

For values of η of Equation (3-21) in tellurium such that the diffraction efficiency at f_o does not exceed about 50% the passband shape and hence bandwidth is only slightly dependent on η. Also shown in Fig 5-4,5-5 is the double-phonon scattering dip in the efficiency which occurs at f_o. This dip is due to the fact that the diffracted light in the fast mode gets efficiently rediffracted into the slow mode at an angle $-\Theta_I$ and hence represents a decrease in the diffraction efficiency at f_o. Using the expression given by Warner, White and Bonner [15] the calculated maximum diffraction efficiency at the midband degenerate frequency is found to be 40%, and 50% at $f \neq f_o$, (see

Fig 5-4,5). At $\frac{I_D}{I_I}$=100%, the double phonon scattering dip drops to 31%. Clearly this midband degeneracy is not desirable in a deflection configuration, fortunately it can be eliminated by offsetting the acoustic wave propagation direction by a few degrees from the X-axis, as it will be demonstrated in the 4° off X-axis AO interaction.

The remaining calculated diffraction characteristics is the time of transit of the acoustic beam across the optic beam :

$$\tau = w_o/V_P \quad (w_o \text{ optic beam width})$$

$$\text{For } 2.5\mu m < w_o < 1cm \begin{cases} 1.0\,ns < \tau < 4\mu s \text{ for the fast shear} \\ 2.5\,ns < \tau < 10\mu s \text{ for the slow shear} \end{cases}$$

The small and high values of w_o correspond to a modulation or deflection configuration respectively.

The number of resolvable points is:

$$N = \frac{\Delta\Theta_o}{\lambda_o/V_P} = 310; \text{ if } w_o = 1cm$$

Thus, N=310 for both the slow and fast acoustic wave respectively with LxH=1x1mm.

5.3.The 4° Off-Axis Interaction. Calculation of the Passband Curves and the Diffraction Characteristics.

5.3.1.Calculation of the Passband Curves.

The configuration for this AO interaction with acoustic propagation 4^0 off the X axis is indicated in Fig 5-1b which shows the acoustic wavevector at 4° from the X-axis in the XZ plane. It is a double-phonon-free AO interaction because the diffracted beam cannot be rediffracted efficiently.

Similarly as in the previous section, first the Bragg angles versus acoustic frequency are calculated using Equations (3-40a,b) in which Θ has been replaced by $\Theta-4^0$ and are shown in Figures 5-6, 5-7. Then, the passband shapes and the corresponding diffracted angular sweep are calculated using Equations (3-18,3-24) and the calculated Bragg angles of Figures 5-6,5-7. The results obtained are shown in Figures 5-8,5-9.

5.3.2.Calculation of the Diffraction Characteristics

From Figures 5-8,5-9, for an acoustic column size of LxH=1x1mm, we calculate a half-power bandwidth of 27MHz for the slow shear wave and a corresponding angular diffracted sweep of 17°. For the fast shear wave the half-power bandwidth is 72MHz, the center frequency is 34MHz, and the corresponding angular diffracted sweep is 21°.

We note in Fig 5-8,5-9, that offsetting the acoustic propagation from the X-axis eliminates the double phonon scattering dip; the case when the offset is 0° both the bandwidth and the deflection angles are decreased.

The remaining calculated deflection characteristics are:

$$\tau=w_o/V_P = 4\mu s,\ 10\mu s;\ \text{with } w_o=1\text{cm}$$

for the fast and slow acoustic shear waves respectively.

$$N=\frac{\Delta\Theta_o}{\lambda_o/w_o}=360,\ 300,\ \text{with } w_o=1\text{cm}.$$

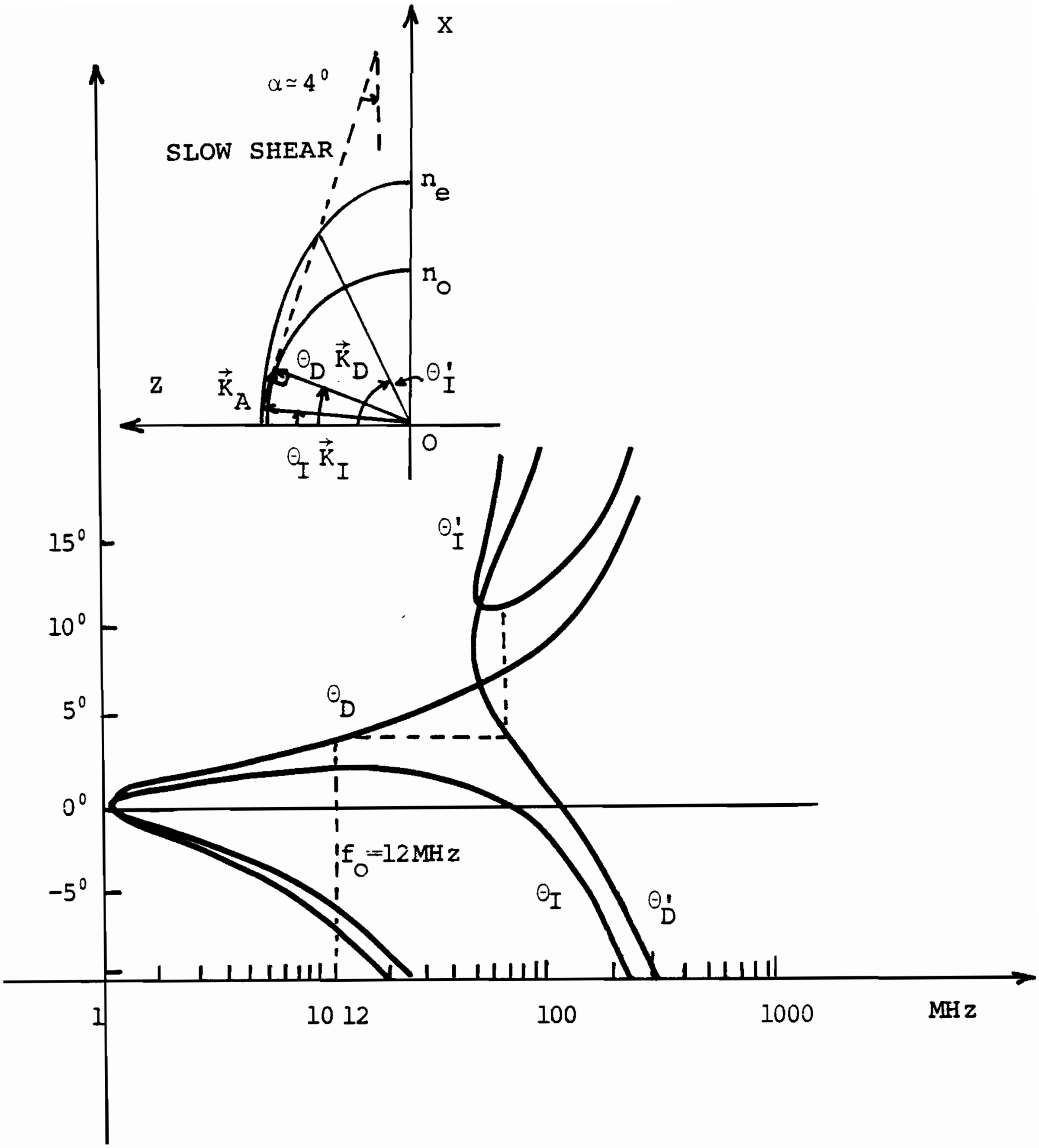

Figure 5-6. Calculated angles of incidence and diffraction inside the tellurium crystal at 10.6μm as a function of frequency, for the slow shear wave propagating at 4° from the X-axis in the XZ plane at 993m/s. The incident slow mode is diffracted into the fast mode.

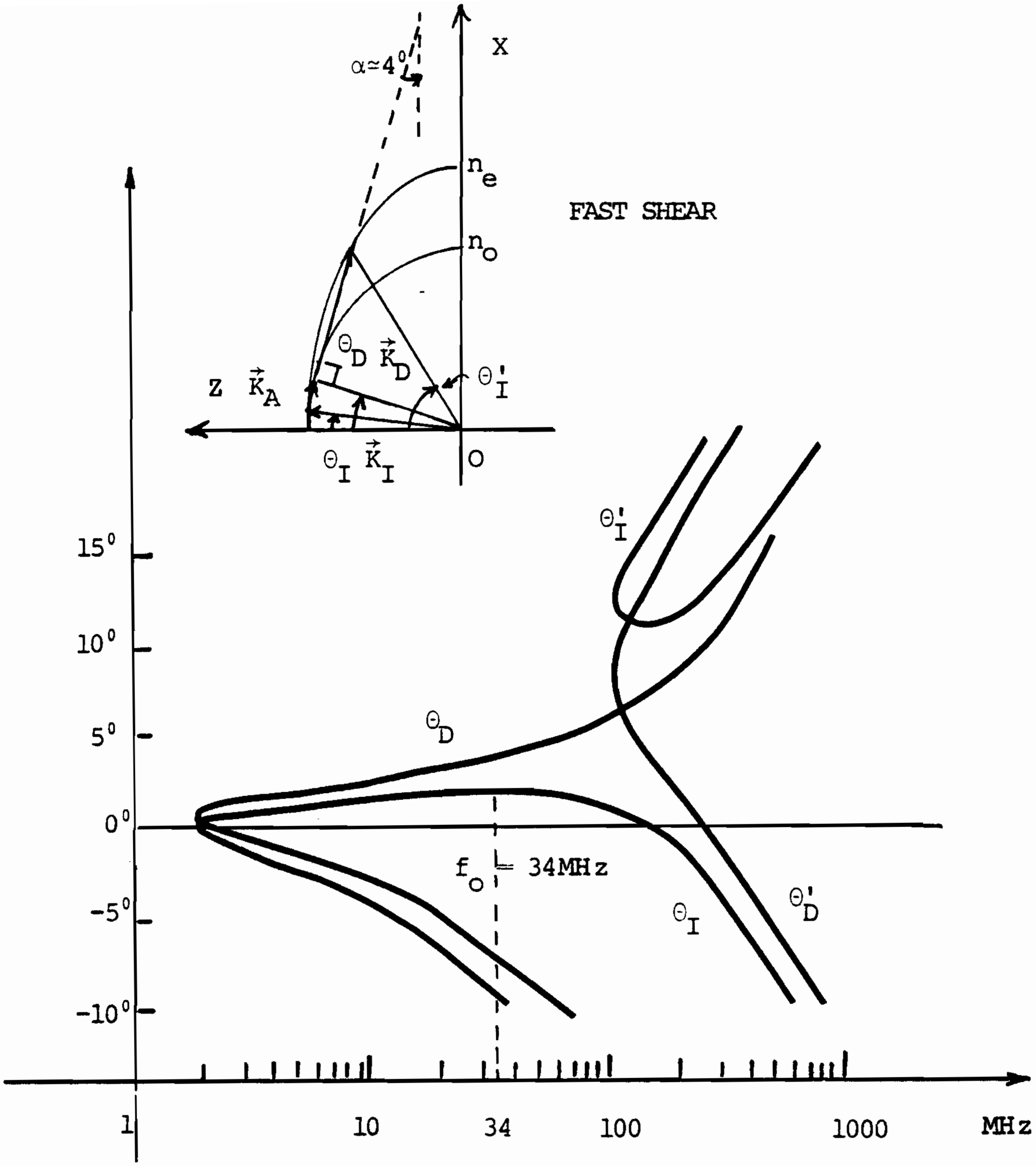

Figure 5-7. Calculated angles of incidence and diffraction inside the tellurium crystal at 10.6μm as a function of frequency for the fast shear wave propagating at 4° from the X-axis in the XZ plane at 2539m/s. The incident slow mode is diffracted into the fast mode.

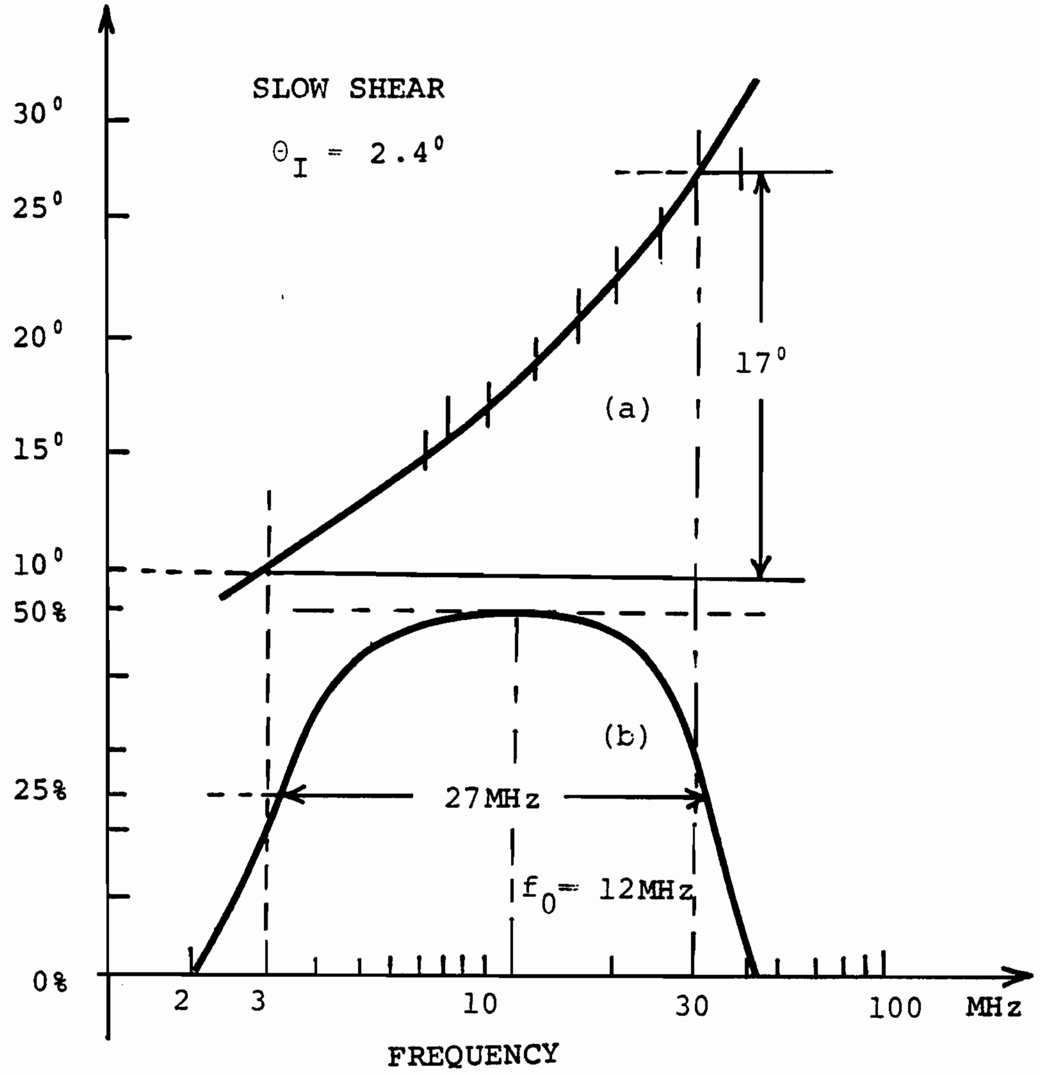

Figure 5-8. Double-phonon scattering-free, slow-shear 4° off-axis AO interaction
a. Calculated and measured angles of deflection outside the tellurium crystal versus frequency.
b. Calculated percentage diffracted light versus frequency. The incident optical mode has $\Theta_I=2.4°$ inside the crystal. The acoustic beam is 1x1mm.

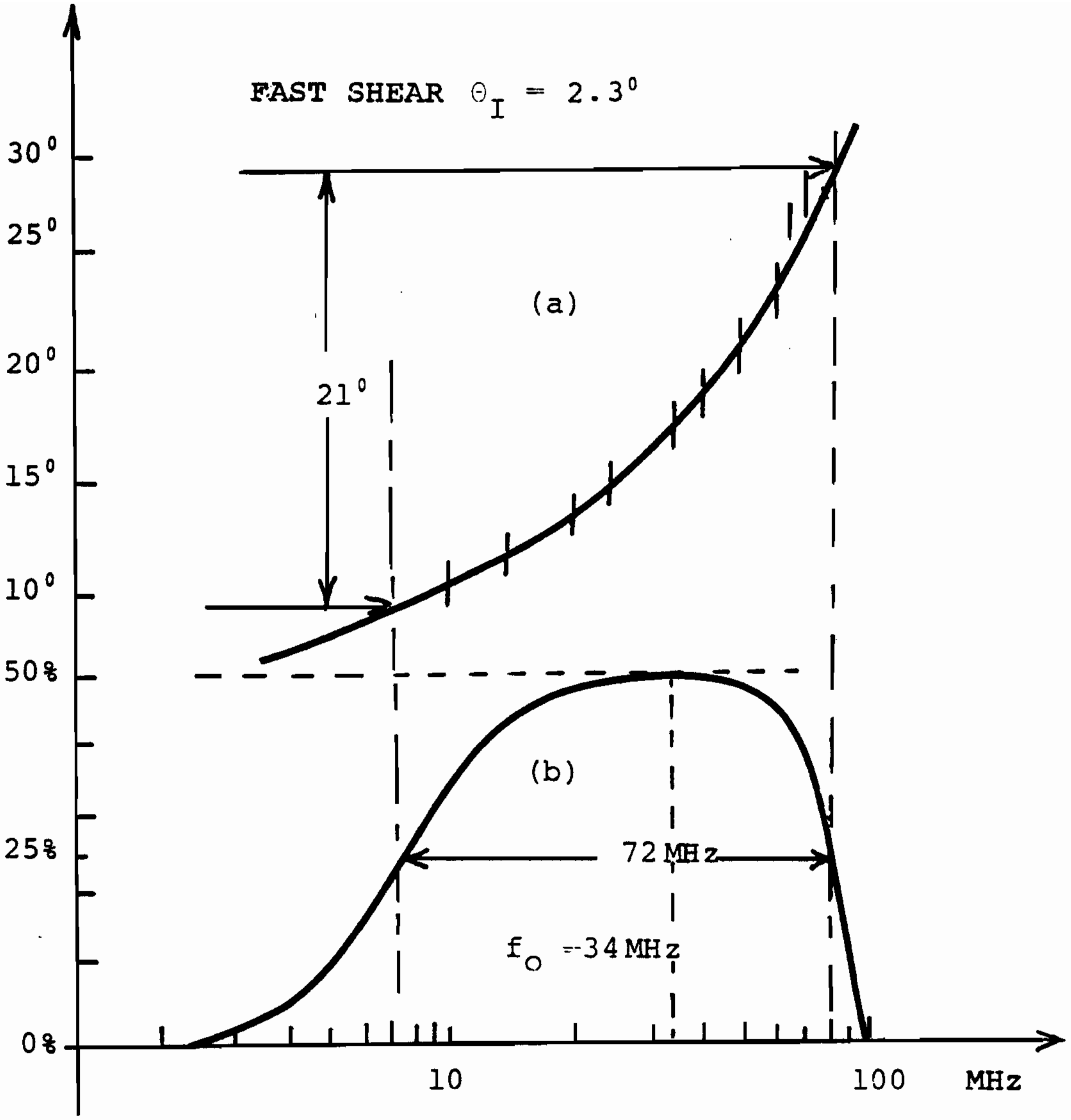

Figure 5-9. Double-phonon scattering-free, fast-shear 4^0 off-axis AO interaction.
a. Calculated and measured angles of deflection outside the tellurium versus frequency.
b. Calculated percentage diffracted light versus frequency. The incident optical mode has $\Theta_I = 2.3^0$ inside the crystal. The acoustic beam is 1x1mm.

for the fast and slow acoustic shear waves respectively.

5.4. The Second-Order Isotropic AO Interaction with X-Axis Longitudinal Acoustic Propagation. Calculation of the Diffraction Passband Curves and the Deflection Characteristics.

Figure 5-10 shows this AO geometry, where the incident ordinary polarized optic beam propagates at twice the Bragg angle with respect to the Y-axis in the XY plane, and the required longitudinal acoustic beam propagates along X.

This is also a double-phonon scattering free interaction because the diffracted beam cannot be efficiently rediffracted. (See Figure 5-10).

Equations (3-18),(3-34), (3-44) ,(3-45) are used to calculate the deflection passband characteristics. The detailed passband curves are shown in Figure 5-11, and are calculated for a 1x1mm acoustic column size. A deflection angle of 17°, outside the tellurium crystal is obtained over a half-power bandwidth of 65MHz centered at 40MHz. Thus, this second-order AO configuration has deflection passband characteristics which are comparable to the 4^0 off-axis geometry. It requires 6 times more acoustic power to diffract 100% of the incident light than the first-order isotropic case. (See section 3.3).

The other remaining deflection characteristics are:

$\tau = w_o/V_P = 4\mu s$; with $w_o = 1cm$

$N=300$ with $L \times H = 1 \times 1mm$ and $w_o = 1cm$.

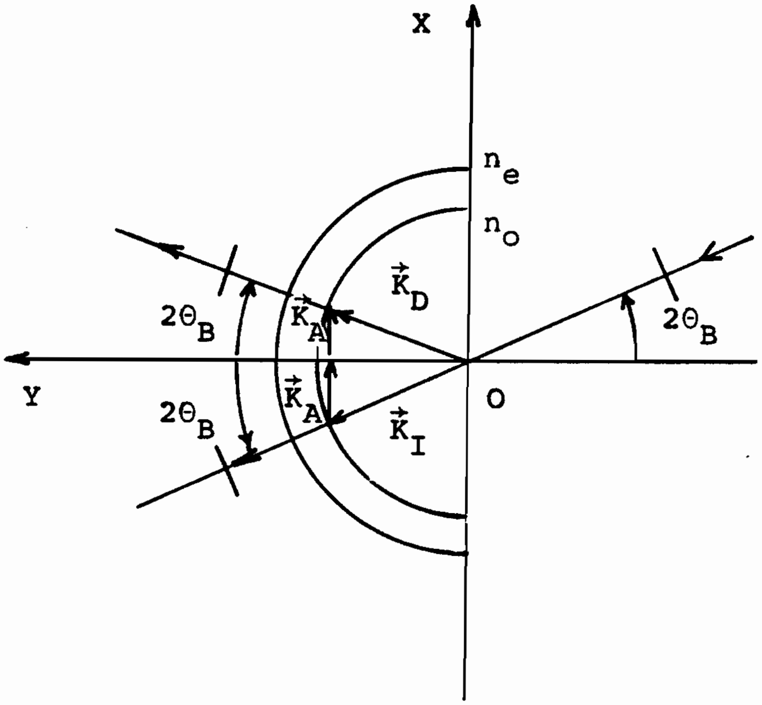

Figure 5-10. Second-order X-axis longitudinal acoustic propagation isotropic interaction. $2\Theta_B = 2.20^0$ inside tellurium. f_0=40MHz.

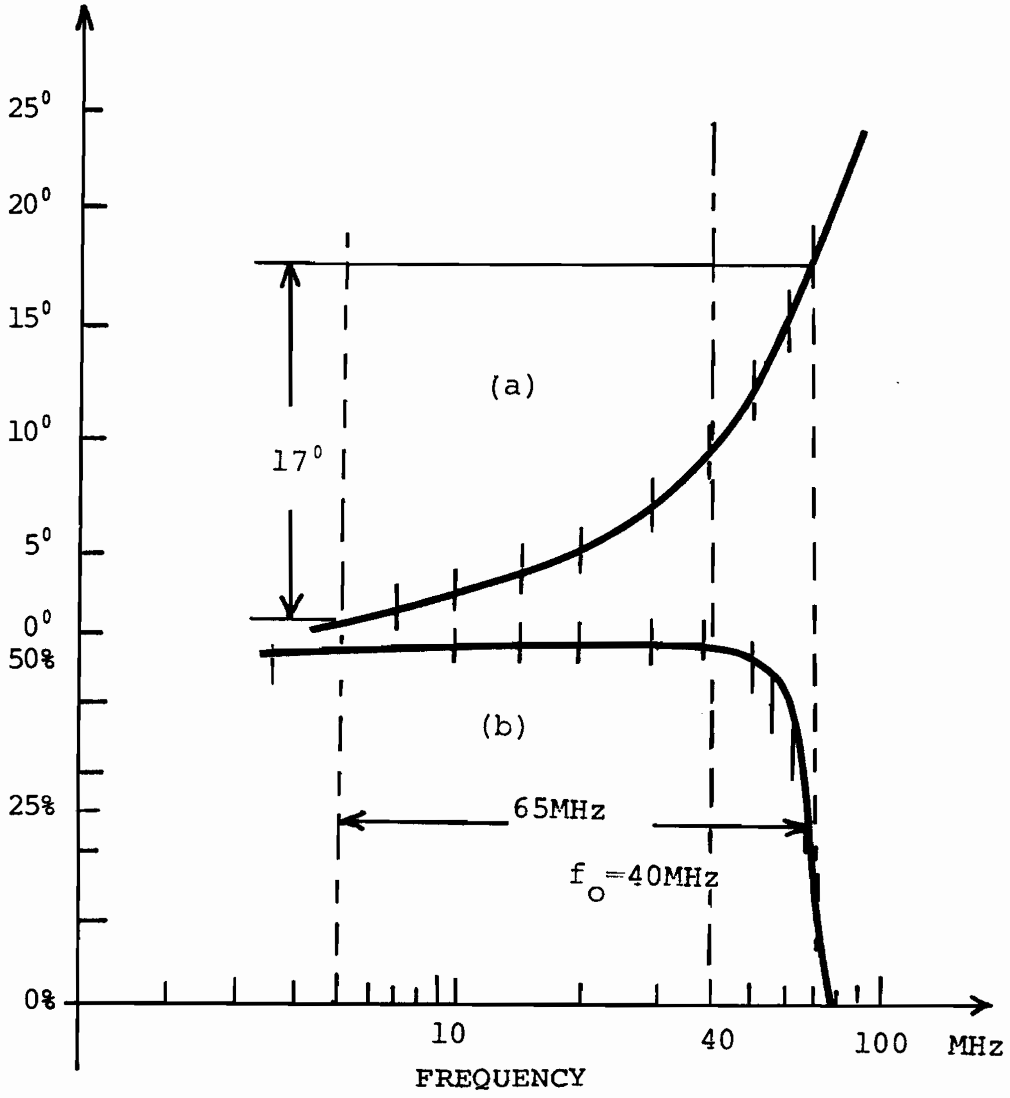

Figure 5-11. Double-phonon, scattering-free, second-order AO Bragg interaction.
a. Calculated and measured deflection angles outside the tellurium versus frequency.
b. Calculated and measured diffraction efficiency versus frequency. The acoustic beam is 1x1mm.
$2\Theta_B = 2.20^0$ inside the crystal, kept constant. (Incident angle).

6.EXPERIMENTAL SYSTEM.

6.1.Introduction.

In order to make the precise AO diffraction efficiency measurements in Chapters 7 and 8, it is important that the power fluctuations of the laser be small. When a laser is stable in frequency, its output power is also stable. In this section we give first the frequency and corresponding power stability characteristics of our CO_2 laser measured for the first time by optoacoustic tracking of a Lamb dip in SF_6 gas [35] (see appendices D and E), and optoacoustic detection in CO_2 gas [34]. Then the optical and acoustic measurement conditions for the diffraction efficiencies and passband measurements of Chapters 7 and 8 are presented.

6.2.The CO_2 Laser and the Optical Measurement Condition.

6.2.1.The CO_2 Laser.

Our CO_2 laser design and its spectral characteristics have been described previously in Ref [34].

We have measured the frequency stability characteristics of our CO_2 laser for the first time using room temperature optoacoustic tracking of an SF_6 Lamb dip. Appendices D and E describe in detail the experimental procedure where a standard electronic negative feedback loop was implemented. The CO_2 laser frequency was compared with the given Lamb dip frequency, so that a relative shift provides an error signal which in turn produces a laser mirror translation tending to minimize shift and eventually lock the two frequencies.

A plot of the laser frequency shift with and without locking scheme in operation, is shown in Fig 6-1, indicating a frequency lock range of 200 KHz and a frequency drift of 800 KHz per 10 minutes time interval, due to $0.02^{0}C$ temperature variation. This results in a frequency stability of 1 part in 10^8. This latter characteristic can be improved provided the ambient temperature variations are controlled to a finer fluctuation limit as would be the case in a specially equipped laboratory environment. Therefore, this laser design will provide also good power stability per 10minutes time interval, since the corresponding frequency shift of the single longitudinal mode oscillating in the laser cavity is much less than the 60MHz one-half power bandwidth of the CO_2 laser.

This conclusion has been verified experimentally;the plot of Fig 6-2 indicates that the laser power fluctuations due to dilation and contraction of the laser cavity with the change of temperature is 0.1 watt per 15 minutes interval. The corresponding frequency shift is estimated at 1KHz . In this experiment, the laser power was measured by a properly calibrated room-temperature optoacoustic detector filled with CO_2 gas [34]. The slope of the plot indicates also that the fluctuations of the laser power due to the gas flow are much smaller that the change of power due to the variations of the length of the cavity.

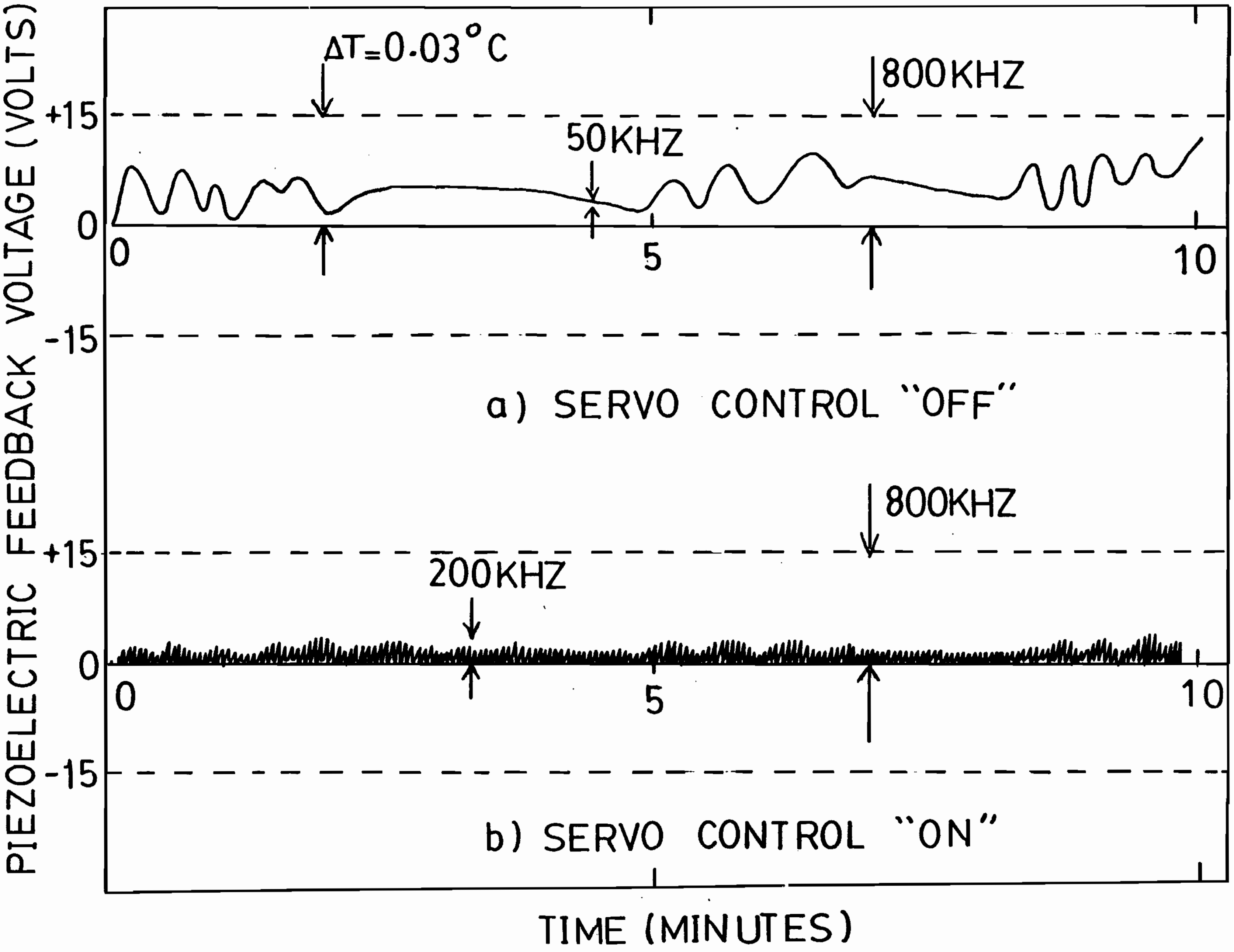

Figure 6-1. Plots of the Frequency Stability of the CO_2 Laser with Time.

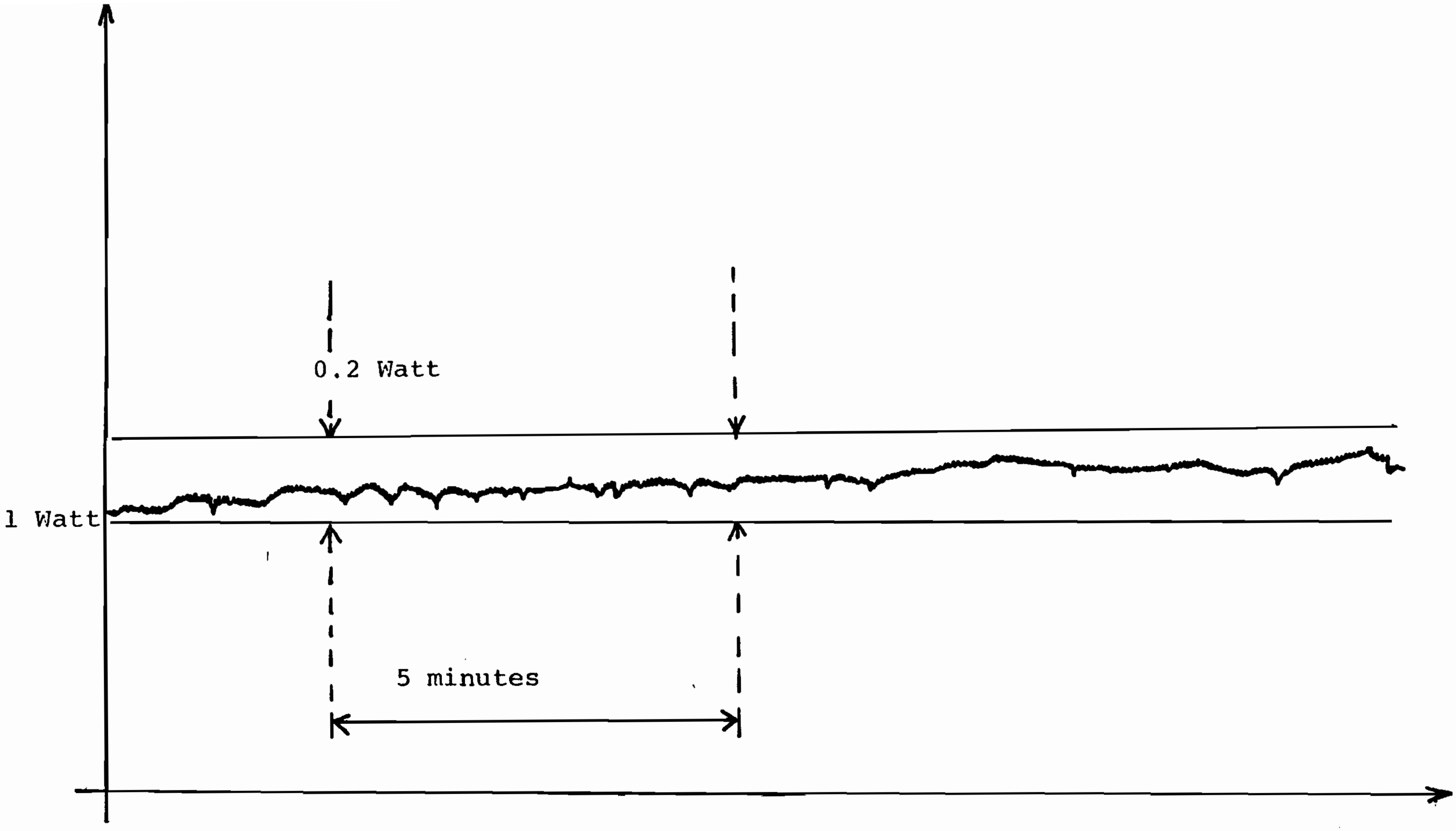

Figure 6-2. CO_2 Laser Power Fluctuations with Time.

6.2.2.Optical Conditions.

The laser light was polarized in the vertical direction by the end reflector grating of the laser. It was focused on the tellurium crystal by a germanium lens of 10cm focal length, in order that the size of the optic beam was at most of the width of the acoustic column.

The light deflected by the acoustic pulses, was detected by an Optikon HgCdTe detector of responsivity 97 Volts/Watt , and cooled at 77^0K, in order to lower the Johnson noise [36]. The average optical power deflected by the crystal was kept well below the maximum optic power which saturates the detector of 850mV [36] by setting the acoustic pulse width and repetition time ratio at a value of the order of 1/1000.

The diffraction efficiency expressed by Eq (3-21) , is calculated by measuring independently the diffracted light intensity (W/m^2) emerging at the diffracted Bragg angle Θ_D and the non deflected optic beam intensity emerging from the crystal.

The incident and diffracted optic angles were measured on the optic table with angular positioners .

6.3.The Acoustic Measurement and Calculation Conditions.

6.3.1.Generalities.

A schematic diagram of the electric and acoustic arrangement is shown in Fig 6-3 . The tellurium cube sample of 8x8x8mm size is cut from a Czochralski grown ingot along the X, Y and Z

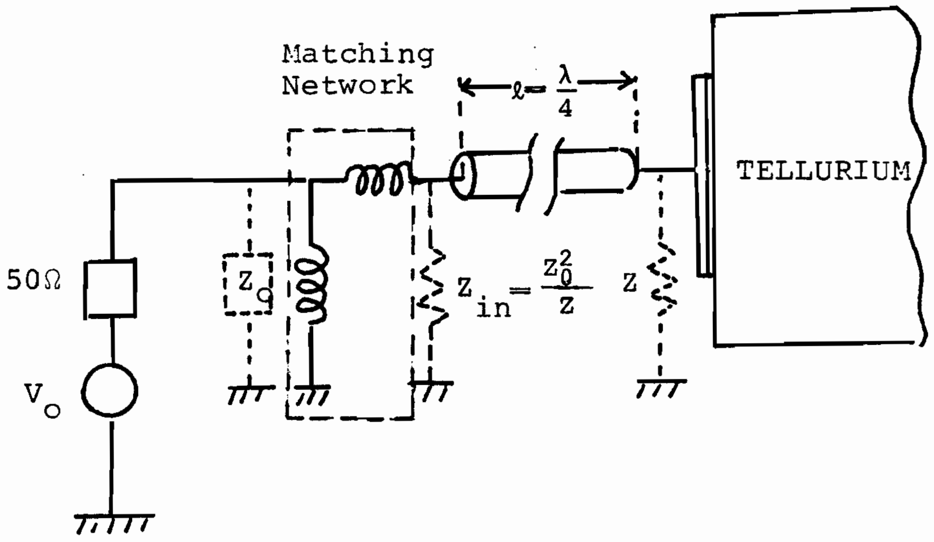

Figure 6-3. a. Acoustic-electrical, experimental arrangement.

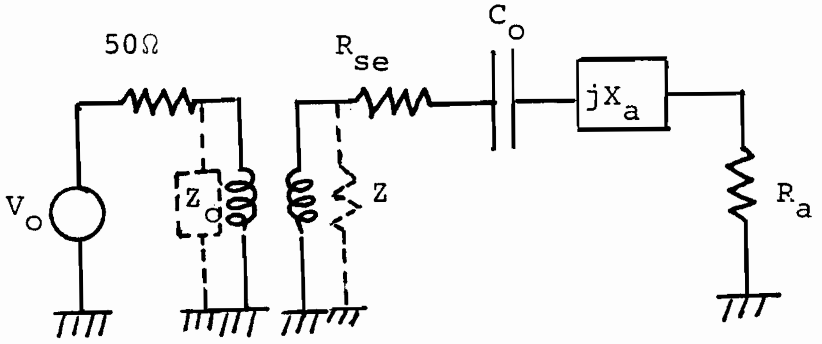

b. Equivalent electric circuit.

crystal axes. A $LiNbO_3$ transducer plate bonded to the tellurium with Canada balsam resin was used to generate the acoustic waves in tellurium. A proper transducer thickness and cut are chosen in order to excite at its resonance frequency, $V_d/2d$, (where d is the thickness and V_d the acoustic velocity in the transducer), the single longitudinal or shear acoustic wave .

In order to calculate the acoustic power in the crystal, a single acoustic excitation mode in the tellurium is required. Thus the polarization direction of the transducer is aligned with the polarization direction of the single acoustic mode in the tellurium.

Also, under electric matched conditions, the acoustic power carried by the single acoustic mode inside the tellurium is equal to the electric power from the RF generator at the resonance frequency of the transducer if there are no losses in the transducer or in the matching network.

6.3.2.Transducer-Substrate Characteristics.

It is important that the transducer-substrate combination provides transfer of acoustic power into the tellurium substrate with high efficiency and well defined acoustic propagation characteristics.

The characteristics of the transducer-substrate combination are:

a) The electromechanical coupling coefficient k of the transducer:

For the two kinds of shear and compressional $LiNbO_3$ transducers used in the experiments of Chapters 7 and 8, the calculated values of k are:

For the 41° X-cut $LiNbO_3$ transducer, k=0.68.

For the 36° Y-cut $LiNbO_3$ transducer, k=0.5.

b) The radiation resistance of the transducer-substrate combination at resonance frequency [23] [26]:

$$R_A = \left(\frac{k^2 \rho_t V_t^2}{\pi^2 \rho V_p \varepsilon \varepsilon_o L H}\right)(1/f_o^2) \qquad (6\text{-}1)$$

where k is the electro-mechanical coupling coefficient

$\rho_t = 4700 Kg/m^3$ is the density of $LiNbO_3$

$V_t = 4793 m/s$ is the fast shear velocity in $LiNbO_3$

$\varepsilon_o = 9\times10^{-12} F/m$ is the free space permittivity

$\varepsilon = 4.84$ is the dielectric constant of $LiNbO_3$

$\rho = 6210 Kg/m^3$ is the density of tellurium.

V_p is the acoustic phase velocity in tellurium.

f_o is the resonance frequency of the transducer.

L,H are the length and width of the cross section of the acoustic column.

For example, for the 41° X-cut $LiNbO_3$ shear transducer at a resonance frequency of 40MHz, $R_A = 950\ \Omega$ and 2370Ω for the fast and slow acoustic shear wave respectively. In this latter calculation, we have used the value of $V_t = 4793 m/s$ as the fast shear acoustic velocity propagating along the X-axis of the $LiNbO_3$ transducer, and $V_p = 2445 m/s$ and 979m/s as the fast and slow shear acoustic velocity in tellurium along X and LxH=5x1mm.

For the compressional 36^0 Y-cut $LiNbO_3$ transducer, $R_A=1293\Omega$ at 40MHz. In this latter calculation, we have used the value of $V_t=7400m/s$ as the compressional acoustic velocity in $LiNbO_3$ and $V_P=2318m/s$ as the acoustic velocity of the longitudinal acoustic wave along X in tellurium.

c) Insertion loss and 3dB acoustic bandwidth of the transducer-substrate combination versus acoustic frequency:

According to Reeder and Winslow [41], if a transducer is connected directly to a source V_o with real impedance Z_o conversion of electromagnetic to acoustic power is given by the power insertion loss ratio:

$$T(f) = \frac{P_A}{P_L} = \frac{V_o^2 /8Z_o}{1/2(I^2R_A)} \qquad (6-2)$$

Where P_A is the power available from the source under matched conditions and P_L is the power absorbed by the real part of the impedance of the transducer, $Z=R_A+jX_A+1/j\omega C_o= R_A+jX$. Where X_A is the reactance and C_o the capacity of the transducer[41].

T(f) can also be written as:

$$T(f) = \frac{(Z_o+R_A)^2+ X^2}{4Z_oR_A} = M_a(f)xM_e(f) \qquad (6-3)$$

Where $M_a(f)$ is the acoustic bandshape function and $M_e(f)$ is the electric bandshape function.[26],[41].

With adequate electric matching, (see Fig 6-3a), the electric bandwidth can be made larger than the acoustic bandwidth. Minimun tuned loss occurs ,(ie $T(f)=1$), when $X=0$ and $R_A=Z_o$. The acoustic bandshape functions are calculated in Ref [41] as a function of the acoustic frequency and the parameter $r_d=\rho V_p/\rho_t V_t$ from which the optimum half-power acoustic bandwidth of the transducer-substrate combination can be predicted.

For example, for the 41° X-cut $LiNbO_3$ transducer bonded on the tellurium crystal: $r_D= 0.674$ (fast shear along X). Thus, from Fig 8-22 of Ref [26],the power insertion loss of the transducer, at resonance frequency is equal to unity and the corresponding 3dB bandwidth of the transducer-substrate is $0.2f_o$.

For the 36° Y-cut $LiNbO_3$ transducer bonded on the tellurium crystal, $r_D= 0.4$. Thus, the power insertion loss at resonance is equal to unity and the corresponding 3db bandwidth of the transducer-substrate is again $0.2f_o$.

We also note that when the frequency is high, the 3dB acoustic bandwidth obtained by Bragg angle limitation becomes less than the 3dB acoustic bandwidth of the transducer-substrate combination (See Chapter 3). In this case one single-element transducer is sufficient to operate a deflector or modulator device.

6.3.3.Consideration of Acoustic and Optic Beam Attenuation.

6.3.3.1.Acoustic Beam.

It is understood that for deflection applications, w_o is usually set to a relatively large value of typically 1cm in order to make N high, where again N is the number of resolvable points.

Along this typically 1cm propagation path, (see Fig 3-1a), the acoustic beam must not be attenuated by more than about 1/e, ie 4.2db/cm.

Therefore we choose to limit the M values calculated in Chapter 9 for deflection applications, to those for which the corresponding AO geometry has an acoustic attenuation at the center acoustic frequency f_o of less than 4.2dB/cm.

The attenuation values can be estimated for an arbitrary AO interaction, from the following approximate expression of the attenuation coefficient [31,32,33]:

$$A = \frac{\omega^2 \gamma \kappa T}{\rho V_P^5} + \frac{\omega}{V_P} \cdot \frac{e^2}{2c\varepsilon} \cdot \frac{\omega}{\omega_c} \qquad (6\text{-}4)$$

Where ω is the acoustic angular frequency.

$\rho = 6210 \text{kg/m}^3$ is the density of tellurium.

γ is the Gruneisen's constant and varies between 0.5 and 7 [31]

V_P is the acoustic phase velocity. T is the temperature $^\circ K$

κ is the thermal conductivity=0.05 $\text{Wdeg}^{-1}\text{cm}^{-1}$. (deg.= $^\circ K$)

$\omega_c = 2\pi f_c$, f_c is the conduction frequency=$5\text{x}10^{10}$ rad/sec [2].

e is the piezoelectric constant (see Appendix B)<0.42 C/m .

c is the stiffness constant (see Appendix B)$<3.27\text{X}10^{10}$ N/m^2.

ε is the dielectric permittivity (see Appendix B)$< 40\text{x}10^{-11}\text{F/m}^2$.

Thus $\frac{e^2}{2c\varepsilon}$ is at most of the order of a one percent and the second term in Equation (6-4) amounts for a small fraction of the first term.

The first term is inversely proportional to V_P^5 and is eight fold larger in tellurium compared to germanium.

When $f < 100$MHz, all M values are suitable for deflection as well as modulation applications.

Above 100MHz, the acoustic attenuation becomes too high, in tellurium, modulation applications are more favorable since in this case the acoustic path crossing the laser beam waist is relatively small [20], and therefore the acoustic attenuation can be neglected.

6.3.3.2.Optic Beam.

In tellurium, the optic absorption coefficient is maximun and equals 5cm^{-1} [13] for polarization direction parallel to the Z axis. However, since the acoustic beam waist in the direction of the optical propagation is small, typically less than 1mm, the total optic absorption can be neglected for the given short propagation distances.

Finally, we note that in modulation devices, where the acoustic and optic beams are highly localized along the relatively small acoustic path length, the acoustic as well as the optical attenuation can be neglected. In this case, fastest rise time or largest bandwidth of the AM modulated light is obtained [11].

6.3.4.Measurement of the acoustic power inside the crystal.

Sittig [71] has shown that the acoustic power flowing inside the crystal can be calculated from Eq(6-2). Where P_A represents the best maximum power available from the source of output impedance $Z_o=50\Omega$ and L_D represents the total input power loss in the matching circuit, conversion into undesired modes, radiation from the back face of the transducer, absorption in the bond layer, etc... Hence, when L_D is known, the acoustic power inside the crystal is equal to, $P_L=L_DP_A$. ($L_D<1$).

L_D was calculated from the following equation [26] [56] [71]. (See Fig 6-4).

$$\frac{P_L}{P_A} = L_D^2 L_B (1-R_L^2) = \frac{\text{Power in the first acoustic echo}}{\text{Input power across } 50\Omega} \qquad (6\text{-}5)$$

R_L^2 is the coefficient of reflexion in intensity of the acoustic wave at the interface Tellurium-$LiNbO_3$.

R_L^2 was calculated from the following equation [26]:

$$R_L = \frac{\rho V_p - \rho_t V_t}{\rho V_p + \rho_t V_t} \qquad (6\text{-}6)$$

where ρ, ρ_t, V_p, V_t, are the acoustic densities and phase velocities of the tellurium and $LiNbO_3$ crystals, respectively.

L_B is the acoustic power loss after a round trip inside the crystal. $L_B=\exp(-4A\ell)$. Where ℓ is the length of the crystal and A the acoustic attenuation coefficient expressed by Eq(6-4).

L_B was calculated from the following equation:

$$\frac{\text{Power into second acoustic echo}}{\text{Power into first acoustic echo}} = \frac{L_B^2 R_L^2 (1-R_L^2)}{L_B(1-R_L^2)} = L_B R_L^2 \qquad (6\text{-}7)$$

The power levels in Eq(6-5,6,7) were measured from Fig 6-4b .

For the 41° X-cut $LiNbO_3$ transducer L_D was found to vary between 0.05 and 1 from 20MHz to 90MHz.

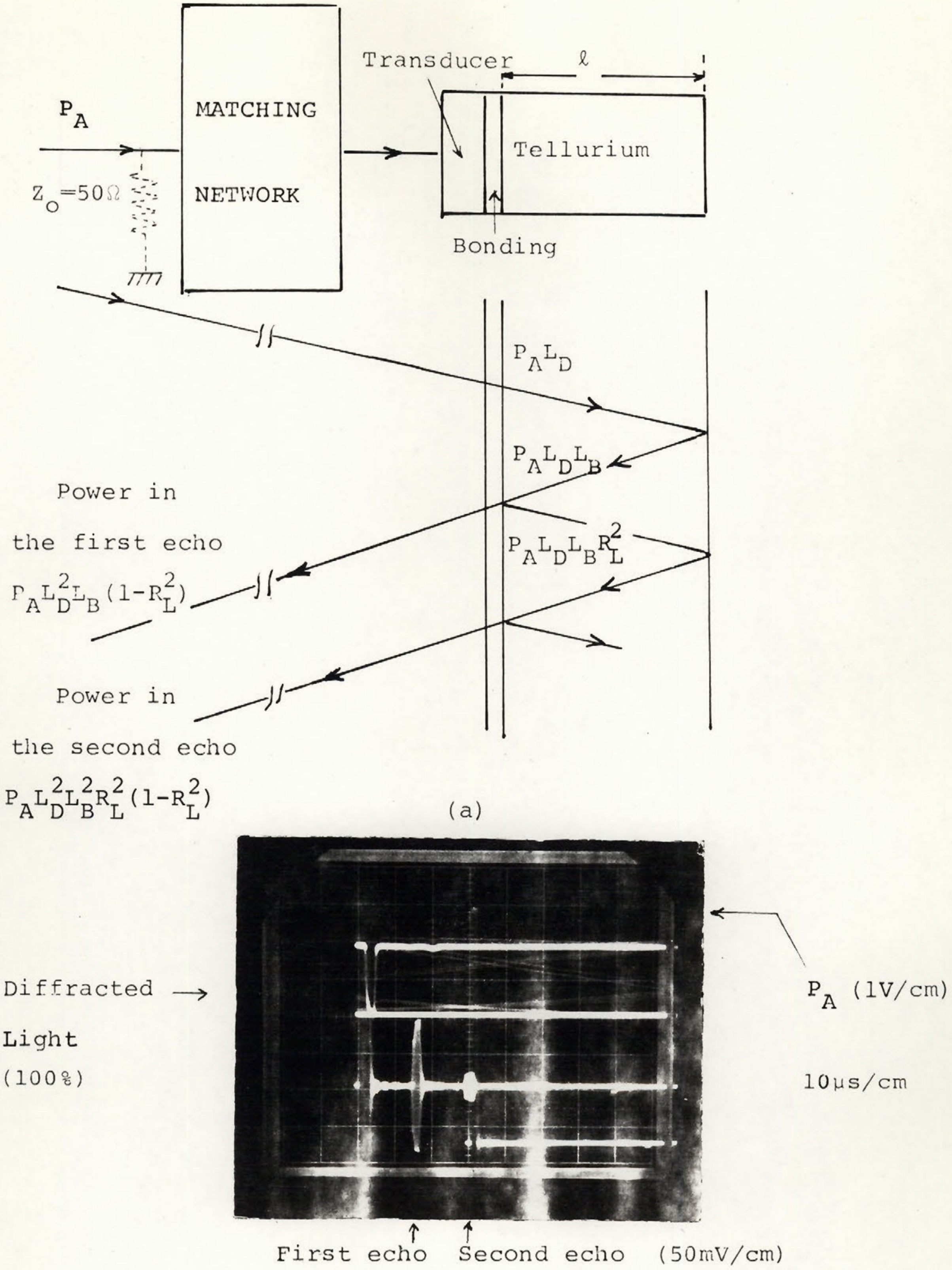

(a)

(b)

Figure 6-4. Measurement of the acoustic power inside the crystal. a) Theory. b) Typical oscillogram.

7.MEASUREMENT OF THE UNKNOWN PHOTOELASTIC COEFFICIENTS p_{65} p_{56} p_{44}

In order to evaluate these photoelastic coefficients, the figure of merit as given by Eq (3-22) is measured for a number of different conveniently chosen configurations,as specified in Chapter 4, where the required p_{ij} parameters become significant in the expression of p_{eff}.

7.1.Measurement of p_{65}.

For the calculation of p_{65}, we use the AO interaction of Fig 4-a where the fast shear wave propagates along the X axis, the extraordinary incident and ordinary diffracted beams propagate in the XZ plane near the Z axis.

At a center frequency of f_O=40MHz, Θ_I=7.5° and Θ_D=6° inside the crystal. A diffraction efficiency of η=5% for an acoustic power striking the laser beam of 1 Watt was measured. Using Eq (3-21), we find:

$$M=230\text{x}10^{-15}\,\text{sec}^3/\text{Kg} \text{ and } p_{eff} = 0.041$$

Hence, using Eq (4-3):

$$p_{65} = \pm 0.04$$

To eliminate the sign uncertainty, we use an AO interaction where the extraordinary incident beam propagates now at 20° from the Z axis in the XZ plane, the diffracted beam is ordinary polarized and the slow shear wave propagates along X.From Eq (4-3) we find two possible values [37]:

$$\text{(a)} \quad p_{65} = -0.04 \text{ and (b) } p_{65} = -0.013$$

Comparing (a) and (b) here with the previous values, clearly p_{65} is determined to be:

$$p_{65} = -0.04$$

The total uncertainty on this coefficient is estimated to be at most 20% and is mainly due to slight beam misalignment and limitation of accuracy in estimation the acoustic power.

7.2.Measurement of p_{56}.

For the estimation of p_{56}, we use the pure transverse shear wave along Y, velocity of 1439m/s, interacting with a Z-propagating extraordinary polarized incident optical beam in the YZ plane, 5° offset from the Z axis inside the crystal, and an acoustic frequency of 100MHz. Figure 4-b, shows the corresponding AO geometry. Having measured a diffraction efficiency of 6% with a total acoustic power striking the laser beam of 3.4 Watts, Eq (3-21) gives:

$$M=70\times10^{-15}\ \mathrm{sec}^{3}/\mathrm{Kg}$$

and using Eq (3-22), $p_{eff} = \pm0.0104$,hence from Eq (4-5b),

$p_{56} = 0.27$ or 0.027

The highest magnitude 0.27 is accepted, since this value agrees with an independent measurement [37] in which the ratio p_{56}/p_{11} was found to be equal to 2.

The uncertainty on this coefficient is estimated at 20% and is due mainly to the small value of Θ_D which makes the possibility of error high for p_{56} despite the good precision in obtaining p_{eff}.

7.3.Measurement of p_{44}.

Finally, we have estimated p_{44} using the configuration, of Fig 4-c, where the acoustic beam propagates 4° from the Y axis in the YZ plane, the incident optical beam is along Z and the diffracted beam is near the Z-axis.Both optic beams are extraordinary polarized.

At 100MHz, we measured a diffraction efficiency of 8% for an acoustic power of 2 Watts, carried by the fast shear wave propagating at a velocity of 2519m/s.

Using Eq (3-21):

$M=2385 \times 10^{-15} sec^3/Kg$, with an H/L ratio of 3.

Using Equations (3-22) and (4-6), we obtain a value of p_{44} of 0.15 or 0.51 with the condition that $p_{13}>0$. The smaller magnitude is accepted, since it is in agreement with another independent experiment [37].

In summary our estimates for the following previously unknown photoelastic constants are:

$p_{65} = -0.04 \pm 0.008$ (MKSA)

$p_{56} = 0.27 \pm 0.05$ (MKSA)

$p_{44} = 0.15 \pm 0.04$ (MKSA)

Furthermore, in the determination of these coefficients we find that p_{11}, p_{12}, p_{13}, must be positive.

Finally from the results obtained in Appendix G, where we consider the case of an extraordinary polarized incident optic beam interacting with an acoustic beam propagating along the rotated X* axis localized at $\phi=0^0$, $\Theta=130^0$ and $\psi=\pm45^0$, we verify the value of these coefficients and furthermore we find that p_{31}

is positive. It is the last significant photoelastic coefficient with unknown sign.

The complete photoelastic tensor is presented in Table 2 .

TABLE 2

PHOTOELASTIC CONSTANTS OF TELLURIUM (MKSA)

0.164	0.138	0.146	-0.04	0	0
0.138	0.164	0.146	0.04	0	0
0.086	0.086	0.038	0	0	0
0.27	-0.27	0	0.15	0	0
0	0	0	0	0.15	0.27
0	0	0	0	-0.04	0.013

8.MEASUREMENT OF THE DIFFRACTION PASSBAND CHARACTERISTICS IN TYPICAL AO INTERACTIONS. COMPARISON WITH THE CALCULATED RESULTS.

8.1.Introduction

In this section using a high stability CO_2 laser we verify experimentally the calculated deflection passband characteristics of Chapter 5 for the three AO configurations studied.

8.2.The X-axis Birefringent AO Interaction

8.2.1.Experimental Arrangement.

The schematic diagram of the experimental arrangement is shown in Fig 8-1b. The tellurium cube sample of 8x8x8mm size is cut from a Czochralski-grown ingot along the X,Y, and Z crystal axis. The shear transducer is a 41° X-cut $LiNbO_3$ plate, bonded to the tellurium with Canada balsam resin. The optic and acoustic experimental conditions have been described previously in Chapter 6. This transducer was used in order to excite in a single-mode operation the fast or slow shear wave in tellurium propagating along X.

The characteristics of the transducer bonded on the tellurium crystal were given previously in Chapter 6.

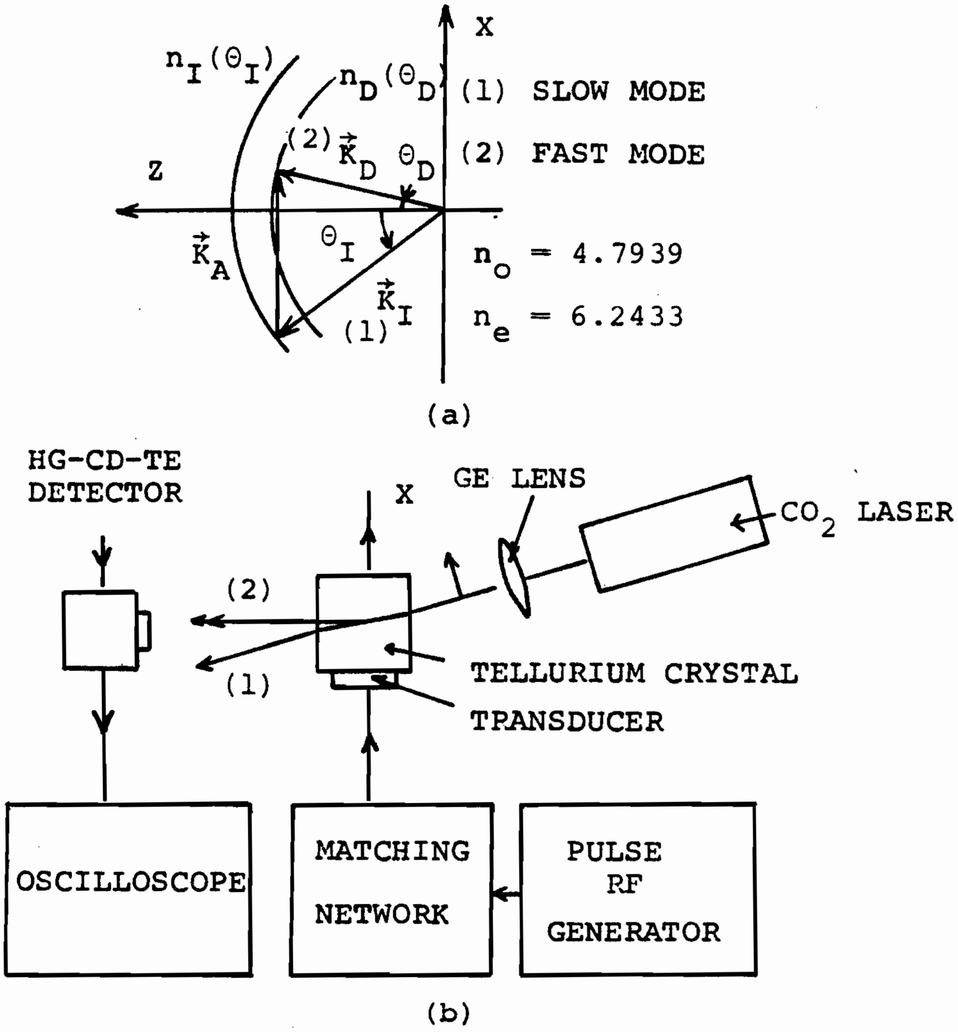

(a)

(b)

Figure 8-1. a. Wavevector diagram for acoustooptic interaction in tellurium.
b. Experimental arrangement

8.2.2. Measurement of the diffraction characteristics. Comparison with the calculated results.

In Figures 5-4,5, the measured angles of incidence and diffraction for the fast and slow shear modes are shown together with the theoretical predictions for a fixed incident angle $\Theta_I = 1.2^0$. The uncertainty bars indicate the half power angle spread in adjusting for the phase matching and the deviation between measured data and calculations is due to an acoustic beam diffraction divergence of about 0.4° at the highest frequency data points. These results indicate that the measured angular diffracted sweep (or slope), is in agreement with the calculated values of Chapter 5.

Using the measured value of p_{65} of Chapter 7 the AO figures of merit M for the fast and slow shear acoustic waves can be calculated using Eq (3-22) with p_{eff} calculated using Eq (3-23).

For the fast shear (V_P=2445m/s), we obtain:

$$p_{eff} = 0.041 \quad \pm 20\%.$$

$$M(fast) = 0.23 \times 10^{-12} sec^3/Kg.$$

For the slow shear mode (V_P=979m/s), we obtain:

$$p_{eff} = 0.006 \quad \pm 50\%$$

$$M(slow) = 0.08 \times 10^{-12} sec^3/Kg$$

The existence of the double phonon scattering dip shown in Figures 5-4,5 as well as the value of M near f_o have been verified experimentally.

8.3.The 4° Off-Axis Interaction.

8.3.1.Experimental Arrangement.

The schematic diagram of the experimental arrangement is shown in Fig 8-2b. A 41° X-cut $LiNbO_3$ transducer was used to excite the acoustic shear waves in the tellurium.

8.3.2.Measurement of the passband characteristics

In Figures 5-8,5-9, the measured diffracted angles outside the crystal, for a fixed incident angle of 2.3^0 for the fast and slow shear modes propagating inside the crystal, are shown with the corresponding calculated predictions. The uncertainty bars indicate the half power angle spread in adjusting for the phase matching and the deviation between measured data and calculations is due to an acoustic beam diffraction divergence of about 0.4°. at the highest-frequency data points. The measured deflection angles are in agreement with the calculated values of Chapter 5.

The figures of merit for the fast and slow acoustic shear waves corresponding to this AO interaction, are calculated using again Eq (3-22) where p_{eff} is calculated Eq (3-23).

For the fast shear wave (V_P=2539m/s), we obtain:

$$p_{eff}= 0.035 \pm 20\%$$

$$M(fast)=0.15x10^{-12} sec^3 /Kg$$

For the slow shear mode (V_P=993m/s) we obtain:

$$p_{eff}=0.006 \pm 50\%$$

$$M(slow)=0.08 x10^{-12} sec^3/Kg$$

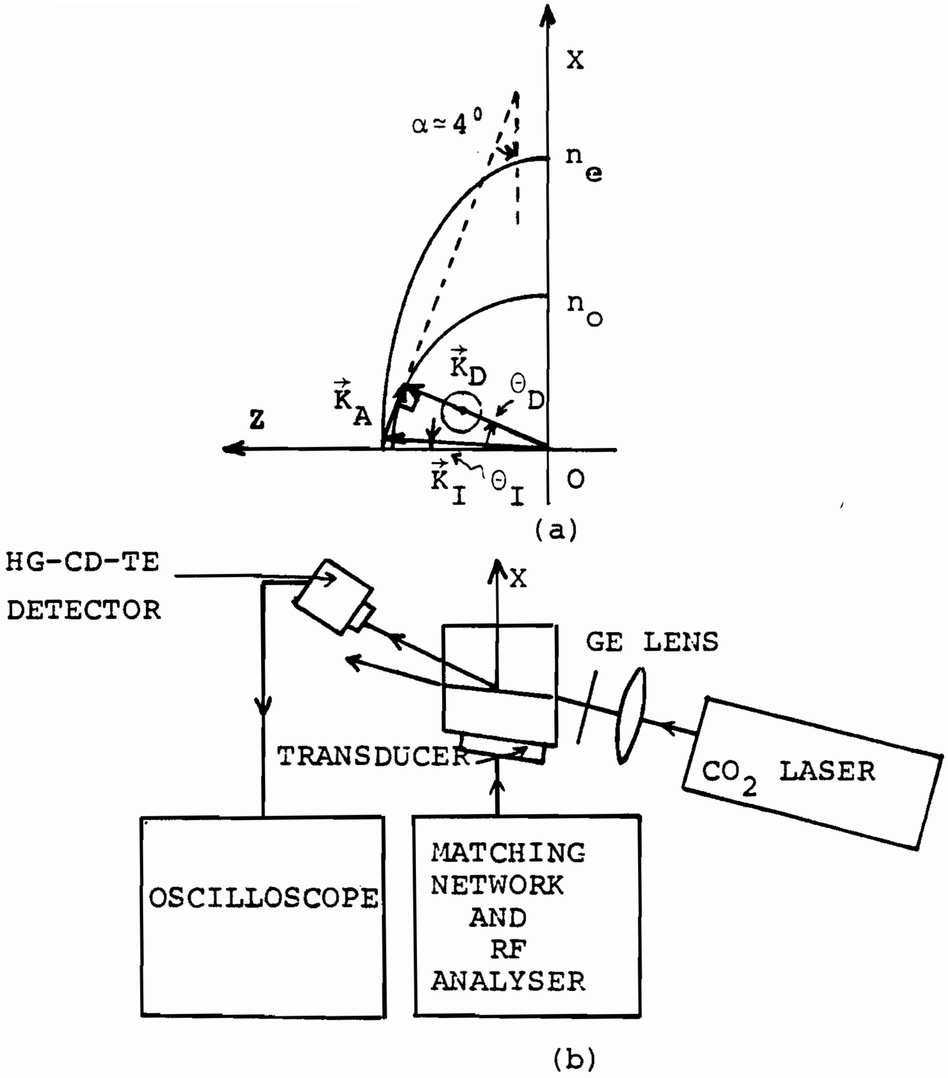

Figure 8-2. a. Wavevector diagram for the 4° off-axis AO interaction.
b. Experimental arrangement.

In calculating the above results, we have used $n_{I,D}$=4.7939 and the measured values of p_{65} given in Chapter 7. These results indicate, that in order to diffract 50% of the incident light at f_o we need 80 Watts for the fast shear wave and 154 Watts for the slow shear wave, for a L/H ratio of 1. These values were not verified experimentally because the transducer could not excite these pure acoustic shear waves of the required power in tellurium.

8.4.The Second-Order X-Axis Isotropic Interaction.

8.4.1.Experimental Arrangement.

A schematic diagram of the experimental arrangement is shown in Fig 8-3b

The compressional transducer is a 36° Y-cut $LiNbO_3$ plate. Its characteristics are given in Chapter 6.

8.4.2.Measurement of the Passband Characteristics.

Figure 5-11 shows good agreement between the data points and the theoretical calculation of the diffraction efficiency and the corresponding diffracted angles. In this configuration, Θ_I was kept constant at 2.2° inside the crystal and the acoustic frequency was varied around 40MHz. The deviation between measured data and calculations at low acoustic frequency is due to acoustic diffraction.

Thus this second-order AO configuration has a deflection

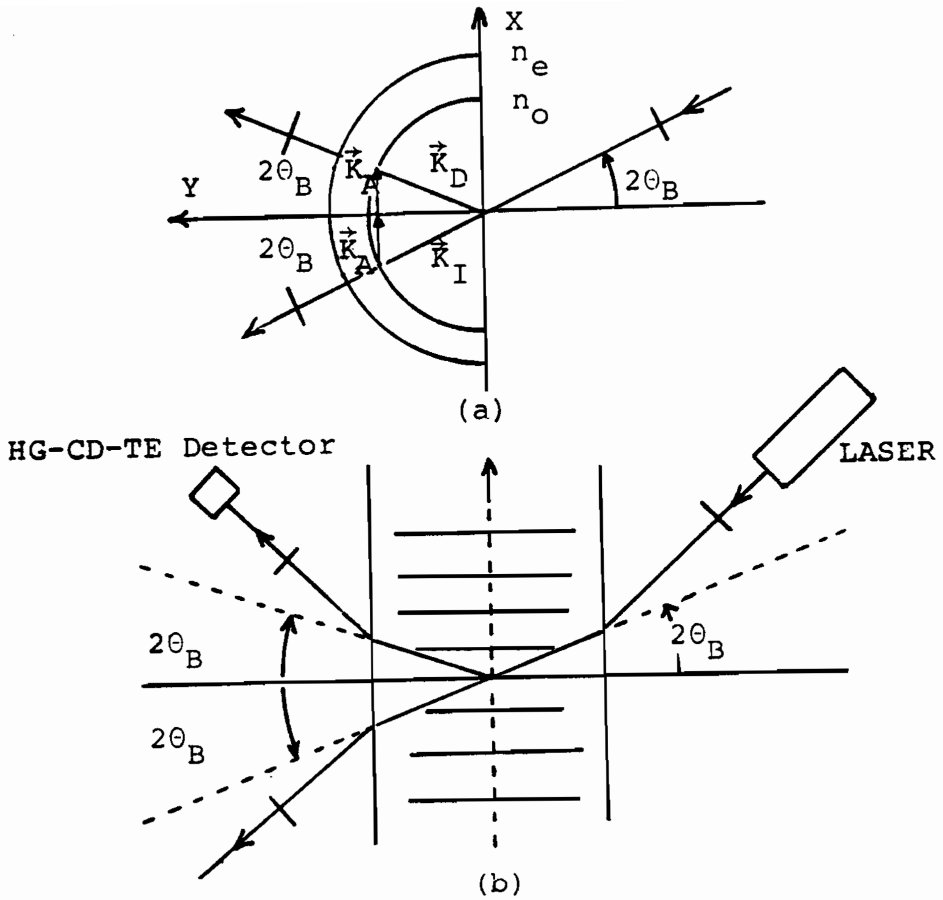

(a)

(b)

Figure 8-3. Double-phonon scattering-free, second-order AO Bragg configuration. $2\Theta_B = 2.2^0$ inside the tellurium, f_o=40MHz.
a. Wavevector diagram.
b. Experimental arrangement.

passband characteristic comparable to the 4° off X-axis geometry but the acoustic power required for the same percentage of diffracted beam power is about 5 times larger than for the case of the fast shear 4° off X-axis interaction [1].

Since $M=4400\times10^{-15}\,\text{sec}^3/\text{Kg}$, is the figure of merit of the normal first-order isotropic, X-axis longitudinal acoustic propagation interaction [1], we calculate from Eq(3-32), that in order to diffract 100% of the incident light, we need 17 watts of acoustic power for an L/H ratio of 1. This result has been verified experimentally with an accuracy estimated at 50%.

The elimination of the double-phonon-scattering dip has also been verified experimentally.

9.THREE DIMENSIONAL QUANTITATIVE MAPPING OF THE FIGURE OF MERIT IN TELLURIUM.

9.1.Introduction

Using the completely determined photoelastic tensor of tellurium Table 2 and Equations (3-22),(3-23), we present in this section the computed figure of merit for acoustooptic diffraction configurations that scan the entire space of the crystal for first and second-order isotropic interactions as well as for first-order birefringent interactions.

The Tables presented in this section list only the highest M values found for these AO interactions with the corresponding relevant AO parameters as presented in Chapter 3.

In Appendix A the computer programs used in these calculations are presented, each of them is followed by a detailed listing of the highest-M values computed for each of the AO configurations specified in the next sections.

9.2.First-Order and Second-Order Isotropic AO Interaction.

A general isotropic AO interaction is defined with the help of Figures 3-1c and 3-3a.

We note in Fig 3-3a, that the acoustic and optic wavevectors form the well known vector triangle which lies in the X*Z* plane, localized by the three Euler angles ϕ,Θ,ψ.

The AO geometry was scanned in the half space of the crystal , in which ϕ and Θ were each varied from 0 ,180^{0} by steps of 10^0 at ψ constant. For each set of ϕ,Θ,ψ, the AO triangle was furthermore rotated around the Z* axis by an angle of 90° in steps of 10°, in order to get all possible isotropic AO geometries similar to that of Fig 3-3a.

This procedure generates 5832 AO interaction configurations. However to each acoustic wavevector $\vec{K}_A$ corresponds three modes described as longitudinal, fast quasi shear, slow quasi shear. Thus in total 3x5832 figures of merit have been calculated.

We have sorted out these values into three groups corresponding to the three acoustic modes. The figures of merit are evaluated numerically from the photoelastic tensor,Table 2 and Eq (3-22) with a computer. The three-dimensional quantitative mapping of Fig 9-1 shows the most efficient AO isotropic interaction geometries of tellurium, where we note that the highest M values are found for acoustic propagation in the XY plane (ie $\psi=0$).

Table 3 lists , together with the M-values the characteristics of the AO interaction such as the direction of the acoustic beams, p_{eff}, V_P, the direction cosines of the acoustic polarization vector in the rotated axes X*,Y*, Z*, the deflection passband characteristics, the global figure of merit M, and the acoustic attenuation. It should be noted that in Table 3 , the values of M for second-order isotropic interactions are given as being equal to those of first-order isotropic interaction and the deflection slope is twice as large, following the discussion of section 3.4.3.

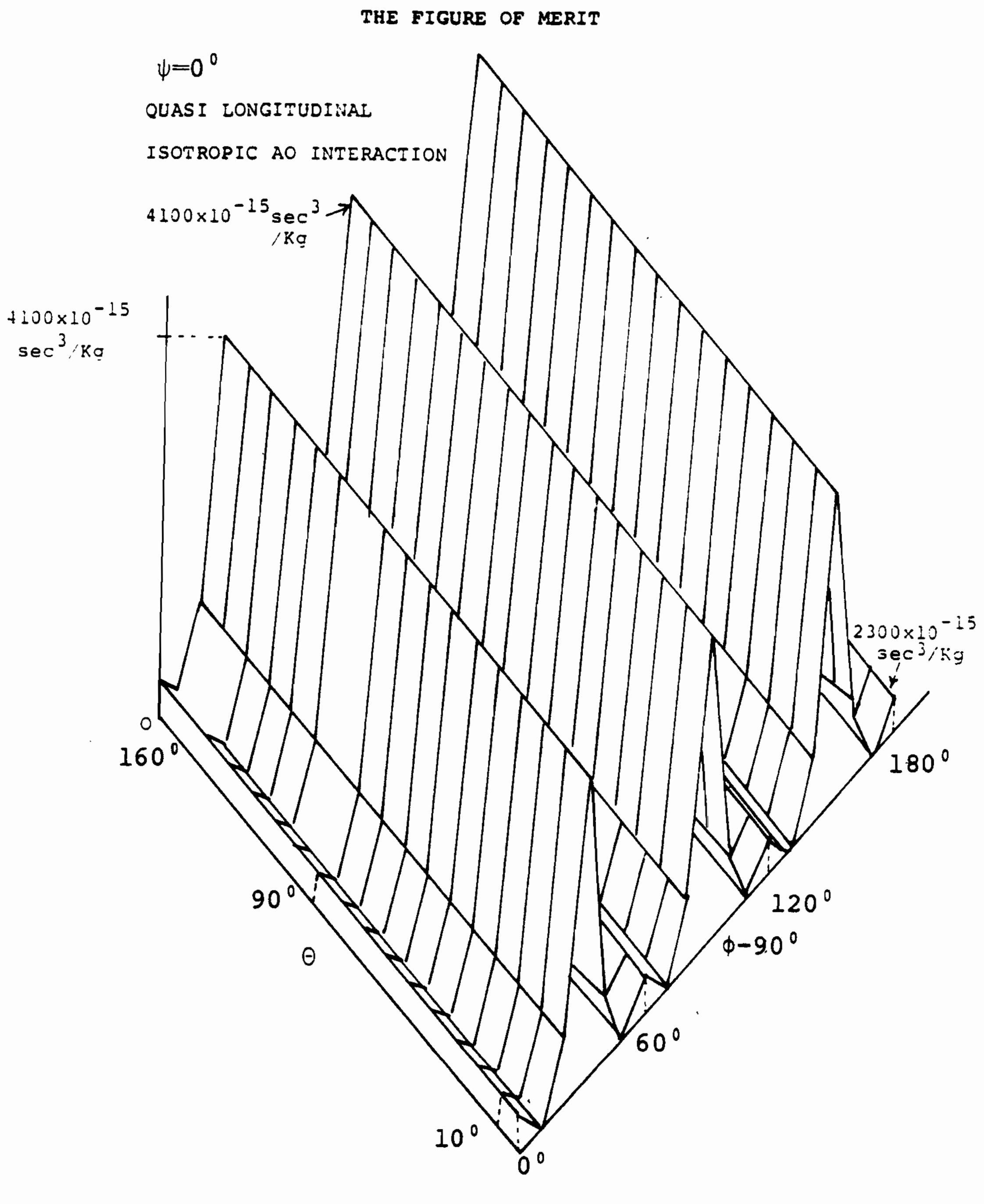

Figure 9-1. Three Dimensional Quantitative Mapping of the High M-Figures of Merit for Isotropic Interactions with Ordinary Polarized Optic Beams.

TABLE 3

HIGHEST M VALUES FOR ISOTROPIC AO INTERACTIONS, ASSOCIATED WITH PURE ACOUSTIC MODE ON THE ROTATED AXES WITH THE CORRESPONDING VALUES OF THE AO PARAMETERS AND GLOBAL FIGURE OF MERIT

FIRST AND SECOND ORDER ISOTROPIC INTERACTIONS	PURE LONGITUDINAL (1st Order)	(2nd Order)
Optic Polarization	Ordinary($\perp$OZ Axis)	
$Mx10^{-15}sec^3/Kg$	4100	4100
P_{eff}	0.16	same
V_P(m/s)	2310	same
Acoustic Polarization Direc.Cosines (Rotated Axes)	1.0 0.0 0.0	same
Acoustic Direction (ϕ,Θ,ψ)	ϕ=0 Θ=arbitrary ψ=0	same
Angle$(\vec{V}_P,\vec{V}_G)$	0	same
f_o(MHz)	40	same
$\Delta f/2$(Mhz)	58	29
$\Delta\Theta/2$(Deg)	7.2^0	7.2^0
$P={}^{\Delta\Theta}/\Delta f$ per 10MHz	1.2^0	2.4^0
Global figure of merit $x10^{-7}$(sec/Kg)m^2	1000	1000
Number of Resolvable Points (D=1cm)	125	125

9.3.First-Order Birefringent Interactions.

9.3.1.Case 1, Incident and Diffracted Optic Beams Extraordinary Polarized.

We calculate the figure of merit for the AO configuration corresponding to Fig 3-1c but now the directions of polarization of the optic beams are extraordinary, as defined in Fig 3-1c. This AO triangle was scanned in the entire half spherical space of the crystal. (ie,$\phi=0°$ to 180° $\Theta=0°$ to 180°, with $\psi=0°$, =±15°, ±45°, ±75°, ±90°). This procedure generates 3x2448 cases. It should be noted that the configurations for which $\Theta=0°$ or 180°, correspond to isotropic interactions and were considered previously in section 9-2.

The three dimensional quantitative mapping of Fig 9-2 shows the location of the most efficient birefringent interactions which are noted to be up to two orders of magnitude higher than in the isotropic case.

Table 4 lists the highest M values and gives, as in section 9-2 , the corresponding relevant AO parameters.

It is to be noted also that these birefringent interactions are described by wavevector triangles similar to the isotropic case and consequently the expressions for the passband characteristics follow the isotropic expressions.

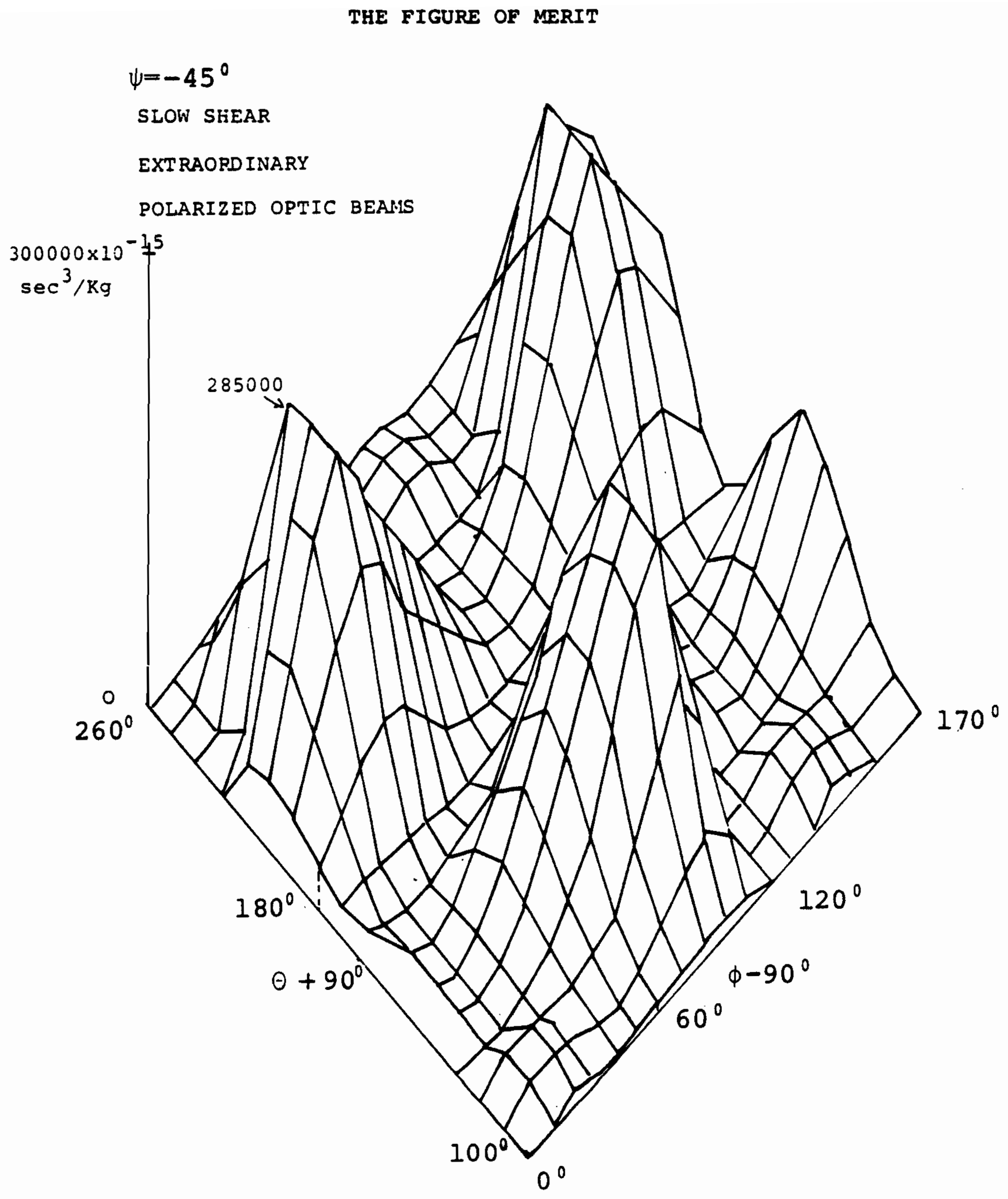

Figure 9-2. Three Dimensional Quantitative Mapping of the High M-Figures of Merit for Birefringent Interactions with Extraordinary Polarized Optic Beams.

TABLE 4

HIGHEST M VALUES FOR BIREFRINGENT AO INTERACTIONS ASSOCIATED WITH PURE ACOUSTIC MODE ON THE ROTATED AXES AND CORRESPONDING AO PARAMETERS AND GLOBAL FIGURE OF MERIT

Optical Incident Polarization	Inc. Optic Beam Extr. Dif. Optic Beam Ord.			Inc. Optic Beam Extr. Dif. Optic Beam Extr.		
	(1st Order)			(1st Order)		(2nd Or)
M $\times10^{-15}$ sec^3/Kg	231	31600	500000	100000	300000	300000
P_{eff}	0.04	0.11	0.33	0.26	0.3	same
V_P (m/s)	2445	979	979	1439	1023	same
Acoustic Polarization Direc.Cosines (Rotated Axes)	0.0 -0.44 0.89	0.0 0.89 0.44	0.0 0.89 0.44	1.0 0.0 0.0	0.058 -0.89 0.43	same same same
Acoustic Direction (ϕ ,Θ ,ψ)	$\phi=0^\circ$ $\Theta=0^\circ$ $\psi=0^\circ$	$\phi=180^\circ$ $\Theta=20^\circ$ $\psi=0^\circ$	$\phi=180^\circ$ $\Theta=90^\circ$ $\psi=0^\circ$	$\phi=90^\circ$ $\Theta=50^\circ$ $\psi=0^\circ$	$\phi=120^\circ$ $\Theta=140^\circ$ $\psi=\pm45^\circ$	same same same
Acoustic Poynting Vector Direc.Cosines (Rotated Axes)	1.0 0.0 0.0	1.0 0.0 0.0	1.0 0.0 0.0	0.71 -0.53 -0.45	0.91 -0.39 -0.049	same same same
Angle($\vec{V}_P,\vec{V}_G$)	0	0	0	32.5	23	same
f_o (MHz)	40	100	369	40	40	same
$\Delta f/2$(MHz)	50	19	20	32	22.5	11.25
$\Delta\Theta/2$(Deg)	6	6	6	6.3	6.3	6.3
$P=\Delta\Theta/\Delta f$ per 10MHz	1.2°	3.0°	3.0°	1.9°	2.8°	5.6°
Global Figure of Merit $\times10^{-7}(sec/Kg)m^2$	64	2001	22100	11500	17000	17000
Number of Resolvable Points (D=1cm)	100	100	100	100	100	100

9.3.2.Case 2,Incident Optic Beam Extraordinary Polarized, Diffracted Optic Beam Ordinary Polarized.

We calculate the figure of merit for the AO configuration shown in Fig 3-1c, and specified in Section 3.2.1 . This interaction triangle will scan the space in two distinct regions, first in the region characterized by optical activity (ie $\Theta < 5^\circ$), and then in the region of optic absorption (ie $\Theta > 5^\circ$).

A)Scanning in the region where tellurium is optically active . (ie $\Theta < 5^\circ$)

In this region the expression of the figure of merit is still given by Eq(3-22) . First we consider a vertical AO triangle localized by $\phi=0^0$,$\Theta=0^0$, with ψ arbitrary. This right angled AO triangle, is scanned around the Z axis, (ie ϕ is varied between 0° to 180° by 10° steps and $\Theta=0^0$,$\psi=0^0$), generating 3x18 configurations and corresponding figures of merit. Then the scan is extended to the entire cone with the computed M values found to be slightly decreasing in magnitude.

Table 4 lists the highest M value configuration.

B) Scanning in the region where $\Theta > 5^0$.

In the region where $\Theta > 5^\circ$, the AO triangle of Fig3-1c has been scanned in such a way that Θ varies between 10° and 170° and ϕ varies between 0° to 180° by 10° steps at ψ constant. For each set of ϕ Θ ψ , the AO triangle was furthermore rotated by $\psi = \pm 15^\circ, \pm 30^\circ, \pm 75^\circ$. This procedure generates 3x2142 configurations. The three-dimensional quantitative mapping given in Fig 9-3, shows the most efficient birefringent AO interactions of tellurium. Note that these highest M values are found for an acoustic propagation in the XY plane (ie $\psi=0°$) and are also of the same order of magnitude as for the previously discussed birefringent interactions with both optic beams extraordinary polarized.

Table 4 lists the highest M values with the corresponding relevant AO characteristics.

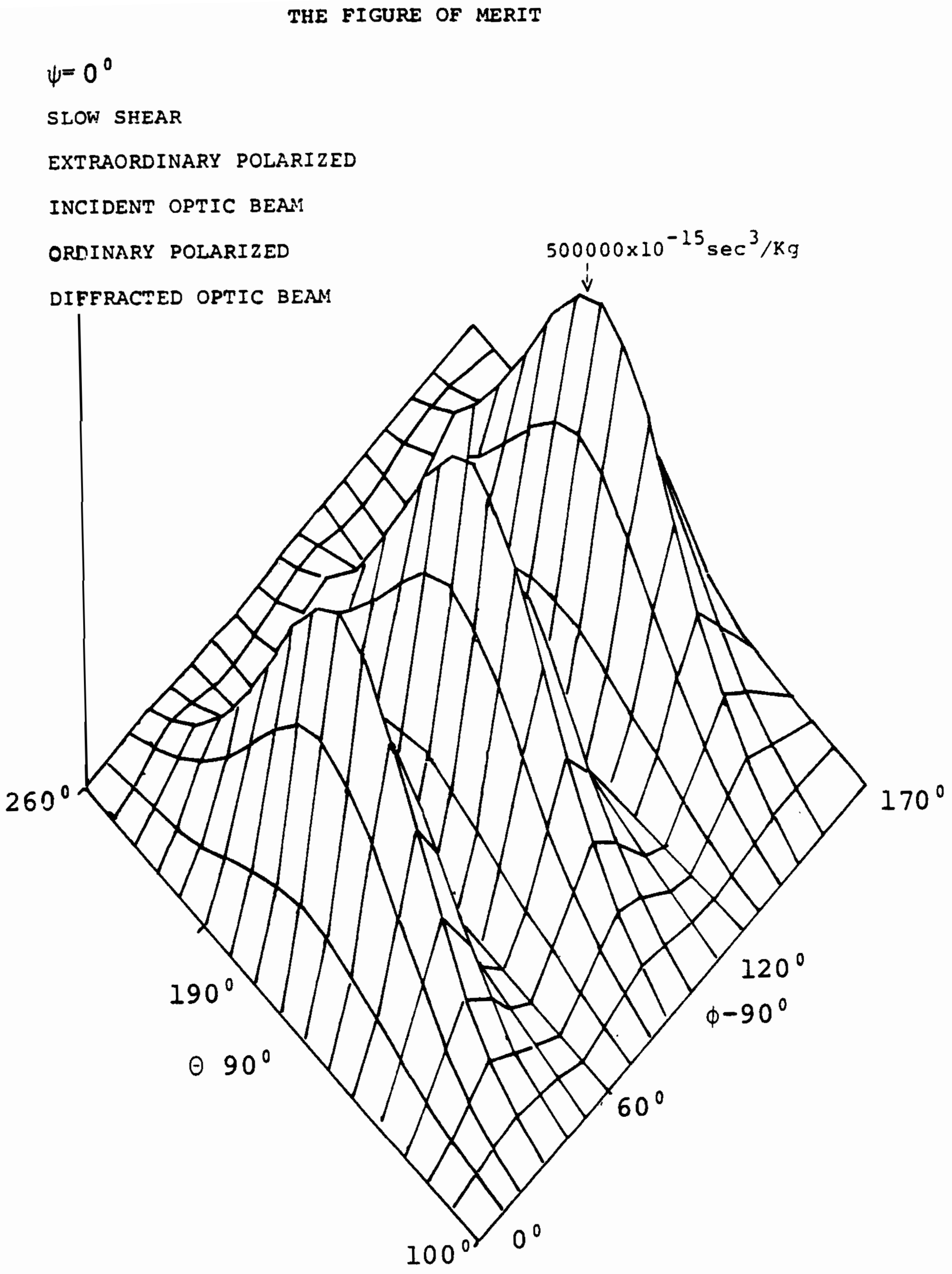

Figure 9-3. Three Dimensional Quantitative Mapping of the High M-Figures of Merit for Birefringent Interactions with Incident Optic Beam Extraordinary Polarized and Diffracted Beam Ordinary Polarized.

10.DISCUSSION AND SUMMARY.

10-1.Discussion.

10.1.1.Isotropic AO Interactions.

The highest value found for the figure of merit associated with a pure acoustic mode on the rotated X*,Y*,Z* axes, is equal to $4100 \times 10^{-15} \sec^3/\mathrm{Kg}$, and is identical to the value reported previously by Fukuda [1]. Our computation shows that this high M value is also found for the configurations specified by $\phi=0°,60°,120°$ $10°<\Theta<170°$, $\psi=0°$. (See Fig 9-1).Note that in all these cases the acoustic beam propagates in the XY plane. It should be noted that the peak values are obtained when p_{eff} and V_P reach simultaneously and respectively their highest and lowest values.

Our computation identifies other interaction configuration with comparable high values of M, however since such configurations are not associated with a pure acoustic mode, they are not listed in Table 3.

Since the center acoustic frequency for this interaction can be chosen to be of any convenient low value, see section 6.3.3, these isotropic configurations are considered suitable for deflection as well as modulation applications.

It is noted in Table 3 that the calculated second-order interaction highest M values are listed to have the same values as the corresponding first-order interactions. See section 3.3.2. On the other hand the deflection slope is twice as large as in the latter case; consequently the net deflection for a given acoustic bandwidth is twice that of a first-order interaction. Thus this mode of interaction is very favorable for deflection applications.

Finally in Table 3 , we note that the calculated value of the global figure of merit is of the same order of magnitude as reported previously [19]. These interactions are not subjected to optical absorption [13].

10.1.2.Birefringent AO Interactions.

10.1.2.1.Incident and Diffracted Optic Beams Extraordinary Polarized.

An M value two orders of magnitude higher than in the preceding case is identified in this case and listed in Tables 4 and 5.

This value $M=300000 \times 10^{-15} \sec^{3}/Kg$, associated with a pure quasi shear wave propagating in the X*-direction of the rotated X* Y* Z* axes specified by $\phi=120°$, $\Theta=130°$, $\psi=\pm45°$; $\phi=130°$, $\Theta=130°$, $\psi=-45°$ and $\phi=190°$, $\Theta=50°$, $\psi=45°$.

It is noted that these unusually high M values at the above specified interaction configuration result from a simultaneous occurence of high p_{eff} values of the order of 0.3, intermediately high n values of 5.5 and very low V_P values of 980m/s. Finally, the two configurations above correspond to a pure quasi acoustic shear mode propagating along the specified X* axis.

In this case many very high M value configurations are identified scattered throughout the crystal space and it is noted that they all correspond to $\psi \neq 0°$ configurations i.e. the acoustic beam does not propagate in the XY plane as in cases 1 and 2.

Since the center acoustic frequency for this interaction can also be chosen to be of any convenient low value, thus, from section 6.3.3, these birefringent configurations are suitable for deflection as well as modulation applications.

It is noted in Table 4 that the highest M values for the second-order interactions are again listed to be the same as for the corresponding first-order interactions. See Section 3.3. On the other hand the deflection slope is twice as large as in the latter case; consequently the net deflection slope for a given acoustic bandwidth is again twice that of a first-order interaction. Thus this mode of interaction is very favorable for deflection applications.

Note finally that these interactions are subjected to optic absorption. In Appendix G, two of these giant M values have been verified experimentally.

10.1.2.2. Incident Optic Beam Extraordinary Polarized, Diffracted Optic Beam Ordinary Polarized. Acoustic direction in the XY plane. Right angled AO Triangle. (Fig 3-1c).

A) Region of the crystal, where $\theta < 5°$.

Here the AO triangle is localized by $\phi = 0°$, $\theta = 0°$, $\psi = 0°$, and the highest value of the figure of merit is equal to $230 \times 10^{-15} \sec^3/\mathrm{Kg}$, a value comparable to a previously published result [38].

The Bragg angle is $\Theta_I=1.2°$ inside the crystal and the acoustic center frequency is 24 MHz . This interaction can be used for deflection application but the other configurations specified in the previous sections operating in second-order deflection mode are more than two orders of magnitude more efficient.

B) Region of the crystal, where $\Theta > 5°$.

When we rotate the AO triangle specified in part A) above around an X* axis lying in the XY plane, the M values increase drastically (see Fig 9-3) but the center acoustic frequency f_o predetermined by the AO triangle increases also.

It is to be noted that this f_o value is uniquely determined at each such configuration. This was not the case for the two AO configurations specified in sections 9.2 and 9.3.1.

The highest M value associated with the highest admissible f_o value of 100MHz ,(see section 6.3.3), i.e equal to $3160\mathrm{x}10^{-14}\mathrm{sec}^3/\mathrm{Kg}$ is localized by $\phi=180°$, $\Theta=20°$, $\psi=0°$. A value one order of magnitude larger than for the isotropic case. Furthermore this is a typical deflector configuration with a broad minimum in the angle of incidence and a large deflection slope [37].

A further rotation of Θ increases this high M value but it also results in higher f_o, making deflection applications impossible.

The highest M value is equal to $500000\mathrm{x}10^{-15}\mathrm{sec}^3/\mathrm{Kg}$ corresponding to an AO triangle localized by $\phi=0°$, $\Theta=90°$, $\psi=0°$, and is associated with a pure slow shear wave with respect to the X*,Y*,Z* rotated axes. The center acoustic frequency is f_0=369MHz. The Bragg angle Θ_B=40° inside the crystal. The AO triangle lies in the XY plane. This unusually high M value results from a simultaneous occurence of high p_{eff} value equal to 0.33, highest extraordinary index of refraction of 6.2433 of the incident optic beam and very low V_p value of 979m/s.

This interaction may be suitable only for modulation applications. in Table 4 , the global figure of merit is listed to be $G=22100x10^{-7}(sec/Kg)m^2$, it is one order of magnitude larger than the largest reported value for Te and Ge [19].

The other computed highest M-values, corresponding to the case, same ϕ,same Θ,but $\psi \neq 0$, are found decreasing in magnitude and they are not generally associated with a pure acoustic mode.

10.2.SUMMARY.

In summary, this investigation has resulted in the determination of all the previously unknown terms of the photoelastic tensor, namely p_{65},p_{56},p_{44}, both in magnitude and sign.

In Chapters 8 and 9, it has then been shown that tellurium is capable of efficiently deflecting 10.6μm radiation through large angles over wide bandwidth.

Many outstandingly high efficiency AO first-order interaction configurations have been determined involving extraordinary polarized optic beams associated with an adjustable acoustic center frequency and an M value that is two orders of magnitude higher than ever reported before.

It is important to note that these configurations with high M values are also associated with pure acoustic modes. This allows maximum electric to acoustic power transfer from the transducer into a single acoustic mode inside the crystal.

Second-order isotropic interactions have been evaluated identifying configurations which are expected to provide more than one order of magnitude higher interaction efficiencies than ever reported before, with bandwidth comparable to that of the optimun first-order birefringent interactions.

In the region where optical activity is effective, the M values are found to be relatively weak and about three orders of magnitude lower than for the highest possible M-value configurations.

Finally, considering M as a basis of comparison of materials for AO deflection and modulation applications based on our results and comparing with those obtained by previous workers [19], we conclude that tellurium is superior to any other material for AO deflection and modulation at 10.6μm.

11.CONCLUSION.

A theoretical and experimental description of AO diffraction and deflection in tellurium at 10.6μm for the CO_2 laser, has been presented.

This thesis gives, in Chapter 3, a new theoretical analysis of AO Bragg diffraction in tellurium, taking into account both optical activity which affects the propagation of an extraordinary polarized optical beam near the Z axis where tellurium is transparent to the laser beam, and the finite deviation of the optic as well as the acoustic propagation directions from their respective Poynting vectors. A general expression for the diffraction efficiency is derived for first-order AO interactions for an arbitrary acoustic and optic beam propagation condition consequently a general expression for the figure of merit is derived for first-order birefringent and isotropic AO interactions. The relationship between incident and diffracted Bragg angles in terms of the acoustic frequency is then obtained, leading to the derivation of the deflector parameters.

Based on the above, we have generalized the results of Hecht [46] for multifrequency AO interactions in the Raman Nath and Bragg regimes. Expressions for the diffraction efficiency are found to be different from the first-order case, but the expression of the figure of merit is still the same.

An important contribution of this thesis consists of the experimental results beginning Chapter 6, where first the CO_2 frequency and power stability characteristics are given. Then follows in Chapters 7,8 an experimental program where from diffraction efficiency measurements, the photoelastic tensor components of tellurium which had remained unknown to this date, have been estimated in magnitude and in sign. Then we have measured and verified the AO diffraction and deflection passband characteristics in three typical cases of AO configurations.

A major contribution of this thesis is the calculation of the figure of merit of Chapter 9. It was numerically evaluated for birefringent configurations with optical propagation close to the optical axis where tellurium is transparent, also in the optical absorption region of the crystal, and finally, for isotropic first-order and second-order configurations covering the entire spherical space of the crystal. A three- dimensional quantitative mapping of the figure of merit in tellurium is thus obtained, from which the most favorable regions for deflection as well as modulation applications have been identified.

The final contribution of the thesis is the discussion and summary of the results obtained which appears in Chapter 9. The Tables list the optimun parameters of AO diffraction in tellurium allowing a comparison of the AO diffraction and deflection parameters of first and second-order isotropic and first-order birefringent AO interactions in tellurium. The Tables indicate the superiority of tellurium compared to germanium and therefore to any other known infrared materials for AO diffraction, deflection and modulation at 10.6μm.

R. REFERENCES

[1] S. Fukuda, T. Shiosaki and A. Kanabata. **"Acoustooptic Properties of Tellurium at 10.6μm".** J. Appl. Phys. Volume 50 (6), pp. 3899-3905, 1979.

[2] S. Fukuda, T. Karasaki, T. Shiosaki and A. Kawabata. **"Photoelasticity and AO Diffraction in Piezoelectric Semiconductors".** Physical Review B, Volume 20 (10), pp. 4109-4119, 1979.

[3] D.F. Nelson and M. Lax. **"Theory of Photoelasticity".** Phys. Rev. B, Volume 3 (8), pp. 2778-2794, 1971.

[4] L. Brillouin. **"Diffusion de la lumière et des rayons X par un corps transparent homogène".** Ann. Phy. (Paris), Volume 17, pp. 88-122, 1922.

[5] R. Lucas and P. Biquard. **"Propriétés des milieux solides et liquides soumis aux vibrations élastiques sonores".** J. Phys. Radium, Volume 3, pp. 464-477, 1932.

[6] P. Debye and F.W. Sears. **"Scattering of Light by supersonic waves".** Proc. Nat. Acad. Sci. Volume 18, pp. 409-414, 1932.

[7] C.V. Raman and N.S. Nagendra Nath. **"The Diffraction of Light by High Frequency Sound Waves".** Proc. Indian Acad. Sci, Part I, Volume 2A, pp. 406-412, 1935 ; Part II, Volume 2A, pp.413-420, 1935; Part III, Volume 3A, pp. 75-84, 1936; Part IV, Volume 3A, pp. 119-125, 1936; Part V, Volume 3A, pp. 359-365, 1936.

[8] R.W. Dixon. **"Photoelastic properties of selected materials and their relevance for applications to AO light modulators**

and scanners". J. Appl. Phys. Volume 38, pp. 5149-5153, 1967.

[9] W.R. Klein and B.D. Cook. **"Unified Approach Ultrasonic Light Diffraction".** IEEE Trans. Sonics Ultrasonics, Volume SU-14, pp. 123-134, 1967.

[10] A. Korpel. **"Acoustooptic a review of fundamentals".** Proceedings of the IEEE Volume 69 (1), pp.48-53, 1981.

[11] E.H. Young, Jr and Shi-Kay Yao. **"Design consideration for AO devices".** Proceedings of the IEEE, Volume 69 (1), pp. 54-64, 1981.

[12] I.C. Chang. **"AO Devices and Applications".** IEEE Trans. on Sonics and Ultrasonics, Volume SU-23, pp. 2-22, 1976.

[13] S. Ades and C.H.Champness. **"Intermediate Infrared Optical Absorption in Intrinsic Tellurium".** J. Appl. Phys. Volume 49, pp. 4543-4548, 1978.

[14] A. Yariv. **"Quantum Electronics".** Editor John Wiley, 1975.

[15] A.W. Warner, D.L. White and W.A. Bonner. **"AO light deflectors using optical activity in TeO_2".** J. Appl. Phys. Volume 43, pp. 4489-4495, 1972.

[16] M. King, W.R. Bennet, L.B. Lambert and M.Arm. **"Real-Time Electrooptical Signal Processors with Coherent Detection".** Applied Optics Volume 6 (8), pp. 1367-1375, 1967.

[17] L. Beiser, Ed. **"High Speed Read/Write Techniques for Advanced Printing and Data Handling".** Proceedings of SPIE, Vol.390, Los Angeles, California, January 20-21, 1983.

[18] R. Whitman,A. Korpel,and S. Lotsoff. **"Application of Acoustic Bragg Diffraction to Optical Processing Techniques".** Proceedings. Symp. Modern Optics, pp. 243-255, 1967.

[19] R.J. Presley, Ed. **"CRC handbook of lasers with selected data on optical technology".** Chemical Rubber Co, Cleveland 1971.

[20] D. Maydan. **"AO Pulse modulators"** IEEE J. Quantum Electronics, Volume QE-6, pp. 5-24, 1970.

[21] I. Gorog, J.D. Knox and P.V. Goedertier. **"A television rate laser scanner. General considerations".** RCA Rev. Volume 33 (4),pp. 667-673, 1972.

[22] J.C. Urbach, T.S. Fisli,and G.K. Starkweather. **"Laser scanning for electronic printing".** Proceedings of the IEEE, Volume 70 (6), pp. 597-618, 1982.

[23] B.S. Collins, K.F. Hulme, N.A. Lowde. **"An AO modulator for a CO_2 laser rangefinder using heterodyne detection"** Optical and Quantum Electronics. Volume 12, pp. 419-426, 1960.

[24] M.V. Klein. **"Optics".** Editor Wiley, 1969.

[25] N. Uchida and N. Niizeki. **"AO deflection materials and techniques".** Proceedings of the IEEE, Volume 61 (8), pp.1073-1091, 1971.

[26] B.A. Auld. **"Acoustic Fields and Waves in Solids".** Volume I, Editor Wiley, 1970.

[27] T. Yano, M. Kawabuchi, A. Fukumoto and A. Watanabe. **"TeO_2 anisotropic Bragg light deflector without midband degeneracy".** Appl. Phys. Lett. Volume 26, pp. 689-691, 1975.

[28] A. Jenkins and H.E. White. **"Fundamentals of Optics".** Editor McGraw Hill, 1965.

[29] M. Born and E. Wolf. **"Principle of Optics".** Editor

MacMillan, 1959.

[30] T.C. Poon and A. Korpel. **"High efficiency AO diffraction into the second Bragg order".** IEEE Ultrasonics Symposium Proceedings, pp. 751-754, 1981.

[31] W.P. Mason, T.B. Bateman. **"Relation between Third-Order Elastic Moduli and the Thermal Attenuation of Ultrasonics Waves in Non Conducting and Metallic Crystals".** The Journal of the Acoustical Society of America. Volume 40 (4), pp. 852-862, 1966.

[32] A.R. Hutson and D.L. White. **"Elastic wave propagation in piezoelectric semiconductors".** Journal of Applied Physics, Volume 33 (1),pp. 40-47, 1982.

[33] W.P. Mason and T.B. Bateman. **"Ultrasonic Wave in Pure Silicon and Germanium".** The Journal of the Acoustical Society of America,Volume 36 (4), pp. 644-652, 1964.

[34] D. Souilhac and A.Gundjian. **"Measurement and Theoretical Confirmation of Xe-Enhanced CO_2 Laser Output Power Levels".** Appl. Opt. Volume 20, pp. 3097, 1981.

[35] D. Souilhac and A. Gundjian. **"Carbon Dioxide Laser Stabilization by Optoacoustic Tracking of an SF_6 Lamb Dip".** Appl. Opt. Volume 21 (8), pp. 1478-1481, 1982.

[36] K. Alizadeh. **" CO_2 Laser beam phase modulation interferometry".** Thesis of Master of Science, Elec. Engr. Depart. Mc Gill University, Montreal, P.Q. Canada, September 1977.

[37] J.E.B. Oliviera, E.L. Adler, D. Souilhac and A.A. Gundjian. **"Acoustooptic Diffraction and Deflection in Tellurium at 10.6μm".** IEEE Ultrasonics Symposium Proceedings, pp.

332-340, 1984.

[38] E.L. Adler, A.A. Gundjian, D. Souilhac,and C.H. Champness. **"AO light deflection for the CO_2 laser in optically active tellurium".** Ultrasonics Symposium Proceedings, pp.430-435, 1932.

[39] A.A. Gundjian, E.L. Adler, D. Souilhac and J.E. Oliviera. **"Double-Phonon Scattering-Free and second-order AO Bragg deflection in tellurium at 10.6μm".** Ultrasonics Symposium Proceedings, pp. 471-475, 1983.

[40] C.K. Jen, G.W. Farnell, E.L. Adler, J.E.B. Oliveira. **"Interactive Computer-Aided Analysis of Bulk Acoustic Waves in Materials of Arbitrary Anisotropy and Piezoelectricity".** IEEE Trans. Sonics and Ultrasonics, Volume SU-32, pp.56-60, 1985.

[41] T.M. Reeder, D.K. Winslow. **"Characteristics of microwave acoustic transducer".** IEEE Transactions on Microwave Theory and Techniques. Volume MTT-17, pp. 927-941, 1969.

[42] Z. Turski, L.A. Kraus, Ho-Chung Huang. **"Properties of an X-cut single crystal of lithium niobate transducer".** IEEE Transactions on Sonics and Ultrasonics. Volume SU-29 (6), pp. 402-405, 1975.

[43] G. Arlt and P. Quadflieg. **Electronic Displacement in Tellurium by Mechanical Strain".** Phys. Stat. Solidi. Volume 32, pp. 687-690, 1969.

[44] P. Bammes, R. Klucker, E.E. Koch. **"Anisotropy of the Dielectrtic Constants of trigonal selenium and tellurium between 3 and 30 ev".** Phys. Stat. Solidi, Volume 49 (2), pp. 561-570, 1972.

[45] J. Oliveira and E. Adler. **"Analysis of off-optical axis anisotropic diffraction configurations in positive uniaxial crystals".** Electronics letters, Volume 20, pp. 927-928, 1984.

[46] D.L. Hecht. **"Multifrequency AO Interactions".** IEEE Trans. on Sonics and Ultrasonics. Volume SU-24 (1), pp. 7-18, 1977.

[47] D.L. Hetch, T. Mannigal, J. Rieden and M.Silver. **"Wideband Recording Using AO".** Electrooptic Systems Design Conference Proceedings, pp. 112-116, 1973.

[48] J. Bradford Merry. **"High Speed Read / Write Techniques for Advanced Printing and Data Handling".** Proceedings of SPIE pp. 91-95, 1983.

[49] A.J. Decker, Yoh-Han Pao and P.C. Claspy. **"Electronic Heterodyne Recording and Processing of Optical Holograms, using Phase Modulated Reference Waves".** Applied Optics, Volume 17 (6), pp.917-921, 1978.

[50] J.B. Houston Jr Ed. **"Acoustooptics".** Proceedings of SPIE, Volume 90 August 26-27, 1976. San Diego, California.

[51] A. Vanderlugt. **"Bragg Cell Diffraction Patterns".** Applied Optics Volume 21 (6), pp.1092-1100, 1982.

[52] I.C. Chang, D.L. Hecht. **"Characteristics of AO Devices for Signal Processors".** Proceedings of SPIE, Volume 241, pp.129-138, 1981.

[53] M.G. Cohen and E.I. Gordon. **"Acoustic Beam Probing Using Optical Techniques".** The Bell System Technical Journal, pp. 693-721, 1965.

[54] N. Uchida. **"Fraunhofer Diffraction Pattern Deflected by Highly Absorbed Ultrasound".** Japanese Journal of Applied

Physics, Volume 8 (7), pp. 935-940, 1969.

[55] D.I. Shih. "Crystal Growth and Photoconductivity of Tellurium and Selenium-Tellurium-Alloy". PHD Thesis, McGill University, Electrical Engineering Department, 1981.

[56] R.N. Thurston. "Effect of Electrical and Mechanical Terminating Resistances on Loss and Bandwidth According to the Conventional Equivalent Circuit of a Piezoelectric Transducer" IRE Transactions on Ultrasonics Engineering, Volume 7, pp.16-25, 1960.

[57] R.A. Paananen. "A CO_2-N_2-He-Xe Laser". Proceedings of IEEE, Volume 55 (2), pp. 2035-2035, 1967.

[58] P.O. Clark and J.Y. Wada. "The Influence of Xenon on Sealed-Off CO_2 Lasers". IEEE J. Quantum Electron. Volume QE-4, pp. 263-266, 1968.

[59] K.J. Siemsen. "Axial Gain Distribution in a CW CO_2 Laser". Appl. Opt. Volume 19 (5), pp. 818-821, 1980.

[60] L.W. Casperson. "Laser power calculations: Sources of error". Appl. Opt. Volume 19 (3), pp. 422-434, 1980.

[61] J. Ried and K.J.Siemsen. "Laser power gain measurements on the sequence bands of CO_2 ". Journal of Applied Physics, Volume 48 (7), pp. 2712-2717, 1977.

[62] M.W. Golberg and R. Yusek. "High Resolution Inverted Lamb-Dip Spectroscopy on SF_6". Appl. Phys. Lett. Volume 17 (8), pp. 349-351, 1970.

[63] M.W. Golberg and R. Yusek. "Doppler Jitter Stabilization of a CO_2 Laser". Appl. Phys. Lett. Volume 18 (4), pp. 135-136, 1971.

[64] A. Di Lieto, P. Minguzzi and Tonelli. "Sub-Doppler

Optoacoustic Spectroscopy". Opt. Commun. Volume 31 (1), pp.25-27, 1979.

[65] E.L. Kerr and J.G. Atwood. **"The laser Illuminated Absorptivity Spectrophone: A Method for Measurement of Weak Absorptivity in Gases at Laser Wavelengths".** Appl. Opt. Volume 7 (5), pp. 915-921, 1968.

[66].R.D. Kamm. **"Detection of weakly absorbing gases using a resonant optoacoustic method".** J. Appl. Phys. Volume 47 (8), pp. 3550-3558, 1976.

[67] F.W. Fraim and P.V. Murphy. **"Electrets in miniature microphone".** J. Acoust. Soc. Am. Volume 53 (6), pp. 1601-1608, 1972.

[68] D.R. Wake and N.M. Amer. **"The dependence of an acoustically non resonant optoacoustic signal on pressure and buffer gases".** Appl. Phys. Lett. Volume 34 (6), pp.379-381, 1979.

[69] D.G. Hawkins. **"Resolution Criteria for Acoustooptic Deflector"** Appl. Optics, Vol.19 (2), pp.186, 1980.

[70] D.Royer and E. Dieulesaint. **"Elastic and Piezoelectric Transducers for Frequencies Above 100MHz"** J. App. Phys., Volume 50, pp.4042-4045, 1979.

[71] E.K. Sittig. **"Design and Technology of Piezoelectric Transducers for Frequencies Above 100MHz"** Physical Acoustics, Edited by W.P.Mason and R.N.Thurston, Volume 9, pp.221-275, 1972.

[72] L.B. Kreuzer and C.F. Dewey,Jr. **"Optoacoustic Spectroscopy and Detection".** Chapt.1 and 3. Edited by Yoh-Han Pao, Academic Press, 1977.

[73] J.P. Monchalin,M.L. Meyer, J.M. Gagné, L. Bertrand. **"Détection et Spectroscopie Optoacoustiques avec Lasers: État des Recherches".** Rapport EP 78-R-39. École Polytechnique de Montreal, 1979.

[74] W.E. Lamb. **"Quantum Electronics and Coherent Light".** Academic Press, Inc, New-York.Editor Miles, pp.78, 1964.

[75] A.E. Siegman. **"An Introduction to Lasers and Masers".** Editor McGraw-Hill, New York, 1971.

[76]. J.D. Knox and Yoh-Han Pao. **"Absorption Profiles and Inverted Lamb Dips of I_2 Vapor at 633mn as Studied with He-Ne".** Appl.Phys.Letters, Vol.16 (3), pp.129-131, 1970.

[77] W.K.Pratt. **"Laser Communication Systems".** Editor John Wiley, New York, 1968.

[78] A.Waksberg. **"Range Predictions for a CO_2 Laser Communication System".** Applied Optics ,Vol.20 (15), pp.2688-2693, 1981.

[79] P.W.Pace and James M.Cruickshank. **"A Frequency Stabilized Compact High Repetition Rate TEA-CO_2 Laser".** IEEE Journal of Quantum Electronics, Vol.QE-16 (9), pp.937-944, 1980.

[80] P.Pace and J. Cruickshank". **"Frequency-Stabilized Hybrid CO_2 Laser".** SPIE, Vol.227 CO_2 Laser Devices and Applications, pp.28-34, 1980.

[81] J.M.Cruickshank. **"Tranversely Excited Atmospheric CO_2 Laser Radar with Heterodyne Detection".** Applied Optics, Vol.18 (3), pp.290-293, 1979.

[82]. B. Cooper. **"Optical Communications in the Earth's Atmosphere".** IEEE Spectrum, pp.83-86, 1966.

APPENDIX A

COMPUTER PROGRAMS AND LISTINGS OF THE HIGH M-FIGURES OF MERIT.

This Appendix presents the computer program used to calculate the figure of merit for the isotropic and birefringent AO interactions specified in Chapter 9.

The highest M-values corresponding to extraordinary polarized optic beams associated with an adjustable acoustic center frequency are tabled following the listing of the computer program.

1.Computation of the figure of merit

1.1.Introduction.

The calculation of the figure of merit, requires for a general AO wavevector triangle configuration, the calculation of the corresponding direction cosines of the acoustic wave propagation and polarization vectors, the acoustic phase velocity of each of the three modes, the direction cosines of the polarization directions of the optic beams and finally, the values of the indices of refraction and the density of the material.

The most difficult term to calculate in the expression of the figure of merit is p_{eff}. It was calculated in the following way:

1.2. Expression of p_{eff}.

It can be shown that the expression of $p_{eff} = d_m d_n p_{mnkl} a_l b_k$, of Eq (3-23), can also be written as:

$$p_{eff} = (b_1, b_2, b_3) \begin{vmatrix} A_{21} & A_{12} & A_{13} \\ A_{21} & A_{22} & A_{23} \\ A_{31} & A_{32} & A_{33} \end{vmatrix} \begin{vmatrix} a_1 \\ a_2 \\ a_3 \end{vmatrix} \tag{A-1}$$

Where the A_{ij} coefficients are expressed in the listing of the computer program presented at the end of the Appendix and a_l, b_k are obtained from an available acoustic wave program [40]. Equation (A-1) was used in the computation.

1.3. Expression of the Direction Cosines of the Optic and Acoustic Beams.

1.3.1. Isotropic Interactions.

In Fig 3-1c , the direction cosines of the polarization vector for the ordinary polarized optic beam are equal to (Θ_I^* small):

$$d_1^{I,D} = \cos\phi \ ; \quad d_2^{I,D} = \sin\phi \ ; \quad d_3^{I,D} = 0 \tag{A-2}$$

The direction cosines for the propagation wavevector of the acoustic beam, are:

$$\begin{aligned} a_1 &= -\sin\psi\sin(\Theta+90)\cos(\Theta-90)-\cos\psi\sin(\phi-90) \\ a_2 &= -\sin\psi\sin(\Theta+90)\sin(\phi-90)+\cos\psi\cos(\phi-90) \\ a_3 &= -\sin\psi\cos(\Theta+90) \end{aligned} \tag{A-3}$$

Where ϕ,Θ,ψ are the three Euler angles locating the rotated X*Z* plane.

1.3.2.Birefringent Interactions

1.3.2.1. Birefringent Interactions with Incident Optic Beam Extraordinary Polarized and Diffracted Optic Beam Ordinary Polarized.(Right angled AO triangle).

In Fig (3-1c), when $\Theta_D^*=0$, the direction cosines of the polarization vector for the ordinary polarized optic beam are:

$$d_1^I = -\cos\phi \qquad d_2^I = \sin\phi \qquad d_3^D = 0 \tag{A-4}$$

and for the incident extraordinary polarized optic beam:

$$d_1^I = -\cos\Theta_I\sin\phi \quad d_2^I = -\cos\Theta_I\cos\phi \quad d_3^I = \sin\Theta_I \tag{A-5}$$

Where $\phi\ \Theta\ \psi$ are the three Euler angles.

The expressions for the direction cosines of the acoustic beam are the same as in Eq(A-3).

1.3.2.2.Birefringent Interactions with Incident and Diffracted Optic Beams Extraordinary Polarized.

In Fig 3-1c, the direction cosines of the polarization vector for the extraordinary polarized optic beam are equal to (Θ_I^* small):

$$d_1^{I,D}= -\cos\Theta\sin\phi \quad d_2^{I,D}= -\cos\Theta\cos\phi \quad d_3^{I,D}= \sin\Theta . \tag{A-6}$$

The expressions for the direction cosines of the acoustic beam are the same as in Eq(A-3).

2.Computer Program and Listings of the Highest M Figures of Merit for birefringent interactions with extraordinary polarized optic beams.

This computer program is now presented, followed by a listing of the highest M values computed for this interaction.

BIREFRINGENT AO INTERACTIONS IN TELLURIUM
EXTRAORDINARY POLARIZED OPTIC BEAMS
LISTING OF THE COMPUTER PROGRAM AND
LISTING OF THE HIGHEST M VALUES.

```
/INC OSJE

//EE79SAS3 JOB (EE79,001,70,300,,42),MSGLEVEL=1
/*ROUTE  PRINT CENx27
//*PASSWORD=DOM
// EXEC SAS
 OPTIONS MLOGIC NOMPRINT MACROGEN SYMBOLGEN OBS=6;
**********************************************************************
* MACRO TO CALCULATE THE FIGURE OF MERIT MEFOR THIRD  DEFLECTOR MODE
**********************************************************************;
%MACRO MECALC (VP=,
               B=,
               DTHETAA=,
               DTHETAI=,
               DPHK=,
               DPHJ=,
               DPSI=,
               NO=4.7939,
               NE=6.2433,
               RHO=6210);

        P=&PVAL;
        A=&AVAL;
        AA=&AAVAL;
        DEG= ATAN(1)#/ 45;  %* CALCULATE # OF DEGREES/RADIANS;
        THETAA= &DTHETAA#DEG;
        PSI=&DPSI#DEG;
thetai=&dthetai#deg;
PHK =&DPHK#DEG;
NI=SQRT(1#/(((SIN(THETAA)##2)#/(&NO##2))
+((COS(THETAA)##2)#/(&NE##2))));
ND=SQRT(1#/(((SIN(THETAA)##2)#/(&NO##2))
+((COS(THETAA)##2)#/(&NE##2))));
    DI= 0 0 0;
     DI(1,1) = -SIN(THETAA)#COS(PHK);
     DI(1,2) = -SIN(THETAA)#SIN(PHK);
     DI(1,3) = -COS(THETAA);

   PEFF =&B * A * AA;  %* B = ARRAY (1 BY 3)
                              A = ARRAY (3 BY 3)
                              AA= ARRAY (3 BY 1)
                              THUS FINAL RESULT IS PEFF= ARRAY (1 BY 1);

   ME =( (NI ##3) # (ND ##3) # (PEFF ##2))
              #/ (&RHO # (&VP ##3));
%MEND MECALC;


%MACRO FQCALC (VP=,
NO=4.7939,
dthetai=);
deg=atan(1)#/45; %* calculate # of degrees/radians;
thetai=&dthetai#deg;
dthetai=5;
     FQ=((&VP)#(2)#(&NO))#(SIN(THETAI))#/(10.6);
%MEND FQCALC;

**********************************************************************
* MACRO TO CALCULATE THE NEW AA FOR THE THIRD DEFLECTION MODE*
```

```
********************************************************************;
 %MACRO CALCNWAA(DTHETAA=, DPHK=,DPSI=);
  DEG = ATAN(1) #/ 45; %*CONVERT TO DEGREES;
        PHK =&DPHK#DEG;
      PSI=&DPSI#DEG;

     THETAA=&DTHETAA#DEG;
  NEWAA = 0 / 0 / 0;
  NEWAA(1,1) =-(SIN(PSI)#SIN(THETAA)#COS(PHK))-(COS(PSI)#SIN(PHK));

  NEWAA(2,1) =-(SIN(PSI)#SIN(THETAA)#SIN(PHK))+(COS(PSI)#COS(PHK));

  NEWAA(3,1) = -(SIN(PSI)#COS(THETAA));
%MEND  CALCNWAA;
********************************************************************
* MACRO TO CALCULATE THE ORIGINAL "A" FOR THIRD     DEFLECTION MODE
********************************************************************;
%MACRO CALCORGA(DTHETAA=,DPHK=);
  P= &PVAL;
DEG=ATAN(1)#/45; %*CONVERT TO DEGREES;
THETAA=&DTHETAA#DEG;
PHK=&DPHK#DEG;
DD= 0 0 0;
 DD(1,1) = -SIN(THETAA)#COS(PHK);
 DD(1,2) = -SIN(THETAA)#SIN(PHK);
 DD(1,3) = -COS(THETAA);


DI= 0 0 0;
 DI(1,1) = -SIN(THETAA)#COS(PHK);
 DI(1,2) = -SIN(THETAA)#SIN(PHK);
 DI(1,3) = -COS(THETAA);


  ORGA= 0 0 0/
        0 0 0/
        0 0 0;
    ORGA(1,1) = P(1,1)#DI(1,1)#DD(1,1)+P(6,1)#DI(1,1)#DD(1,2)+P(5,1)#
                DI(1,1)#DD(1,3)+
                P(6,1)#DI(1,2)#DD(1,1)+P(2,1)#DI(1,2)#DD(1,2)+P(4,1)#
                DI(1,2)#DD(1,3)+
                P(5,1)#DI(1,3)#DD(1,1)+P(4,1)#DI(1,3)#DD(1,2)+P(3,1)#
                DI(1,3)#DD(1,3);
    ORGA(1,2) = P(1,6)#DI(1,1)#DD(1,1)+P(6,6)#DI(1,1)#DD(1,2)+P(5,6)#
                DI(1,1)#DD(1,3)+
                P(6,6)#DI(1,2)#DD(1,1)+P(2,6)#DI(1,2)#DD(1,2)+P(4,6)#
                DI(1,2)#DD(1,3)+
                P(5,6)#DI(1,3)#DD(1,1)+P(4,6)#DI(1,3)#DD(1,2)+P(3,6)#
                DI(1,3)#DD(1,3);
    ORGA(1,3) = P(1,5)#DI(1,1)#DD(1,1)+P(6,5)#DI(1,1)#DD(1,2)+P(5,5)#
                DI(1,1)#DD(1,3)+
                P(6,5)#DI(1,2)#DD(1,1)+P(2,5)#DI(1,2)#DD(1,2)+P(4,5)#
                DI(1,2)#DD(1,3)+
                P(5,5)#DI(1,3)#DD(1,1)+P(4,5)#DI(1,3)#DD(1,2)+P(3,5)#
                DI(1,3)#DD(1,3);
    ORGA(2,1) = P(1,6)#DI(1,1)#DD(1,1)+P(6,6)#DI(1,1)#DD(1,2)+P(5,6)#
               DI(1,1)#DD(1,3)+
                P(6,6)#DI(1,2)#DD(1,1)+P(2,6)#DI(1,2)#DD(1,2)+P(4,6)#
                DI(1,2)#DD(1,3)+
```

```
                P(5,6)#DI(1,3)#DD(1,1)+P(4,6)#DI(1,3)#DD(1,2)+P(3,6)#
                DI(1,3)#DD(1,3);
     ORGA(2,2) = P(1,2)#DI(1,1)#DD(1,1)+P(6,2)#DI(1,1)#DD(1,2)+P(5,2)#
                 DI(1,1)#DD(1,3)+
                 P(6,2)#DI(1,2)#DD(1,1)+P(2,2)#DI(1,2)#DD(1,2)+P(4,2)#
                 DI(1,2)#DD(1,3)+
                 P(5,2)#DI(1,3)#DD(1,1)+P(4,2)#DI(1,3)#DD(1,2)+P(3,2)#
                 DI(1,3)#DD(1,3);
     ORGA(2,3) = P(1,4)#DI(1,1)#DD(1,1)+P(6,4)#DI(1,1)#DD(1,2)+P(5,4)#
                 DI(1,1)#DD(1,3)+
                 P(6,4)#DI(1,2)#DD(1,1)+P(2,4)#DI(1,2)#DD(1,2)+P(4,4)#
                 DI(1,2)#DD(1,3)+
                 P(5,4)#DI(1,3)#DD(1,1)+P(4,4)#DI(1,3)#DD(1,2)+P(3,4)#
                 DI(1,3)#DD(1,3);
     ORGA(3,1) = P(1,5)#DI(1,1)#DD(1,1)+P(6,5)#DI(1,1)#DD(1,2)+P(5,5)#
                 DI(1,1)#DD(1,3)+
                 P(6,5)#DI(1,2)#DD(1,1)+P(2,5)#DI(1,2)#DD(1,2)+P(4,5)#
                 DI(1,2)#DD(1,3)+
                 P(5,5)#DI(1,3)#DD(1,1)+P(4,5)#DI(1,3)#DD(1,2)+P(3,5)#
                DI(1,3)#DD(1,3);
     ORGA(3,2) = P(1,4)#DI(1,1)#DD(1,1)+P(6,4)#DI(1,1)#DD(1,2)+P(5,4)#
                 DI(1,1)#DD(1,3)+
                 P(6,4)#DI(1,2)#DD(1,1)+P(2,4)#DI(1,2)#DD(1,2)+P(4,4)#
                 DI(1,2)#DD(1,3)+
                 P(5,4)#DI(1,3)#DD(1,1)+P(4,4)#DI(1,3)#DD(1,2)+P(3,4)#
                 DI(1,3)#DD(1,3);
     ORGA(3,3) = P(1,3)#DI(1,1)#DD(1,1)+P(6,3)#DI(1,1)#DD(1,2)+P(5,3)#
                 DI(1,1)#DD(1,3)+
                 P(6,3)#DI(1,2)#DD(1,1)+P(2,3)#DI(1,2)#DD(1,2)+P(4,3)#
                 DI(1,2)#DD(1,3)+
                 P(5,3)#DI(1,3)#DD(1,1)+P(4,3)#DI(1,3)#DD(1,2)+P(3,3)#
                 DI(1,3)#DD(1,3);
%MEND  CALCORGA;
**********************************************************************
**********************************************************************
PROGRAM TO ACCEPT DATA PRODUCED BY THE "BULK2" FORTRAN PROGRAM.      *
**********************************************************************
**********************************************************************;

  DATA BULK2;
    INPUT PHO THETA PSI VP B1 B2 B3;

CARDS;
/INC BULK2.DATA
PROC MATRIX;
  FETCH MAT DATA=BULK2;
  NOOBS= NROW(MAT);

  %LET PVAL = 0.164  0.138  0.146 -0.04  0      0      /
              0.138  0.164  0.146  0.04  0      0      /
              0.086  0.086  0.038  0     0      0      /
              0.27  -0.27   0      0.2   0      0      /
              0      0      0      0     0.2    0.27   /
              0      0      0      0    -0.04   0.013   ;

  MAT2=J(NOOBS,5,0);
  MAT = SHAPE( MAT || MAT2,12);

  DO I = 1 TO NOOBS;
```

```
   _PHK    = MAT(I,1)-90;
DEG    =ATAN(1)#/45;  * CALCULATE# OF DEGREES/RADIANS;
   _PHK    = _PHK#DEG;
  _THETA=MAT(I,2);
  _THETAA=MAT(I,2)+90;
   MAT(I,8)=_THETAA;
  _PSI=MAT(I,3);
  _PSI=_PSI#DEG;
  MAT(I,3)=_PSI;
  _THETAI=5;
  MAT(I,9)=_THETAI;
  _VP     = MAT(I,4);
  _B = 0 0 0;
  _B(1,1)= MAT(I,5);
  _B(1,2)= MAT(I,6);
  _B(1,3)= MAT(I,7);
 *  START    =====> THIRD   MODE OF DEFLECTION;
      %CALCORGA(DTHETAA=_THETAA,DPHK=_PHK);
      %LET AVAL= ORGA;
      %CALCNWAA (DTHETAA=_THETAA, DPHK=_PHK,DPSI=_PSI);

      %LET AAVAL= NEWAA;
      %MECALC (B=_B,
               VP=_VP,
               DPHK=_PHK,
               DPSI=_PSI,
               DTHETAI=_THETAI,
               DTHETAA=_THETAA);

%FQCALC (VP=_VP,
NO=4.7939,
DTHETAI=_THETAI);

 *  END      =====> THIRD   MODE OF DEFLECTION;

  MAT(I,1)=_PHK;
  MAT(I,3)=_PSI;
  MAT(I, 8)= _THETAA;
  MAT(I, 9)=_THETAI;
  MAT(I,10)= ME;
  MAT(I,11)= FQ;
  MAT(I,12)= PEFF;
  END;



OUTPUT MAT OUT=SASOUT(RENAME=(COL1=PHK COL2=THETA COL3=PSI
           COL4=VP COL5=WB1 COL6=WB2 COL7=WB3 COL8=THETAA
           COL9=THETAI COL10=ME COL11=FQ COL12=PEFF));
STOP;
PROC SORT; BY PHK THETA VP;
PROC PRINT
DATA=SASOUT;
DATA OUT1 OUT2 OUT3; SET SASOUT;
IF ME < 1.0E-14 THEN ME=1.0E-14;
IF ME > 1.0E-9 THEN ME=1.0E-9;
IF MOD(_N_,3)=1 THEN OUTPUT OUT1;
```

```
ELSE IF MOD(_N_,3)=2 THEN  OUTPUT OUT2;
ELSE OUTPUT OUT3;

PROC     G3D DATA=OUT1;
PLOT   THETAA*PHK=ME/CAXIS=RED CTEXT=GREEN TILT=45 ROTATE=45;

TITLE .C=RED .F=COMPLEX THE FIGURE OF MERIT;
PROC  G3D  DATA=OUT2;
PLOT  THETAA*PHK=ME/CAXIS=RED CTEXT=GREEN TILT=45 ROTATE=45;
TITLE .C=RED  .F=COMPLEX THE FIGURE OF MERIT;
PROC  G3D  DATA=OUT3;
PLOT  THETAA*PHK=ME/CAXIS=RED CTEXT=GREEN TILT=45 ROTATE=45;
TITLE .C=RED .F=COMPLEX  THE FIGURE OF MERIT;
```

TABLE 5

HIGHEST M VALUES FOR BIREFRINGENT AO INTERACTIONS WITH INCIDENT AND DIFFRACTED OPTIC BEAMS EXTRAORDINARY POLARIZED

$Mx10^{-15}$ (sec^3/Kg)	P_{eff} (MKSA)	V_P (m/s)	Acoustic Polarization Direc.Cosines (Rotated Axes)	Acoustic Direction (ϕ,Θ,ψ)	f_o (MHz) ($\Theta_B^*=5^0$)	ANGLE ($\vec{V}_P,\vec{V}_G$)
105860	0.26	1439	0.0,-0.64,0.76	90, 50, 0	113	44.6
107996	0.23	1439	0.0,-0.50,0.86	90, 60, 0	113	44.6
107996	0.23	1439	0.0,0.50,0.86	90,120, 0	113	44.6
105859	0.26	1439	0.0,0.64,0.76	90,130, 0	113	44.6
118385	0.20	1066	0.13,-0.96,0.23	90, 40,15	84	44.8
173052	0.22	1067	0.13,-0.90,0.40	90, 50,15	84	43.6
146890	0.16	1089	0.11,-0.64,0.75	90, 70,15	85	43.2
146890	0.16	1089	0.11,-0.64,0.75	90,110,15	85	43.2
192535	0.20	1075	0.12,-0.80,0.58	90,120,15	84	43.3
173052	0.22	1067	0.13,-0.96,0.40	90,130,15	84	43.6
118385	0.20	1066	0.13,-0.96,0.23	90,140,15	84	44.8
104571	0.15	994	0.044,-0.92,0.38	100, 50,15	78	7.9
116585	0.14	998	0.056,-0.84,0.53	100, 60,15	78	5.5
133461	0.15	1094	0.11,0.036,0.99	100,110,15	86	43.5
239903	0.24	1137	0.076,0.33,0.93	100,120,15	89	44.2
224026	0.28	1177	0.087,0.64,0.76	100,130,15	92	43.4
150077	0.28	1209	0.06,-0.85,0.52	100,140,15	95	45.9
150077	0.28	1209	0.061,-0.85,0.52	200, 40,15	114	45.9
224026	0.28	1177	-0.008,-0.64,0.76	200, 50,15	92	43.4
239903	0.24	1137	-0.076,-0.33,0.93	200, 60,15	89	44.2
171858	0.17	1094	0.11,0.036,0.99	200, 70,15	86	43.5
116585	0.14	998	0.056,-0.84,0.53	200,120,15	78	5.5
104571	0.15	994	0.044,-0.92,0.38	200,130,15	78	7.9
200143	0.29	1239	-0.40,0.11,0.90	90, 50,45	97	47.8
269830	0.25	1124	-0.30,0.23,0.92	90, 60,45	88	25.1
210484	0.19	1110	-0.20,0.30,0.92	90, 70,45	87	22.6
210484	0.19	1110	0.20,-0.30,0.92	90,110,45	87	22.6
269830	0.25	1124	0.30,-0.23,0.92	90,120,45	88	25.0
200143	0.29	1239	0.40,-0.11,0.90	90,130,45	97	47.8
209947	0.24	1171	-0.35,0.40,0.84	100, 60,45	92	37.6
194563	0.19	1130	0.12,-0.17,0.99	100,110,45	89	39.4
295831	0.25	1089	0.22,-0.20,0.97	100,120,45	85	11.6
263689	0.30	1152	0.33,0.11,0.93	100,130,45	90	39.5
176668	0.33	1293	0.37,0.59,0.71	100,140,45	101	42.1
158880	0.18	1149	0.017,-0.52,0.85	110,110,45	90	43.4
281642	0.24	1081	0.11,0.31,0.94	110,120,45	85	32.9
309211	0.29	1071	0.21,0.39,0.89	110,130,45	84	23.6

245456	0.32	1128	0.18,0.85,0.48	110,140,45	88	42.3
120886	0.24	1093	0.057,0.99,-0.55	110,150,45	86	49.0
101147	0.14	1123	-0.14,0.85,0.49	120,110,45	88	36.7
225658	0.22	1082	0.62,-0.77,0.63	120,120,45	85	37.1
285422	0.26	1027	0.049,0.69,0.71	120,130,45	81	25.5
269336	0.29	1023	0.058,0.89,0.43	120,140,45	80	23.6
158432	0.24	1016	-0.039,0.99,0.06	120,150,45	80	12.1
130024	0.16	1083	-0.19,0.94,0.26	130,120,45	85	17.5
177526	0.21	1041	0.13,-0.89,0.41	130,130,45	82	22.2
150682	0.21	1004	-0.018,0.84,0.54	130,140,45	79	7.9
108038	0.21	1034	0.014,-0.94,0.32	130,150,45	81	26.9
108038	0.21	1034	0.014,-0.94,0.32	170, 30,45	81	26.9
150682	0.21	1004	0.018,-0.84,0.54	170, 40,45	79	7.9
177526	0.21	1041	0.13,-0.89,0.41	170, 50,45	82	22.2
130024	0.17	1083	0.19,-0.94,0.26	170, 60,45	85	17.5
158432	0.25	1016	-0.039,0.99,0.006	180, 30 45	80	12.1
269336	0.29	1023	-0.058,-0.89,0.43	180, 40,45	80	23.6
285422	0.26	1027	-0.049,-0.69,0.71	180, 50,45	81	25.5
225657	0.22	1082	0.062,-0.77,0.63	180, 60,45	85	37.1
101147	0.14	1123	0.14,-0.85,0.49	180, 70,45	88	36.7
120886	0.24	1093	0.057,0.99,0.005	190, 30,45	86	49.0
245456	0.32	1128	-0.18,-0.85,0.48	190, 40,45	88	42.3
309211	0.29	1071	-0.21,-0.39,0.89	190, 50,45	84	23.6
281642	0.24	1081	-0.11,-0.31,0.94	190, 60,45	85	32.9
158880	0.18	1149	0.017,-0.52,0.85	190, 70,45	90	43.4
176669	0.33	1293	-0.37,-0.59,0.71	200, 40,45	101	42.1
263689	0.30	1152	-0.33,-0.11,0.93	200, 50,45	90	39.5
295831	0.25	1089	-0.22,0.020,0.97	200, 60,45	85	11.6
194563	0.19	1130	-0.12,0.017,0.99	200, 70,45	89	39.4
209947	0.24	1171	0.35,-0.40,0.84	200,120,45	92	37.6
176511	0.24	1140	0.27,-0.24,0.93	100,130,75	89	11.2
192973	0.25	1140	0.25,-0.074,0.96	110,130,75	89	15.9
139625	0.27	1210	0.39,-0.038,0.91	110,140,75	95	42.6
175389	0.24	1144	0.23,0.097,0.96	120,130,75	90	25.4
141288	0.26	1179	0.36,0.13,0.92	120,140,75	92	38.4
141287	0.26	1179	-0.36,-0.13,0.93	180, 40,75	92	38.4
175389	0.24	1144	-0.23,-0.097,0.96	180, 50,75	90	25.4
139625	0.27	1210	-0.39,0.038,0.91	190, 40,75	95	42.6
175389	0.24	1140	-0.25,0.074,0.96	190, 50,75	89	15.9
176511	0.24	1140	-0.27,0.24,0.93	200, 50,75	89	11.2
176783	0.24	1155	0.34,-0.33,0.87	100,140,90	91	30.9
176783	0.25	1155	0.24,0.0.0.97	120,130,90	91	25.9
141825	0.26	1190	0.37,0.0,0.92	120,140,90	93	38.6
160975	0.23	1158	0.23,0.17,0.95	130,130,90	91	28.1
132251	0.25	1181	0.36,0.16,0.91	130,140,90	93	36.9
176783	0.24	1155	0.34,0.33,0.87	140,140,90	91	30.9
176783	0.24	1155	0.24,0.0,0.97	120,130,90	91	25.9
141825	0.26	1190	0.37,0.0,0.92	120,140,90	93	38.6
160975	0.23	1158	0.23,0.16,0.95	130,130,90	91	28.1
132251	0.25	1181	0.36,0.16,0.91	130,140,90	93	36.9
104794	0.21	1155	0.34,0.33,0.87	140,140,90	91	30.9
104795	0.22	1155	-0.34,-0.33,0.87	160, 40,90	91	30.9
132251	0.25	1181	-0.36,-0.16,0.91	170, 40,90	93	36.9
160975	0.23	1158	-0.23,-0.16,0.95	170, 50,90	91	28.1
141825	0.26	1190	-0.37,0.0,0.92	180, 40,90	93	38.6

176783	0.25	1150	-0.24,0.0,0.97	180, 50,90	91	25.9
132251	0.25	1181	-0.36,0.16,0.91	190, 40,90	93	36.9
160975	0.23	1158	-0.23,0.16,0.95	190, 50,90	91	28.1
104795	0.21	1155	-0.34,0.33,0.87	200, 40,90	91	30.9
102293	0.23	1210	-0.39,-0.038,0.9	170, 40,-75	95	42.6
139625	0.27	1140	0.25,0.074,0.96	170, 50,-75	89	15.9
175389	0.24	1144	0.23,-0.09,0.96	180, 50,-75	90	25.4
177526	0.21	1041	0.12,0.89,0.42	110,130,-45	82	22.2
150682	0.21	1004	0.017,0.84,0.54	110,140,-45	79	7.9
108038	0.21	1034	0.014,0.94,0.32	110,150,-45	81	26.9
225657	0.22	1082	0.062,0.77,0.63	120,120,-45	85	37.1
285422	0.26	1027	-0.049,0.69,0.71	120,130,-45	81	25.5
269336	0.29	1023	-0.058,0.89,0.43	120,140,-45	80	23.6
158432	0.25	1016	0.039,0.99,-0.6	120,150,-45	80	12.1
210802	0.20	1149	0.017,0.52,0.85	130,110,-45	90	43.4
281642	0.24	1081	-0.11,0.31,0.94	130,120,-45	85	32.9
309211	0.29	1071	-0.21,0.36,0.89	130,130,-45	84	23.6
245456	0.32	1128	-0.18,0.85,0.48	130,140,-45	88	42.3
209947	0.24	1171	0.35,0.40,0.84	140, 60,-45	92	37.6
194563	0.19	1130	-0.12,-0.017,0.99	140,110,-45	89	39.4
295831	0.25	1089	-0.22,-0.020,0.97	140,120,-45	85	11.6
263689	0.30	1152	-0.33,0.11,0.93	140,130,-45	90	39.5
176669	0.33	1293	-0.37,0.59,0.71	140,140,-45	101	42.1
200143	0.29	1239	0.40,0.11,0.90	150, 50,-45	97	47.8
269831	0.25	1124	0.30,0.23,0.92	150, 60,-45	88	25.1
210484	0.19	1110	0.20,0.31,0.92	150, 70,-45	87	22.6
210484	0.19	1110	-0.20,-0.30,0.92	150,110,-45	87	22.6
269831	0.25	1124	-0.30,-0.23,0.92	150,120,-45	88	25.0
200143	0.29	1239	-0.40,-0.11,0.90	150,130,-45	97	47.8
138628	0.26	1311	-0.45,-0.30,0.84	160,130,-45	101	50.8
263689	0.30	1152	0.33,-0.11,0.93	160, 50,-45	90	39.5
295831	0.25	1089	0.22,0.02,0.97	160, 60,-45	85	11.6
194563	0.19	1130	0.12,0.017,0.99	160, 70,-45	89	39.4
209947	0.24	1171	-0.35,-0.40,0.84	160,120,-45	92	37.6
120886	0.24	1093	-0.057,0.99,-0.005	170, 30,-45	86	49.0
245463	0.32	1128	0.18,-0.85,0.48	170, 40,-45	88	42.2
309213	0.29	1071	0.21,-0.39,0.89	170, 50,-45	84	23.6
281642	0.24	1081	0.11,-0.31,0.94	170, 60,-45	85	32.9
158880	0.17	1149	0.017,0.52,0.85	170, 70,-45	90	43.4
158432	0.25	1016	0.039,0.99,-0.006	180, 30,-45	80	12.1
269336	0.29	1023	0.05,-0.89,0.43	180, 40,-45	80	23.6
285422	0.26	1027	0.049,-0.69,0.71	180, 50,-45	81	25.5
225658	0.22	1082	0.06,0.77,0.63	180, 60,-45	85	37.1
101146	0.14	1123	-0.14,-0.85,0.49	180, 70,-45	88	36.7
108038	0.21	1034	0.014,0.94,0.32	190, 30,-45	81	26.8
150682	0.21	1004	0.017,0.84,0.54	190, 40,-45	79	7.9
177526	0.21	1041	0.13,0.89,0.41	190, 50,-45	82	22.2
130024	0.17	1083	-0.19,-0.94,0.26	190, 60,-45	85	17.5
104571	0.15	994	0.044,0.92,0.37	140, 50,-15	78	7.9
116585	0.14	998	0.056,0.84,0.53	140, 60,-15	78	5.5
239903	0.24	1137	-0.076,0.33,0.93	140,120,-15	89	44.2
224026	0.29	1177	-0.08,0.64,0.76	140,130,-15	92	43.4
150077	0.28	1209	0.06,0.85,0.52	140,140,-15	95	45.9
118385	0.20	1066	0.13,0.96,0.23	150, 40,-15	84	44.8
173052	0.22	1067	0.13,0.90,0.40	150, 50,-15	84	43.6

192534	0.20	1075	0.12,0.80,0.58	150, 60,-15	84	43.3
146891	0.16	1089	0.11,0.64,0.75	150, 70,-15	85	43.2
146890	0.16	1089	0.11,0.64,0.75	150,110,-15	85	43.2
192534	0.20	1075	0.12,0.80,0.58	150,120,-15	84	43.3
173052	0.22	1067	0.13,0.90,0.40	150,130,-15	84	43.6
118385	0.20	1066	0.13,0.96,0.23	150,140,-15	84	44.8
150077	0.28	1209	0.061,0.85,0.52	160, 40,-15	95	45.9
224026	0.28	1177	0.0087,-0.64,0.76	160, 50,-15	92	43.4
239903	0.24	1137	0.076,-0.33,0.93	160, 60,-15	89	44.2
171858	0.17	1094	0.11,-0.036,0.99	160, 70,-15	86	43.5
116585	0.14	998	0.056,0.84,0.53	160,120,-15	78	5.5
104571	0.15	994	0.044,0.92,0.38	160,130,-15	78	7.9

APPENDIX B

Elastic,Piezoelectric and Dielectric Constants of the Trigonal-32 Crystals [40].

a)Elastic Stiffness-Constants

$$\begin{matrix} C_{11} & C_{12} & C_{13} & -C_{14} & 0 & 0 \\ C_{12} & C_{11} & C_{13} & C_{14} & 0 & 0 \\ C_{13} & C_{13} & C_{33} & 0 & 0 & 0 \\ -C_{14} & C_{14} & 0 & C_{44} & 0 & 0 \\ 0 & 0 & 0 & 0 & C_{44} & -C_{14} \\ 0 & 0 & 0 & 0 & -C_{14} & \frac{1}{2}(C_{11}-C_{12}) \end{matrix}$$

b)Piezoelectric Stress Constants

$$\begin{matrix} e_{11} & -e_{11} & 0 & -e_{14} & 0 & 0 \\ 0 & 0 & 0 & 0 & e_{14} & -e_{11} \\ 0 & 0 & 0 & 0 & 0 & 0 \end{matrix}$$

c)Dielectric Constants

$$\begin{matrix} \varepsilon_{11} & 0 & 0 \\ 0 & \varepsilon_{11} & 0 \\ 0 & 0 & \varepsilon_{33} \end{matrix}$$

TABLE 6

Constants of Tellurium at Room Temperature. Ref[43,44,70].

$\rho = 6210 \mathrm{Kg/m^3}$

$C_{11} = 0.326 \mathrm{x} 10^{11} \mathrm{Newtons/m^2}$

$C_{12} = 0.084 \mathrm{x} 10^{11} \mathrm{Newtons/m^2}$

$C_{13} = 0.261 \mathrm{x} 10^{11} \mathrm{Newtons/m^2}$

$C_{14} = 0.124 \mathrm{x} 10^{11} \mathrm{Newtons/m^2}$

$C_{33} = 0.722 \mathrm{x} 10^{11} \mathrm{Newtons/m^2}$

$C_{44} = 0.312 \mathrm{x} 10^{11} \mathrm{Newtons/m^2}$

$e_{11} = 0.42 \mathrm{Coulomb/m}$

$e_{14} = 0.17 \mathrm{Coulomb/m}$

$\varepsilon_{11} = 22.98 \mathrm{x} 10^{-11} \mathrm{Farad/m}$

$\varepsilon_{33} = 38.97 \mathrm{x} 10^{-11} \mathrm{Farad/m}$

APPENDIX C

Reprinted from **APPLIED OPTICS**, Vol. 19, page 186, January 15, 1980

Resolution criteria for acoustooptic deflectors

David G. Hawkins

Andersen Laboratories, Inc., 1280 Blue Hills Avenue, Bloomfield, Connecticut 06002.
Received 24 September 1979.
0003-6935/80/020186-02$00.50/0.

The classic resolution criterion, the Rayleigh criterion,[1] comes from astronomical spectroscopy. It says that for a long rectangular slit illuminated with uniform plane waves, two images are just resolved if the peak intensity of each falls on the first minimum of the other. The angular separation between the peaks in this case is λ/d, where d is the length of the aperture. When the two intensity patterns are summed, the pattern has a null between the two peaks that is down 19% relative to the peaks.

Most acoustooptic deflection cells, however, are usually illuminated with a truncated Gaussian beam instead of a uniform plane wave. Typically the truncation is done by the cell aperture at the $1/e^2$ intensity points. Randolph and Morrison[2] have calculated the resulting beam patterns and show that, for two adjacent deflected beams, if each peak is placed over the first minimum of the other, the peaks must be placed $1.22\lambda/d$ apart, and the resulting null depth is now 24% (relative to the peaks). Therefore, the number of Rayleigh resolved spots is not just $\tau\Delta f$, the time-bandwidth product, as would be the case with uniform plane waves but is

$$N = (\tau\Delta f)/\alpha, \qquad (1)$$

with $\alpha = 1.22$.

They also give curves showing the resulting null depths for this and other beam separations but expressed as a percent of the maximum plus the minimum of the summed pattern. It would seem to be more useful to express it relative to the maximum only, since one can then say that a particular resolution criterion requires the null to be so many percent down from the peak as is done in Ref. 1. This is summarized in Table I for several separations. Each separation listed can be thought of as a criterion of resolution, where the given α is used in Eq. (1) for the computation of the number of resolvable spots.

The choice of criterion depends on what null depth is needed for a particular application. The first criterion listed calls for a separation of $1.17\lambda/d$, which gives a null depth of 19%, just as the classic Rayleigh criterion did, hence its name, the Rayleigh equivalent resolution criterion.

A criterion using $\alpha = 1.34$ would give a null depth of 40%, about twice the Rayleigh equivalent depth, so we call it the double Rayleigh criterion.

It is interesting to note what happens to the width of a Gaussian beam as a result of the input and output aperturing at the deflector. Before deflection, the angular halfwidth of the beam measured from the center to the $1/e^2$ intensity point is $2\lambda/\pi d = 0.637\lambda/d$.[3] After deflection, Ref. 2 shows that the beam has broadened so that its new $1/e^2$ intensity point is $0.83\lambda/d$ from the center, and it has a first minimum of zero intensity at $\sim 1.2\lambda/d$ from the center. This broadening is of course fully taken into account in the construction of Table I. For example, for two adjacent output beams to just touch at their $1/e^2$ points, their centers must be separated (in angle) by $2 \times (0.83\lambda/d) = 1.66\lambda/d$ as is shown by the last entry in the table, i.e., not $2 \times (0.637\lambda/d) = 1.27\lambda/d$ as would be expected without broadening.

Table I. Resolution Criteria for Acoustooptic Cells

Criterion	Null depth (%)	α
Rayleigh equivalent	19	1.17
Rayleigh	24	1.22
Double Rayleigh	40	1.34
Touch at $1/e^2$ points	73	1.66

Aronson[4] briefly discusses resolution criteria in his review article on acoustooptic scanning. His second criterion is for uniform plane waves passing through a circular aperture (something rarely encountered in acoustooptics) and again placing the output peak of each over the first minimum of the other. It is an interesting coincidence that the α for this case, 1.22, is the same as in the case of Gaussian beams truncated at their $1/e^2$ points and placed peak-to-minimum. His third criterion incorrectly lists $\alpha = 1.34$ for the $1/e^2$ points just touching.

Table I criteria here are only for Gaussian beams truncated at their $1/e^2$ points. Criteria for other truncation points can be picked up from curves in Ref. 2.

References

1. M. Born and E. Wolf, *Principles of Optics* (Pergamon, New York, 1975), pp. 333–334.
2. J. Randolph and J. Morrison, Appl. Opt. **10**, 1453 (1971).
3. A. Yariv, *Introduction to Optical Electronics* (Holt, Rinehart & Winston, New York, 1971), p. 35.
4. H. Aronson, "Acousto-Optic Scanning," Laser Focus, 36, Dec. 1976.

APPENDIX D

CO_2 LASER DESIGN , GAIN, POWER, AND SPECTRAL CHARACTERISTICS.

Figure D-1 is a schematic diagram of the apparatus used to observe lasing at the 10.6μm 00°1 P(J) and R(J) lines of the CO_2 gas. A nominal gas mixture of 7% CO_2; 40% He; 48% N has been used to which 5% Xe has sometimes been added for enhanced power measurements. Our total flow rate was 170 ml/min, measured with Matheson rotameters. The laser discharge current was 8mA, and the total pressure was 7 Torr. The CO_2 discharge tube has an active length of 100cm and an i.d. of 1cm. The laser cavity consists of a diffraction grating reflector on one end with 75 lines/mm for accurate wavelength tuning and a concave 60% reflecting mirror at the other end mounted on a piezoelectric transducer for finer tuning. The active plasma effective diameter is of the order of 9mm. Power measurements were obtained with a properly calibrared optoacoustic detector containing 1-Torr CO_2 as the absorbing gas.

Figure D-2 shows the results of our power measurements which show an increase of the order of 100% at each of the entire set of emission lines for the P(J) and R(J) branches in the 10.6μm region when Xe is present in the mixture.

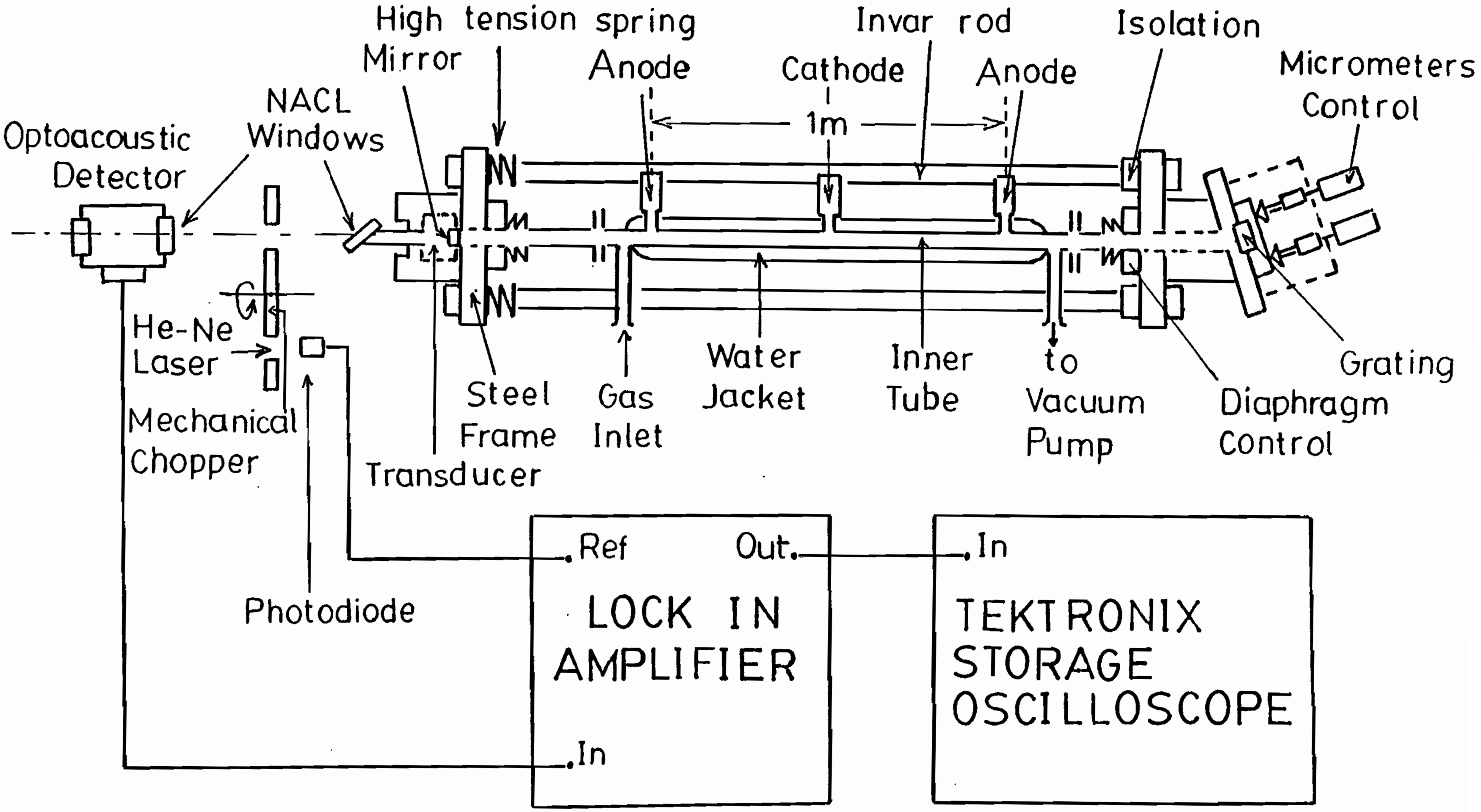

Figure D-1. CO_2 Laser Design.

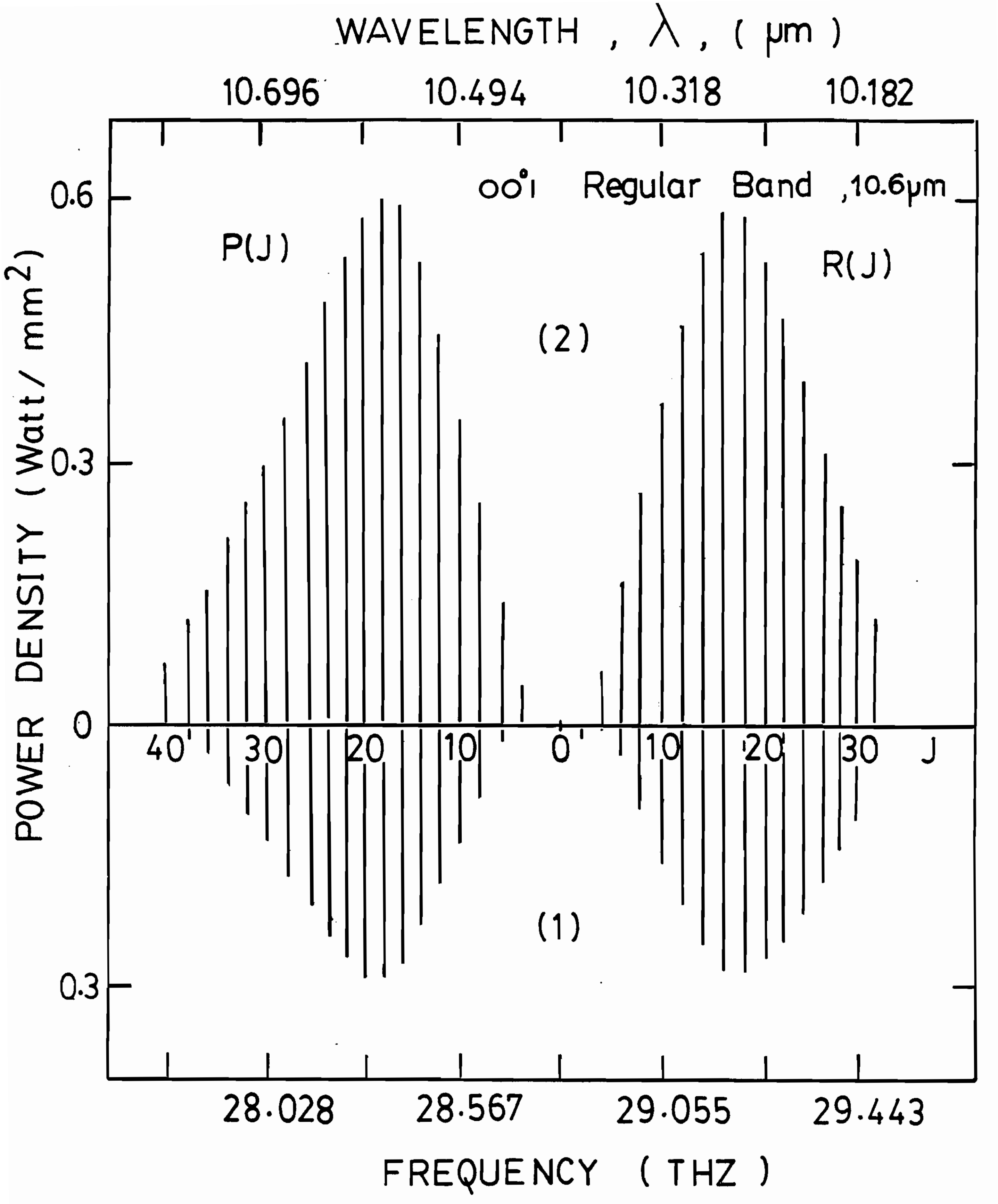

Figure D-2. Spectral Lines of the CO_2 Laser.

To estimate analytically the expected values of the laser output power levels it is necessary to obtain information on the single- pass gain for the given gas mixture.

Using the available general theoretical analysis and our evaluated increase cavity gain condition, we obtain analytically the expected output power levels for the given laser system and obtain excellent agreement with the measured results.

Figure D-2 shows the results of our power increase measurements which show an increase of the order of 100% at each of the entire set of emission lines for the P(J) and R(J) branches in the 10.6μm region, when Xe is present in the mixture.

By combining results from [59] [61] the estimated single-pass gain in the absence of the Xe gas can be evaluated; indeed, Fig 3 of Ref [61] gives the calculated relative gain coefficients vs frequency of the 10.6μm $00^0 1$ P(J),R(J) branches in CO_2 for a flowing gas mixture composition of 14% CO_2;20% N_2; 66% He at a total pressure of 5 Torr and discharge current of 16mA. From Ref [59] Figs 1 and 4, Ref [61] Fig 6, which allow the scaling of the previous results to different CO_2-gas concentrations and discharge current conditions, the estimated single-pass gain for our own experimental conditions is obtained and shown as plot (a) in Fig D-3,where an absolute gain of 0.70 at the P(18) $00^0 1$ transition is shown.Using then the results shown in Ref [59], Fig 3, the increment of the single-pass gain for 5% Xe addition is obtained to be 0.25 at the P(18) $00^0 1$ transition. Point M is thus obtained on plot (b) of Fig D-3 representing the absolute gain of the laser cavity at this transition frequency. Plot (b) which represents the Xe enhanced gain level at all P(J)

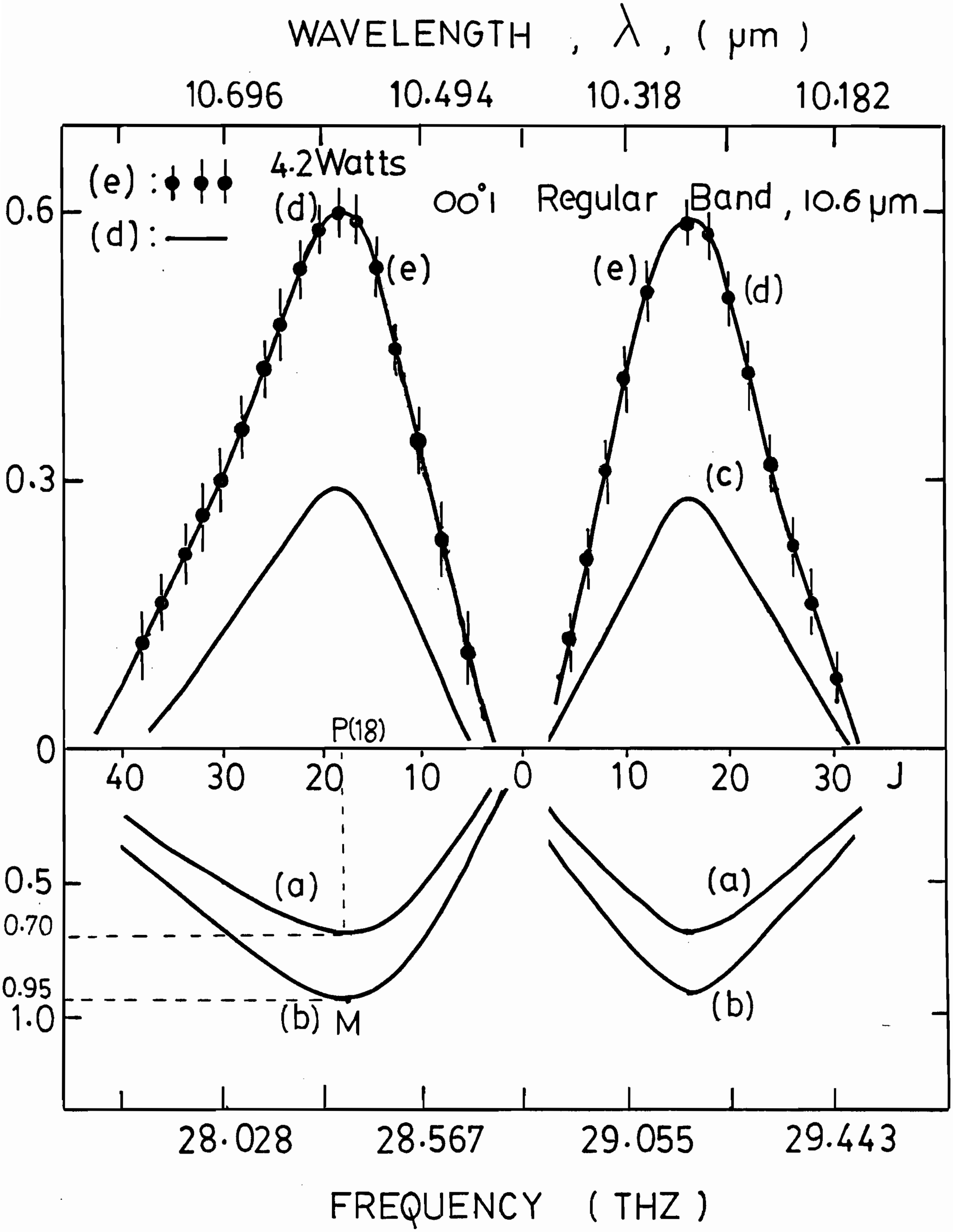

Figure D-3. Gain versus Power Curves of the CO_2 Laser.

and R(J) transition frequencies is then obtained by scaling the relative values of the gain of Ref [61],Fig 3, with the use of the calculated value at point M.

As the next step, to estimate the expected laser output power increase with Xe, the theoretical plot i_t of Ref [60] Fig 4 is used, since the latter corresponds to the same mixed Gaussian-Lorentzian broadened linewidth gain curve, subjected to longitudinal and transverse spatial hole burning which prevails in our experimental conditions; it should be observed that i_t displays relative power density calculations compared with our own data which is given in power units. However, since we have experimentally determined that the beam diameter did not increase by more than 10% for up to 100% power enhancement at all the P(J) or R(J) transitions investigated, we consider power density and total power relative variations to be equivalent. With the help of our plot (c) in Fig D-3 which shows our own measured Xe-free laser output power levels plot (d) is thus obtained predicting an estimated power increase of 100% at all transition frequencies. Finally, our experimental measurements shown as plot (2) in Fig D-2 are transcribed as plot (e) in Fig D-3 showing excellent agreement with the estimated values.

APPENDIX E

OPTOACOUSTIC DETECTION IN SF_6 GAS.

A. General Characteristics.

The first observations of Lamb dip optoacoustic spectroscopy have been reported for the CO_2 gas and for the I_2 vapor [64]. To the best of our knowledge the present is the first report of Lamb dip optoacoustic detection in SF_6. In Fig E-1, the chopped laser power absorbed in SF_6 results in axial heating inside the optoacoustic cell that results in a pressure wave train which is sensed by a miniature microphone. In Reference [73] a general analysis based on the thermodynamic solid-gas theory of Kerr and Atwood [65], Kamm [66] and more recently Wake and Amer [68], Kreuzer [72], shows that the lock-in amplifier output voltage at the fundamental chopping frequency which results from the pressure pulses is given by Eq(E_1).

$$V \simeq s(\omega)\frac{\gamma-1}{V}\,W\beta(P_o)\,L\,\frac{|\tau_R-\tau_L|}{(1+\omega^2\tau_R^2)^{1/2}(1+\omega^2\tau_L)^{1/2}} \qquad (E_1)$$

Where $\beta(P_o)$ is the gas absorption coefficient. cm^{-1}. (See section E).

$s(\omega)$ = rated sensitivity of the microphone. $mV/N/cm^2$.

W = laser power. (Watt).

V = volume of the gas cell. (cm^3).

$\omega = 2\pi f$, f=chopper frequency

$\gamma = C_P/C_V$. C_V and C_P are respectively the gas specific heat at constant volume and constant pressure Cal/g.Deg.K.

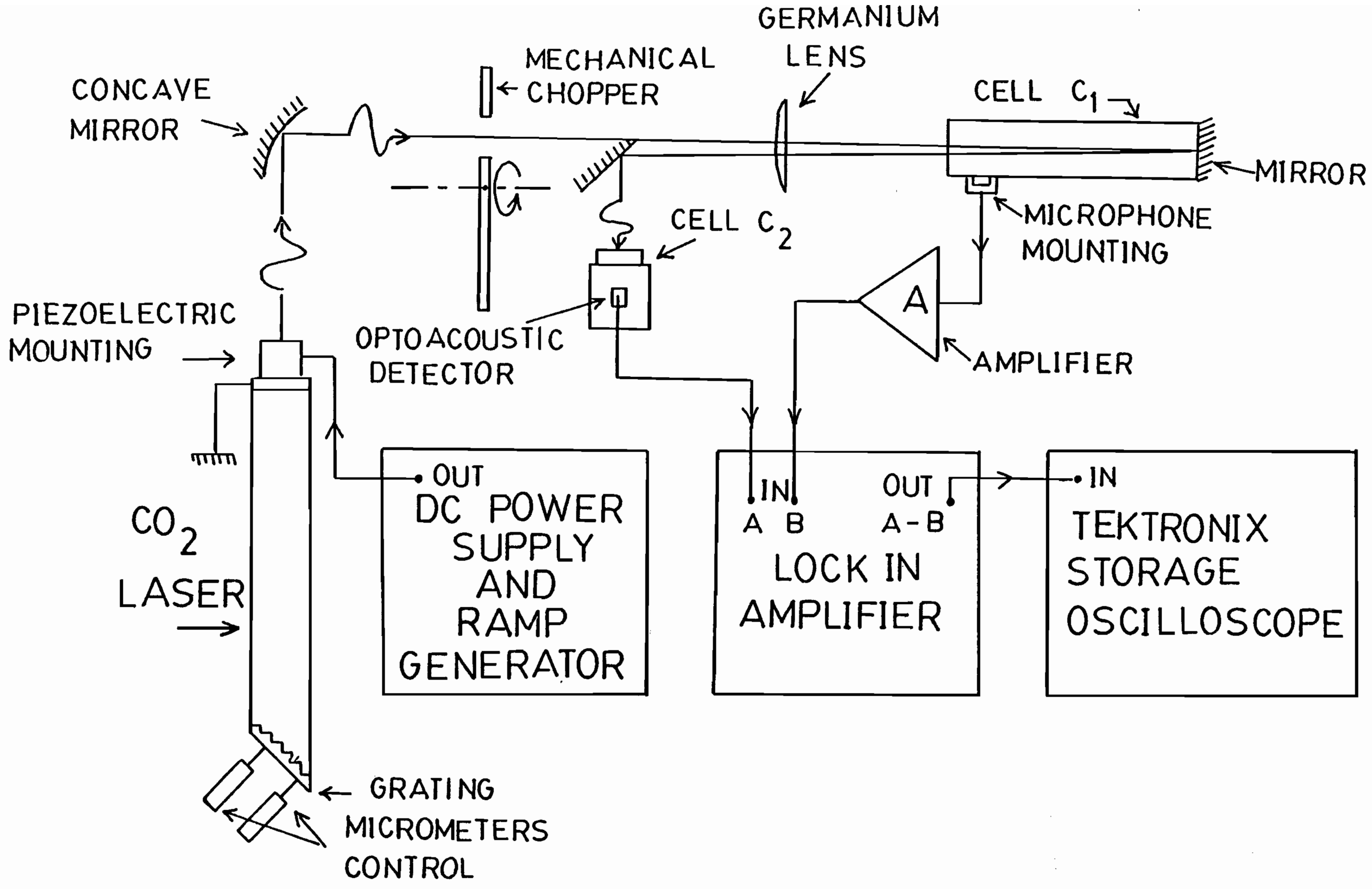

Figure E-1. Experimental Apparatus for Lamb Dip Optoacoustic Detection in SF_6 gas.

K = gas thermal conductivity Cal/Sec.Deg.K.cm. (See Eq(E_2)).

τ_R = molecular relaxation time

τ_L loss time constant which in most practical applications is of the order of the thermal time constant τ_T

L = length of optoacoustic cell

T = temperature.

According to Kerr and Atwood [65],

$$\tau_T = \frac{a^2}{(2.4)^2 \eta} \tag{E_2}$$

Where a = cell radius, and η = gas thermal diffusivity $= \frac{K}{\rho C_V}$

Fraim and Murphy [67] have shown that the dominant noise source in this scheme is the Johnson noise of the microphone field effect transistor (FET) preamplifier input resistor R_{in}, which exhibits a 1/f functional dependence at the output of the FET preamplifier in the low-frequency cutoff region between 10 and 100MHz, more specifically:

$$e(f) = G\left(\frac{4KT\Delta f}{R_{in}}\right)^{1/2} \frac{1}{2\pi f C_T} \tag{E_3}$$

Where e(f) = noise voltage in volts

G = gain of FET preamplifier

K = Boltzmann constant

T = temperature

R_{in} = input resistance of FET preamplifier

f = modulation frequency;

C_T= microphone plus FET preamplifier input capacitance

Δf = FET preamplifier bandwidth.

The measured noise voltage is $1\mu V/(Hz)^{1/2}$ at 50 Hz for a specified bandwidth of Δf = 10kHz.

B.Low-Pressure Cell Characteristics.

One low-pressure optoacoustic detector was specifically designed to allow the high-resolution observation of individual Lamb dips in SF_6. It consisted of a 45 cm long, 1.5-cm diam cylindrical glass cell (see Fig E-1). A Knowles Electronics miniature microphone was placed at the front, and a 99.8% reflecting mirror for the 10.6 μm radiation was placed at the rear. As the laser frequency is tuned within the mixed Gaussian-Lorentzian gain profile of the P(16) or P(18) CO_2 laser transition, and when the incident CO_2 laser beam coincides inside the cell with the reflected beam, strong standing-wave saturation resonances are detected in the SF_6 gas at the dip profile center of each adjacent Doppler widened absorption line; at low-pressure levels the dips are individually observable at the centers of the several overlapping absorption lines. The latter have widths of the order of 25MHz and magnitudes proportional to the term $\beta(P_o)$ in Eq(E_1) evaluated in the ν_3-band of SF_6. A pressure of 100mTorr was chosen for this cell so that the width of the strongest P(16) Lamb dip profile measured at maximun power level was 5MHz as shown in Fig E-2a.

The dominant broadening effect which is of the order of 4.6MHz at 100mTorr SF_6 gas pressure is due to elastic collisions; a secondary geometric broadening of the order 0.6MHz is added due to a maximun estimated crossing angle between the overlapping

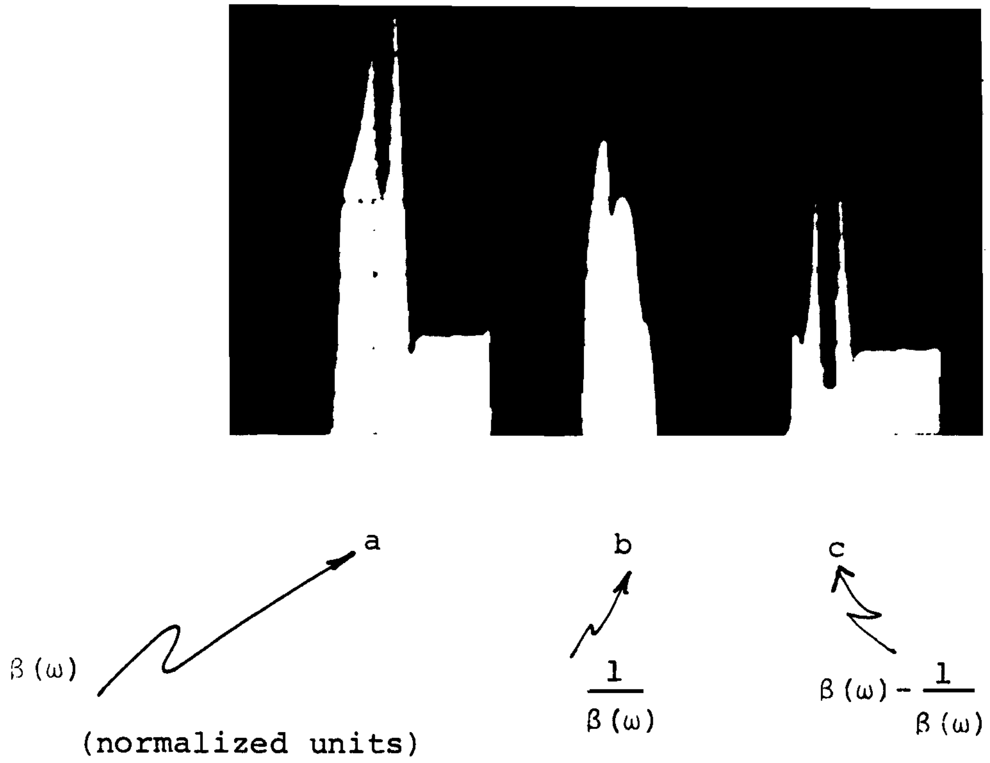

Figure E-2. Optoacoustic Lamb Dip Detection in SF_6 Gas.
a)Saturation Phenomenon ausing a "Dip" in the Absorption at $\omega = \omega_o$.This is a Plot of $\beta(\omega)$ Given by Equation (E_4).
b)Corresponding Inverted Lamb Dip. This is a plot of $1/\beta(\omega)$.
c)a-b resulting in 100% increase in the contrast of the Lamb Dip.

laser beams of 40mrd. The experimentally determined characteristics of our low-pressure optoacoustic detector are: $\tau_L \simeq \tau_T \simeq$ 1msec and $\tau_R \simeq$10msec at 100mTorr. This value of τ_T is consistent with the analytically expected figure of Eq(E_2), whereas the molecular relaxation time constant τ_R is generally a parameter that is determined experimentally. For 1-W incident power the SNR was of the order of 10 at 50Hz measured at the output of the FET preamplifier. Finally, allowing time intervals equal to $3\tau_L$ to reach the steady temperature distribution, the required chopping frequency is found to be < 1/6msec $\simeq$166Hz.

C.High-Pressure Optoacoustic Detector.

The optoacoustic detector consisted of a 10-cm long 1-cm diam cylindrical aluminium cell filled with 20 Torr SF_6 gas (see Fig E-1). The fundamental frequency lock-in amplifier output is again given by Eq(E_1) with the following measured characteristics: $\tau_R \simeq$ 5msec, $\tau_R < \tau_L$. $\tau_L \simeq \tau_T$ is calculated from Eq(E_2) and is equal to 22msec at 20Torr.

For 1-W incident power of the CO_2 laser,the SNR is now 500. Indeed according to Wake and Amer [68], for best performance of this optoacoustic detector a low chopper frequency is required, and the optimun pressure of SF_6 gas must be of the order of a few tens of Torr.

Experimentally, to satisfy the requirements of both high and low - pressure optoacoustic cells and for best noise rejection at the lock-in amplifier output, a chopping frequency of 28 Hz was chosen.

The purpose of this detector is to monitor the variations of the CO_2 laser beam intensity returning after interaction with the SF_6 gas inside the low-pressure optoacoustic cell. The term $\beta(P_o)$ in Eq(E_1) now defines an absorption line of SF_6 which has a non-Doppler homogeneously broadened linewidth of the order of 71MHz at 20Torr calculated from the known value of the cross section of the SF_6 molecules.

Thus, due to the very close frequency spacing of the individual SF_6 absorption lines, $\beta(P_o)$ exhibits a practically flat frequency response within the ν_3 band of SF_6 and therefore becomes a convenient wideband, but slow, room temperature detector for the 10.6μm radiation.

D.Lamb Dip Optoacoustic Detection in SF_6.

The CO_2 laser design and its operating characteristics are described completely in Ref [34].Figure E-1 is a schematic diagram of the apparatus used to observe the Lamb dips in the SF_6 gas at the P(16) and P(18) $00^0 1 \rightarrow 10^0 0$ laser transition line. The output of the laser enters first the double-pass low-pressure SF_6 absorption cell designated as C_1 in Fig E-1.To make Lamb dip observations practical the beam is expanded in diameter to 1.5 cm and then collimated by a germanium lens before entering the cell C_1. The returning laser beam is then passed through the high-pressure cell C_2 which has an output proportional to the laser gain profile modulated by the inverse of the Lamb dip absorption line shape. When the output from the low-pressure cell C_1 shown in Fig E-2a is substracted from the output of the high-pressure cell C_2 shown in Fig E-2b the resultant signal is completly independent of the CO_2 laser power curve profile, and furthermore a 100% increase in the contrast of the Lamb dip is obtained as shown in Fig E-2c .

E. Gas Absorption Coefficient.

a) Low pressure case. (See section B). Inhomogeneous broadening.

Lamb [74] has derived the following equation for $\beta(P_o) = \beta(\omega)$,

$$\beta(\omega)=\frac{\alpha_o e^{-\left(\frac{\omega-\omega_o}{\Delta\omega_D}\right)^2}}{\left[1+\frac{I}{4I_s}\left(1+\frac{\Gamma^2}{(\omega-\omega_o)^2+\Gamma^2}\right)\right]^{1/2}} \qquad (E_4)$$

where $\Delta\omega_D = \left(\frac{2kT\omega_o^2}{Mc^2}\right)^{1/2}$ is the half-width of the line at 1/e intensity , related to the Doppler width at 1/2 by, $\Delta\omega_D = \text{Doppler}/4\pi(\text{Log}2)^{1/2}$.

$\alpha_o = \frac{(\pi)^{1/2}}{c\varepsilon_o\hbar\Delta\omega_D}\mu^2\omega N$ and $I_s = \frac{c\varepsilon_o\hbar^2\gamma^2}{2\mu^2}$ is a saturation parameter.

ω_o is the center frequency of the absorption line.

M is the mass of the atom.

T is the temperature.

c is the speed of light.

μ is the dipole moment of the atom.

N is the number of atoms/m^3. ($P_o = NkT$).

$\Gamma=2\gamma$. γ is a decay rate which includes the effect of collisions.

$\hbar = h/2\pi$. h is the Planck'constant.

$I = \frac{c\varepsilon_o E_o^2}{2}$ is the intensity of the incident laser beam.

E_o is the incident optic electric field.

b) High pressure case. (See section C). Homogeneous broadening.

In this case, the absorption coefficient becomes equal to [74],

$$\beta(\omega) = \frac{\Delta\omega_D \alpha_o}{\pi^{1/2}} \frac{\gamma}{(\omega-\omega_o)^2+\gamma_s^2} \qquad (E_5)$$

where $\gamma_s = \gamma(1+\frac{I}{I_s})^{1/2}$

$2\gamma_s$ represents the full width at 1/2 intensity of $\beta(P_o)$.

For CO_2 gas, $2\gamma_s$= 5MHz/Torr [75].

APPENDIX F

STABILIZATION OF THE CO_2 LASER

A. Experimental Procedure

The CO_2 laser in conjunction with its pair of high and low-pressure optoacoustic SF_6 gas cells is used to localize a Lamb dip frequency within the SF_6 gas absorption spectrum [62] [63]. A standard electronic negative feedback loop is then implemented where the CO_2 laser frequency is compared with the given Lamb dip so that a relative shift provides an error signal which in turn produces a laser mirror translation tending to minimize the shift and eventually lock the two frequencies. The experimental apparatus is shown in Fig F-1. Specifically, the laser frequency was tuned on the P(16) $00^01 \rightarrow 10^00$ line of the CO_2 gas; it was then driven to scan slowly across one of the strong SF_6 Lamb dips such as the Lamb dip center shown in Fig E-2a , that is known to be located at 8.81MHz from the peak of the P(16) line.

A small modulation signal is applied to the piezoelectric crystal to which the laser output mirror is attached; this results in a corresponding modulation of the laser power output which is detected and demodulated by the lock-in amplifier. The output of the latter is a dc feedback correction voltage which is returned to the piezoelectric crystal with the proper sign so as to complete a stable negative feedback loop that maintains the

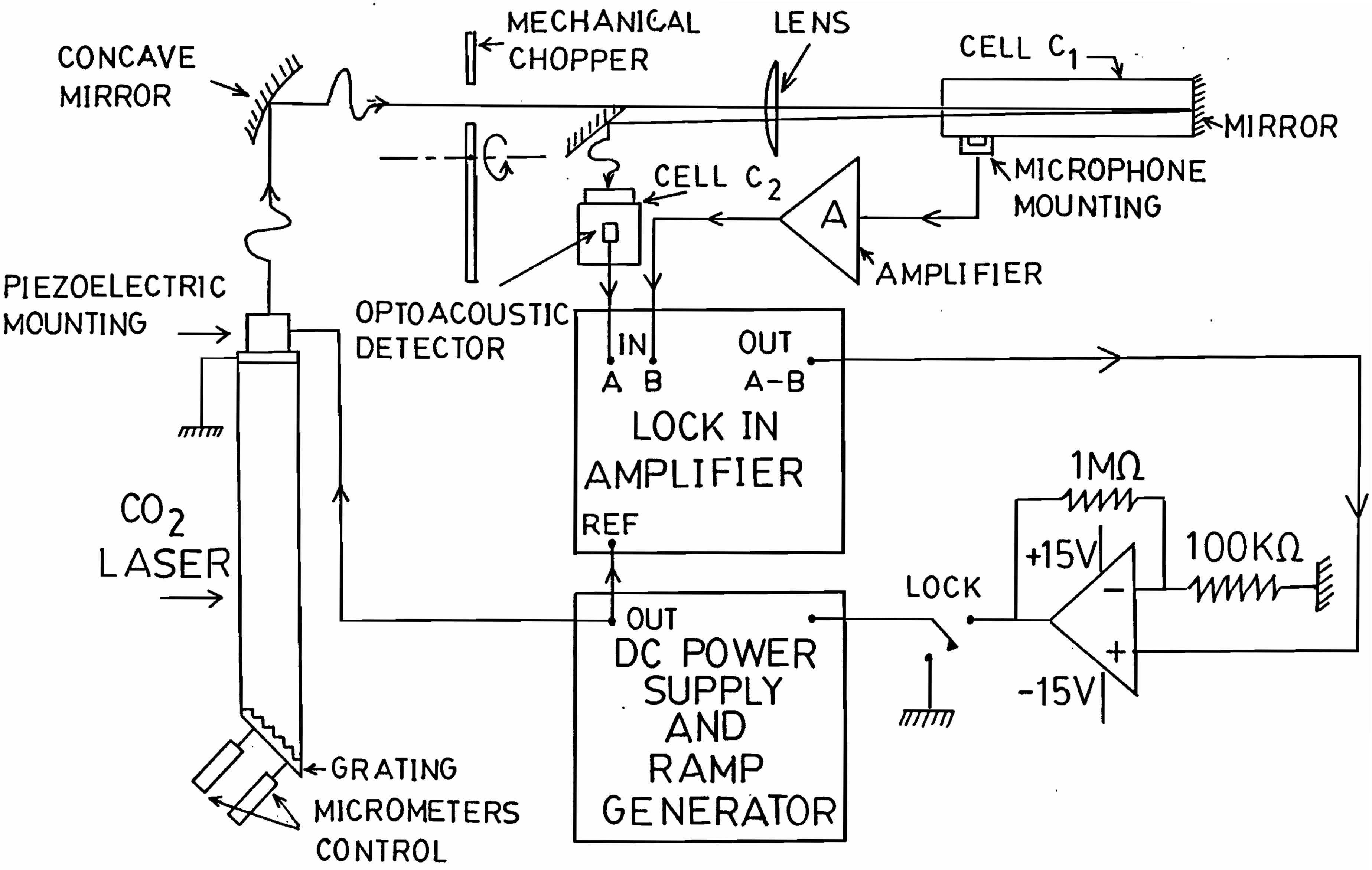

Figure F-1. Experimental Apparatus for the Stabilization of the CO_2 Laser.

laser cavity length to the tracked Lamb dip profile center.

The stabilization results obtained with our CO_2 laser design, are described in Chapter 6.

Note that during the optoacoustic experiments, the stabilization system was removed, since the drift of laser power per 10 minutes time interval was less than 0.2 Watts. (See Fig 6.2).

B.Theoretical Model

The phase lock loop system is shown in Fig F-1. It consists of a phase detector which is modelled by a multiplier and a low pass filter. In order to illustrate the operation, consider the two inputs to the multiplier as:

i) $A\sin(\omega_o t)$

ii) $B(\omega)\sin(\omega_o t+\Theta)$ (F_1)

The multiplication results in the following expression:

$$\frac{AB(\omega)}{2}\left[\cos(2\omega_o t+\Theta)+\cos\Theta\right] \qquad (F_2)$$

This consists of the sum and difference of the frequencies of the two inputs. This signal is then passed through a low-pass filter with a cut-off frequency set to well below the sum of the two input frequencies. The result is:

$$AB(\omega)\cos\Theta$$

This expression is proportional to the two input signal amplitudes and the difference in phase between the two signals. This signal is amplified by a constant gain according to the feedback gain required. The error signal then regulates a voltage controlled laser oscillator, (VCO). A decrease of the laser frequency corresponds to an increase of the error signal $B(\omega)\cos(\Theta)$.

C.Sources of Instability

The major sources of instability in frequency or power are due to changes in the optical length between the mirrors. In fact, it can be shown that:

$$\frac{\Delta f}{f} \simeq -\frac{\Delta L}{L} = \alpha \Delta T \qquad (F_3)$$

The two causes of change of length are:

i)Temperature change ii)External acoustic noise.

To reduce the thermal expansion of the laser cavity invar rods were used. The coefficient of thermal expansion for invar is $\alpha \simeq 1x10^{-6}/^{0}K$.

To reduce the effect of external acoustic noise on the cavity, it is desirable to set the lowest order longitudinal acoustic resonance above a few kilohertz since most of the acoustic noise occurs in the low frequency range.

The fundamental frequency for such structural oscillations is given by $f = \frac{V_s}{2L}$, where V_s is the speed of sound in the material L is the length of the cavity. For invar, V_s= 5000m/s,L=1.5m, thus f = 1.6KHz. Therefore, for any frequencies above this fundamental frequency, the end mirrors will oscillate out of phase and a jitter noise is observed.

APPENDIX G

MEASUREMENT AND CONFIRMATION OF THE GIANT M FIGURES FOR EXTRAORDINARY POLARIZED OPTIC BEAMS.

A.Selection of the Giant M Figures for Experimental Confirmation.

For experimental confirmation of the calculated giant M figures, we choose two AO configurations with extraordinary polarized incident and diffracted optic beams, for which many very high values of M have been found. (See Appendix A).

For small Bragg angles Θ_B^* near the Z* axis, in the X*Z* rotated interaction plane of Fig 3-3a the AO wavector triangle is isoceles. Thus, the center acoustic frequency can be tuned in the low frequency range between 20MHz and 100MHz making practical verification possible.

The values of M which have been chosen for experimental verification, are localized by the following Euler angles: $\phi = 0^0$, $\Theta = 130^0$, $\psi = 45^0, -45^0$ .The corresponding value of M is equal to: $M=285000\times10^{-15} sec^3/Kg$ associated with a pure slow shear acoustic velocity of 1027m/s which propagates along the X* axis.

These configurations are suitable for the design of a highly efficient two-dimensional (2D-AO) deflector.(See section C).

B.Experimental Procedure.

1)Crystal Cut:

First, we localize the crystalline axes of a Czochralski grown ingot of tellurium, by looking at the etch pits orientation produced on one of the crystal planes of the crystal by a solution of H_3SO_4 at 100° during 5mn [55]. Then, using a soft chemical sawing technique which avoids dislocations at the surface of the crystal, we obtain a cube from the ingot.

2)Measurement of the Giant M figures:

Let us verify the value of $M=2850000\text{x}10^{-15}\text{sec}^3/\text{Kg}$ calculated at $\phi = 0^0$, $\Theta = 130^0$, $\psi=45^0$. Using the pure shear wave which propagates along the X* axis at V_P=1027m/s, and an incident beam extraordinary polarized in the $(\vec{K}_I,\vec{Z}^*)$ plane, with $\vec{K}_I$, making an angle of $\Theta_B^* = \lambda f/2n_I V_P \simeq 2^0$ at f_o =39MHz from the Z* axis in the X*Z* plane. 0.20 watt of acoustic power was coupled into the slow shear wave. The latter has a polarization angle of 45° in the X*Z* quadrant, and was launched by a 41° X-cut $LiNbO_3$ transducer.

We have measured a diffraction efficiency of 85%.

Hence,from Equations (3-18) and (3-21), we obtain:

$$M = \frac{2\lambda_o^2}{\pi^2}\frac{1}{P_A}\frac{H}{L}(1.4) \simeq 280000\text{x}10^{-15}\text{sec}^3/\text{Kg} \quad (H/L\simeq 2).$$

The other giant M value localized at $\phi = 0^0$, $\Theta = 130^0$, $\psi=-45^0$has been verified in a similar way as follows:

Measuring a diffraction efficiency of 100% and 1 watt of acoustic power coupled into the pure slow shear wave,(V_P=1027m/s, polarization angle,45° in theX*Z* quadrant),we obtain:

$$M = \frac{2\lambda_o^2}{\pi^2}\frac{1}{P_A}\frac{H}{L}(2.5) \simeq 250000\text{x}10^{-15}\text{sec}^3/\text{Kg} \quad (H/L\simeq 4)$$

The other 4 lower values of M localized at $\phi=0^0$, $\Theta=130^0$, $\psi=\pm 45^0$ have also been verified succesfully experimentally with a discrepancy estimated at 20% from the following calculated values (sec^3/Kg):

$\phi=120^0, \Theta=130^0, \psi= 45^0, V_p=1181m/s$, Slow Quasi shear ,$M=15500x10^{-15}$.

$\phi=120^0, \Theta=130^0, \psi= 45^0$, $V_p=3536m/s$, Pure longitudinal ,$M=880x10^{-15}$.

Finally, by rotating the optic polarization by 90^0, the optic beams become isotropically polarized. We have verified experimentally the value of M which is associated with the pure longitudinal acoustic mode. The latter could be launched easily with a 36^0 Y-cut $LiNbO_3$ transducer, making experimental verification ideal. A discrepancy of 20% between the measured and the calculated value has been obtained.

The calculated value is:

$\phi=0^0$, $\Theta=130^0$, $\psi= 45^0$, Pure Longitudinal Acoustic Wave.$V_p=3536m/s$, $M=640x10^{-15} sec^3/Kg$.

Note that in the isotropic case, the calculations require only the knowledge of the photoelastic coefficients previously found by Fukuda, whereas in the extraordinary case the complete photoelastic tensor must be known.

The other values of M corresponding to $\psi=-45^0$ are identical and are not considered here.

C.Conclusion.

This crystal configuration is suitable for the analysis of a 2D-AO very efficient CO_2 laser-radar-deflector which is under study at the present time at McGill University.This 2D-AO deflector will also find important applications in the field of Optical Computing and CO_2 Laser Communications. More specifically, the tellurium crystal is capable of modulating the laser beam in amplitude, frequency and in pulse code modulation .In the multifrequency phase modulation mode (FM modulation), the high power CO_2 laser modulated by the tellurium 2D-AO deflector can carry theoretically an unlimited number of TV communication channels with the highest efficiency and the highest gain in the recieving antennas at 10.6µm.[75,77,78,79,80,81,82].